



Title	Modeling and Analysis of Geo-disaster Problems Using the SPH Method
Author(s)	Ibrahim, Ahmed Mohamed Abdelrazek
Citation	北海道大学 博士 工学 甲第 1202号
Issue Date	2015/09/25
DOI	10.14943/doctoral/12022
Doc URL	http://hdl.handle.net/2115/62857
Type	theses [doctoral]
File Information	Ahmed Mohamed Abdelrazek Ibrahim.pdf



[Instructions for use](#)

Modeling and Analysis of Geo-disaster Problems using the SPH Method

By

Ahmed Mohamed Abdelrazek Ibrahim

A thesis submitted in partial fulfillment of the requirements for the degree of Doctor
of Philosophy in Engineering

Examination Committee:

Prof. Yasuyuki Shimizu
Prof. Norihiro Izumi
Assoc. Prof. Ichiro Kimura
Assoc. Prof. Tomohito Yamada

Doctor's thesis

Hydraulics Research Laboratory

Division of Field Engineering for Environment

Graduate School of Engineering, Hokkaido University

September, 2015

ACKNOWLEDGEMENTS

First, I wish to express my deep, sincere thanks to my advisor, Associate Professor Dr. Ichiro Kimura for his guidance, supervisions, instructions, valuable advices and suggestions, and necessary assistances throughout the last three-year study period at the Laboratory of Hydraulic Research, Hokkaido University. From the bottom of my heart, I also wish to express my gratitude to my supervisor, Professor Dr. Yasuyuki Shimizu for his accepting me as his student, his guidance, valuable suggestions, and his creation of good condition and opportunities for me during my last study period.

I am thankful to my laboratory colleagues for their assistances through the last three years.

In order to have today achievements, I would like to express my deep gratitude to the Japanese Government for their support of financial assistance as the scholarship during my study period in Japan.

On this occasion, I wish to express my greatest gratitude to my lovely wife, Mona Ali Mustafa and my daughter, Hamsa Ahmed for their care, encouragement, and moral support throughout the time I have lived and learned in Sapporo.

Finally, I would like to give this achievement, Doctor Degree, to my family, including my parent, my brothers, and my sister.

ABSTRACT

Geologic disaster is one of several types of adverse geologic conditions capable of causing damage or loss of property and life. It includes earthquakes, landslides, debris flow, soil liquefaction, rock falls, avalanches, tsunamis, and flooding. These disasters may be induced by natural factors and human activities, and can cause damage to infrastructures, property and loss of human life. Every year, millions of people all over the world experience the effects of geologic disasters. Hence, it is in a major importance to establish effective prediction methods for such events appear to be helpful. This study treats the destruction of recent geo-disasters in the world and basic characteristics of large deformation in these disasters. Based on a review of studies on large deformation simulation and its current limitations, a novel mesh-free particle method called Smoothed Particle Hydrodynamics is introduced, and its advantages and disadvantages are detailed. The basic concept of the SPH method and its innovation are also summarized here.

Our main target is to develop 2D (two-dimensional) and 3D (three-dimensional) models on the basis of the Smoothed Particle Hydrodynamics (SPH) method to simulate various phenomena in the science of computational fluid dynamic. The SPH method is a mesh-free Lagrangian method. It does not require Eulerian grids and deals with a number of particles in a Lagrangian framework.

We developed a Two-dimensional SPH model to simulate free surface flow problems, and we used it to simulate three benchmark tests, (Dam breaking, collapse of a water column with a rigid obstacle, and dam break on a wet bed). The simulation results were compared with experimental data and the solutions of Moving Particles Semi-implicate method. The comparison shows a good agreement and states that our SPH model could capture the water free surface shape precisely, (Abdelrazek et al., 2014, J.S.C.E Ser. B1, Vol.70 No. (4), pp. I_67-I_72). The model is then extended to be Three- dimensional and used to solve the same benchmark tests. We get more realistic and good results in terms of particles spreading and the shape of free surface.

A novel non-Newtonian three-dimensional SPH model was developed to simulate real snow avalanches mechanisms. The snow was considered as a Bingham fluid and the snow viscosity was calculated based on the Bingham constitutive model, on the basis of Coulomb's failure criterion. An equivalent Newtonian viscosity is calculated to express the Bingham viscosity into Navier-Stokes equations. Model validation was performed by simulating the movement of an unsteady mudflow released from a reservoir of a finite size onto a steep channel (Komatina & Jovanovic 1997, Journal of hydraulic research). The results show a good agreement between our models and the experimental results, indicating that this numerical method can be used for practical simulation of non- Newtonian fluid. A small scale snow avalanche experiment with different types of obstacles was simulated using the present refined SPH model. Numerical results showed that, in the most cases, good agreements were found by the means of leading-edge position and the travel length, (Abdelrazek et al., 2014, River Flow 2014& J.S.C.E, Ser. A2, Vol. 70, No.2, pp.I_681-I_690).

The elastic-perfectly plastic model has been implemented in the SPH to develop three-dimensional SPH model to simulate the gravity granular flow past different types of obstacles. The model was validated by the experiment on the collapse of 3D axisymmetric column of sand. A good agreement was observed between the numerical and experimental observations. Granular flows past different types of obstacle, (A group of stake rows with different spacing, circular cylinders, forward-facing and rearward-facing pyramids (tetrahedral) wedge) have been numerically simulated using the SPH model. The computational results were compared with the experimental data, and two numerical methods to check the capabilities of the proposed model. The numerical results in the first case in

terms of the final granular deposition shapes, spreading of the particles and the position of the leading edge is found to be in good agreements with the experimental results. Although the efficiency factor from the experimental results in all cases is slightly greater than the calculated from the SPH results, the error is less than 5 %. Simulations of granular free-surface flows around a circular cylinder, and tetrahedral obstacle show that the present SPH model can capture and describe the formation of the bow shock, normal shock, and oblique shock around the obstacle. It also succeeded in describing the protected area as observed in the experiments, the hydraulic avalanche model solution, and the Savage and Hutter theory solution. This study suggests that the proposed refined SPH could be a powerful tool for solving problems with granular materials subjected to large deformation, and could be used to design real avalanche defenses (Abdelrazek et al., 2015, J.S.C.E Ser. B1, Vol.71, No.4, pp. I_199-I_204 & Abdelrazek et al., 2015, Journal of Glaciology, submitted).

An application of the smoothed particle hydrodynamics (SPH) to simulation of soil–water interaction is presented in order to simulate the soil scour and erosion behind the seawall had occurred during the overflow (return flow). In this calculation, water is modeled as a viscous fluid with weak compressibility and soil is modeled as an elastic–perfectly plastic material. The Mohr–Coulomb failure criterion is applied to describe the stress states of soil in the plastic flow regime. The interaction between soil and water was done by adding the seepage force and pore water pressure terms to the momentum equation. The Louvain erosional dam breaks experiment which induces a surge leading to erosions of the soil, (Fraccarollo and Chapart, 2002), was used to validate our model. The results were compared with experimental data and showed a good agreement between the simulation and experimental results. Finally, the model applied to simulate the return flow scouring experiment done by Yamamoto (2011). It was confirmed that the SPH method can express soil erosion and scouring. However, its analysis result is good from a qualitative perspective, but not so good from quantitative one.

Table of Contents

ACKNOWLEDGEMENTS.....	iii
ABSTRACT.....	iv
Table of Contents.....	vi
LIST OF TABLES.....	x
LIST OF FIGURES.....	xi
Chapter 1.....	1
Introduction.....	1
1.1. BACKGROUND AND MOTIVATION.....	1
1.2. THE ROLE OF NUMERICAL SIMULATION.....	1
1.2.1. Solution steps of general Numerical Simulations.....	2
1.3. GRID-BASED SOLVERS OF NAVIER-STOKES EQUATION.....	2
1.3.1. Lagrangian Grid-based solver.....	2
1.3.2. Eulerian Grid-based solver.....	3
1.3.3. Combined Lagrangian and Eulerian Grids.....	4
1.4. MESH-FREE BASED SOLVERS OF NAVIER-STOKES EQUATION.....	4
1.4.1. Particle methods, the Lagrangian gridless solvers.....	5
1.4.2. Eulerian gridless solvers.....	6
1.5. STRUCTURE OF THE THESIS.....	6
Chapter 2.....	8
SPH Concept and Formulation.....	8
2.1 BASIC CONCEPT OF SPH.....	8
2.2 SPH APPROXIMATION.....	9
2.2.1 Kernel Approximation.....	10
2.2.2 Particle Approximation.....	11
2.3 NUMERICAL ASPECTS OF THE SPH MODEL.....	12
2.3.1 Initial Settings.....	12
2.3.2 Neighboring Particle Searching Algorithm (linked- list).....	12
2.3.3 Kernel Function.....	13
2.3.4 Boundary Treatment.....	14
2.3.5 Integration Schemes.....	15
2.3.6 Outputs of Calculation.....	16

2.4	SUMMARY	16
Chapter 3		17
Two-dimensional and Three-dimensional Numerical Simulations of Free Surface Flow Problems Using SPH.....		17
3.1	INTRODUCTION	17
3.2	GOVERNING EQUATIONS	17
3.3	DISCRETIZATION OF GOVERNING EQUATIONS	18
3.4	NUMERICAL RESULTS	19
3.4.1	Dam breaking	20
3.4.2	Collapse of water column with a rigid obstacle.	20
3.4.3	Dam breaks on a wet bed	21
3.4.3.1	Results and analysis	21
3.5	COMPARISON BETWEEN SPH AND MPS METHODS FOR NUMERICAL SIMULATIONS OF FREE SURFACE FLOW PROBLEMS	26
3.5.1	MPS model for water	26
3.5.2	Boundary conditions	27
3.5.3	Difference in calculation	27
3.5.4	Results and analysis	28
3.5.4.1	Effect of the initial particles spacing.....	30
3.5.4.2	Computational efficiency	31
3.6	SUMMARY	32
Chapter 4.....		33
Numerical simulation of snow avalanche as a Bingham Fluid Flow using non-Newtonian 3D-SPH model		33
4.1.	INTRODUCTION	33
4.2.	GOVERNING EQUATIONS.....	33
4.3.	SPH FORMULATION	35
4.4.	TEST CASE.....	36
4.5.	SNOW AVALANCHES MODEL TEST	38
4.5.1.	Model description	38
4.5.2.	Numerical simulations.....	40
4.5.3.	Results and analysis.....	40
4.6.	SUMMARY	45
Chapter 5.....		46

Simulation of three-dimensional rapid free-surface granular flow past different types of obstructions using the SPH method	46
5.1. INTRODUCTION	46
5.2. GOVERNING EQUATIONS	47
5.3. CONSTITUTIVE EQUATIONS FOR SOIL	48
5.4. DISCRETIZATION OF GOVERNING EQUATIONS	49
5.5. TEST CASE.....	49
5.6. RESULTS AND DISCUSSIONS	52
5.6.1. Gravity granular flows past a group of stake rows.....	52
5.6.1.1. Model description	52
5.6.1.2. Numerical simulations	54
5.6.1.3. Results and analysis	54
5.6.2. Granular free-surface flow around a circular cylinder	56
5.6.2.1. Model description	56
5.6.2.2. Numerical simulations	57
5.6.2.3. Results and analysis	58
5.6.3. Gravity granular flows past tetrahedral wedge	60
5.6.3.1. The model description	60
5.6.3.2. Numerical simulations	61
5.6.3.3. Results and analysis	61
5.6.4. Numerical Investigation of the Propagation of Shock Waves and Dead Zones in Rapid Flows of Granular Materials.....	63
5.6.4.1. The model description	63
5.6.4.2. Numerical simulations	64
5.6.4.3. Results and analysis	64
5.7. SUMMARY	67
Chapter 6.....	69
SPH modeling of Fluid–Soil interactions (Scouring behind Seawall).....	69
6.1. INTRODUCTION	69
6.2. SPH MODEL FOR WATER	69
6.3. SPH MODEL FOR SOIL	71
6.4. SOIL–WATER INTERACTION MODELING	72
6.5. LOUVAIN EROSIONAL DAM BREAK (TEST CASE)	74
6.6. RESULTS AND DISCUSSIONS	76

6.6.1. Scour prediction in front of seawall caused by the return flow	76
6.6.1.1. Model description	76
6.6.1.2. Numerical simulations	76
6.6.1.3. Results and analysis	77
6.7. SUMMARY	77
Chapter 7	79
Conclusions and future work	79
7.1. CONCLUSIONS	79
7.2. FUTURE WORK	80
APPENDIX A- PUBLICATION LISTS	81
REFERENCES	83

LIST OF TABLES

Table 3.1 Differences in the used methods	27
Table 3.2 First and last CPU time step (sec.) – case 2	31
Table 3.3 Total time elapsed (hr.)	32
Table 4.1 The mud-flow properties.....	36
Table 4.2 Snow parameters used in the numerical simulation.....	40
Table 4.3 SPH computed water leading edge, compared with experimental data and MPS results.....	44
Table 4.4 Total time elapsed (hr.)	45
Table 5.1 Efficiency factor for the different cases	56
Table 5.2 Soil parameters.....	57
Table 5.3 Semolina parameters	61
Table 5.4 Materials parameters	64

LIST OF FIGURES

Fig.1. 1 Lagrangian mesh/cells/grids for a shaped charge detonation simulation.....	3
Fig.1. 2 Eulerian mesh/cells/grids for a shaped charge detonation simulation.	4
Fig 2.1 SPH concept figure (The influence domain is circular with a radius of kh , and the cubic spline kernel and its first derivative).	9
Fig 2. 2 Set of neighboring particles in 2D. The possible neighbors of a fluid particle are in the adjacent cells, but this only interacts with particles marked by black dots.	13
Fig 2.3 Arrangement of boundary particles	14
Fig 3.1 Schematic sketch of the experimental setup.....	20
Fig 3.2 Initial geometry, location of the rigid obstacle, and location of point (A).....	20
Fig 3.3 Experimental setup of the dam breaks on a wet bed, and the location of point (B).....	21
Fig 3.4 Comparison between experimental images and SPH simulation showing the position of the free surface at $t=0.2s$, $t=0.4s$, $t=0.6s$ and $t=0.8s$. (Dam break).....	22
Fig 3.5 Comparison between experimental images and SPH simulation showing the position of the free surface at $t=0.1s$, $t=0.2s$, $t=0.3s$, $t=0.5s$, and $t=1.0s$	23
Fig 3.6 Snapshot of water particles at $t = 0.281$ Sec, numerical results (SPH) compared with experiment.....	24
Fig 3.7 Snapshot of water particles at $t = 0.561$ sec, numerical results (SPH) compared with experimente.....	25
Fig 3.8 Snapshots of water particles together with the pressure field at (A) $t= 0.2$ sec, (B) $t= 0.3$ sec, numerical results (SPH &MPS) compared with experimental – case1	28
Fig 3.9 Snapshots of water particles together with the velocity field at (A) $t = 0.281$ and (B) $t = 0.561$ sec, numerical results (SPH &MPS) compared with experimental – case2.....	29
Fig.3.10 Temporal variations of pressure at particles (A) and (B)	29
Fig 3.11 Particles positions and free surface shape using various initial particle spacing at $t=0.3$ sec (case1).	30
Fig 3.12 Particles positions and free surface shape using various initial particle spacing at $t = 0.281$ sec.	31
Fig 4.1 Particle distributions after collapse of dam at time $t = 0:1, 0.2, 0.5,$ and $1.0s$	37
Fig 4.2 The relationship between the non-dimensional leading edge and time after a dam-break of water and mud-flow.....	37
Fig 4.3 Model setup performed by Kato et al. (2012).	38
Fig 4.4 Schematic sketch of the snow avalanche experiment.	39
Fig 4.5 Model setup performed by Kato et al. (2012), with the different shapes of obstacles....	39
Fig 4.6 Comparison between computation and experiment results at different time steps ($t = 0, 0.5, 1, 2, 3,$ and 4 Sec).....	41
Fig 4.7 shape of the deposition cone in the lower part of the slope (case1).....	42
Fig 4.8 comparison between experimental and numerical results in term of the position of snow leading edge with time (case 1).	42
Fig 4.9 Case of Stake rows with 2 cm spacing: (A) Avalanche propagation, (B) Deposition shape in the simulation and the experiment at $t= 4$ Sec.	43

Fig 4.10 Case of Stake rows with 4 cm spacing: (A) Avalanche propagation, (B) Deposition shape in the simulation and the experiment at $t = 4$ Sec.	43
Fig 4.11 Case of obstacle with notched opening: (A) Avalanche propagation, (B) Deposition shape in the simulation and the experiment at $t = 4$ Sec.	44
Fig 5.1 Comparison between experimental and numerical results: (A) initial shape of sand column; (B) simulated final profile; (C) side view of the simulated final profile; (D) experimental final profile (Lube et al. 2004).	50
Fig 5.2 Typical radial displacements as functions of time.	51
Fig 5.3 Comparison of normalized final deposit height between the simulations and experimental results.	51
Fig 5.4 Schematic sketch of the avalanche experiment	53
Fig 5.5 The different types of obstacles, and areas name	53
Fig 5.6 Comparison between the (A) experimental and (B) numerical results in term of the final deposition shape (case1).	54
Fig 5.7 Comparison between the (A) experimental and (B) numerical results in term of the final deposition shape (case2)	55
Fig 5.8 Comparison between the (A) experimental and (B) numerical results in term of the final deposition shape (case3)	55
Fig 5.9 Position of leading edge with time (case1)	56
Fig 5.10 Experimental set-up showing the flow past a circular cylinder on a chute inclined at an angle ζ to the horizontal.	57
Fig 5.11 Comparison between computation and experiment results at different time steps ($t = 7.4$, and 8.12 dimensionless units) showing the continuation of the time-dependent development of a bow shock and a vacuum boundary.	58
Fig 5.12 Conti- Comparison between computation and experiment results at different time steps ($t = 9.56$, 10.28 , and 12.44 dimensionless units) showing the continuation of the time-dependent development of a bow shock and a vacuum boundary	59
Fig 5.13 a) The Schneefernerhaus at the Zugspitze, Germany at 2700 m on a rather planar mountain slope inclined at an angle approximately 45° . b) A model reproduction together with tetrahedral wedge type avalanche protection.....	60
Fig 5.14 Caparison between experimental and numerical results at three different stages showing the motion of a layer of semolina past and around the obstacle and the Schneefernerhaus building.	62
Fig 5.15 Comparison between (A) the experimental results (scale 1:100), (B) numerical results obtained from the two dimensional NOC scheme and, (C) SPH simulation representing the steady flow past the defence structure.....	62
Fig 5.16 Cross section of the avalanche depth distribution along the line $x = 5.6$ through the top of the pyramid.	63
Fig 5.17 Schematic sketch of the granular avalanche experiment.....	63
Fig 5.18 Comparison between (A) the experimental results, (B) numerical results obtained from the quasi-2d model solution and, (C) SPH simulation representing the steady flow past and around the Forward-facing pyramids at different time steps.	65

Fig 5.19 Comparison between (A) the experimental results, (B) numerical results obtained from the quasi-2d model solution and, (C) SPH simulation representing the steady flow past and around the rearward-facing pyramids at different time steps.....	66
Fig 5.20 Conti-Comparison between (A) the experimental results, (B) numerical results obtained from the quasi-2d model solution and, (C) SPH simulation representing the steady flow past and around the rearward-facing pyramids at different time steps.....	67
Fig 6.1 Sketch of the Louvain dambreak experiment's initial set-up.....	74
Fig 6.2 Snapshots of the Louvain experiments (t=0.25 ,0.5, 0.75, 1.0 Sec) compared with SPH simulations.....	75
Fig 6.3 Schematic diagram for hydraulic experiment	76
Fig 6.4 Comparison between experiment and analysis result.....	77

Chapter 1

Introduction

1.1. BACKGROUND AND MOTIVATION

Geo-disasters accompanied by large deformation and failure of geomaterials are a regular occurrence around the world. These include landslides, snow avalanches, debris flows, dam break, soil liquefaction, seepage damage, devastating volcanic ash, and rapid granular flow. Such disasters cause serious damage to infrastructure, resulting in casualties and serious loss of life and property which lead to high economic losses.

To reduce the damage, one of the priorities for governments and researchers is to determine the probability of geo-disasters occurring, devise hazard maps, and take protective measures. Therefore, study of large deformation and flow failure of geomaterials is of great significance to disaster prevention and for design effective defenses to save lives as well as provide a huge economic benefit.

Numerical simulation is a powerful tool, playing an increasingly important role in solving complex problems. The smoothed particle hydrodynamics (SPH) method, a mesh-less hydrodynamics technique, was selected and applied to the modeling of large deformation and post-failure behavior of geomaterials in geo-disasters with some success.

The main aim of this study is to develop 2D and 3D models based on the SPH method, and provide a general view of SPH applications for solving a range of large deformation and failure problems, such as dam breaks, snow avalanches, erosion damage, damage from rapid granular flow. This study selects some typical examples and describes them in detail.

1.2. THE ROLE OF NUMERICAL SIMULATION

In the past, there have been two methodical approaches to uncovering the laws of nature: the practical and the theoretical. The practical approach seeks to discover physical laws through observation aided by experiments and various devices and measuring instruments. The theoretical approach converts the laws of nature to relationships between mathematical quantities, most often employing the language of differential and integral calculus to describe how certain quantities change depending on others. Both approaches, however, have their shortcomings.

Beside the practical and theoretical approaches, numerical simulation has established itself in recent years as a third approach connecting the two traditional ones. With the development of computer technology, numerical simulation has been more and more widely used to simulate complex physical phenomena in science and engineering. Numerical Simulation translates the important aspects of a physical problem into a discrete form of mathematical description, and solves the problem on a computer. Also, it plays an important role in providing a validation of theories and it acts also as a bridge between the experimental models and the theoretical.

Recent dramatic improvements of computers in terms of memory size and computing speed permit ever more realistic simulations, so “practitioners” are increasingly able to reproduce their experiments on a computer. Modifications in these experiments can be made with just a few changes in a computer program rather than the often costly and time-consuming changes

to an experimental apparatus that were previously necessary. Computed data are then processed by visualization techniques so that it can be interpreted. Many shortcomings of both the experimental and the theoretical approaches may be overcome by numerical simulation.

1.2.1. Solution steps of general Numerical Simulations

Numerical simulation is characterized by the following procedure. After the physical phenomena observed, mathematical models are established with some possible simplifications and assumptions. These mathematical models are usually expressed in the form of governing equations (ordinary differential equations or partial differential equations), with proper boundary and initial conditions.

To solve the governing equations numerically, the problem domain should be divided into discrete components, and then the domain discretized using a suitable technique. After domain discretization, the original physical equations can be changed into a set of algebraic equations or ordinary differential equations, which can be solved using the existing numerical routines.

In conventional methods, the physical domain is discretized into meshes. The meshes are fixed in the domain (Eulerian approach) or attached to the material and move in the domain (Lagrangian approach). The meshes are defined in three forms, including, connected nodes in the finite difference (FD) method, volumes (cells) in the finite volume (FV) method and elements in the finite element (FE) method. The meshes are used for transforming governing differential equations of physical phenomena (in physical domains) into a set of algebraic equations (in discretized computational domains).

Applying of a numerical simulation includes translating the domain decomposition and numerical algorithms into a computer code using a programming language. In coding a computer program, the accuracy, and efficiency are two very important considerations. Before applying a numerical simulation, the code should be verified to reproduce sets of experimental data, or exact results from other methods for benchmark problems.

1.3. GRID-BASED SOLVERS OF NAVIER-STOKES EQUATION

There are two fundamental frames for describing the governing equations: the Eulerian description and the Lagrangian description. The Eulerian description is a spatial description that corresponds to the Eulerian grid, which is a grid fixed in space. In the Eulerian grid-based solvers, the discretization of the governing equations is performed on the fixed Eulerian grid, while an additional free-surface tracking model is introduced to track the free-surface. On the contrary, the Lagrangian description is a material description leading to the Lagrangian grid which is a movable grid. In the Lagrangian grid-based solvers, the Lagrangian grid is gradually deformed to fit its edges to the water surface profile.

1.3.1. Lagrangian Grid-based solver

In the Lagrangian grid-based methods such as the well-known and widely used FEM, the grid is fixed to or attached to the material in the entire computation process, and therefore it moves with the material as illustrated in **Fig. 1.1**.

The Lagrangian grid-based solvers of the governing equations are computationally efficient and accurate since:

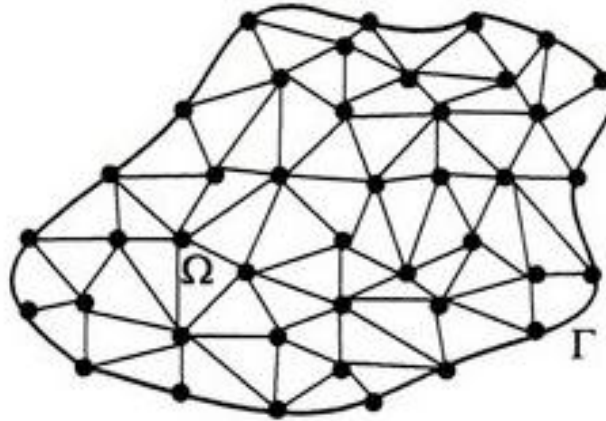


Fig.1.1 Lagrangian mesh/cells/grids for a shaped charge detonation simulation

- 1- The grid is needed only within the computational domain
- 2- No convective term exists in the Lagrangian description of the Navier-Stokes equation; hence, the code is conceptually simpler and faster.
- 3- The boundary conditions at free surfaces, moving boundaries, and material interfaces can be well imposed because of the existence of grid nodes along the boundaries and material interfaces.

However, the main disadvantage of Lagrangian grid-based solvers is the problem of grid (mesh) distortion that makes such methods, improper for solving free-surface fluid flows with large deformations. When the grid is severely distorted, the accuracy of solution is highly affected.

Moreover, the time step of calculation, which is controlled by the smallest element size, can become too small and may even cause the breakdown of computation. To overcome this problem, the Arbitrary Lagrangian-Eulerian (ALE) approach (Hirt et al., 1974) which combines the use of the two reference frames, was proposed. This approach allows for both a flexible grid and a grid that allows the fluid to flow through it. The ALE method is useful in solving a variety of challenging problems such as fluid-structure interactions; nevertheless, it does not yield accurate results when large deformations (Li and Liu, 2002) or fragmentations (Gotoh et al., 2005) exist. In addition, the convective transport effects in ALE often lead to spurious oscillation that needs to be stabilized by for example an artificial diffusion. In other cases, a mesh may carry an inherent bias in numerical simulations, and its presence becomes a nuisance in computations.

1.3.2. Eulerian Grid-based solver

Contrary to the Lagrangian grid, the Eulerian grid is fixed on the space, in which the simulated object is located and moves across the fixed mesh cells in the grid (Illustrated in **Fig. 1.2**).

Since the Eulerian grid is fixed in space and time, large deformations in the fluid do not cause any deformation in mesh and consequently do not lead to same numerical problems as in the Lagrangian grid-based solvers.

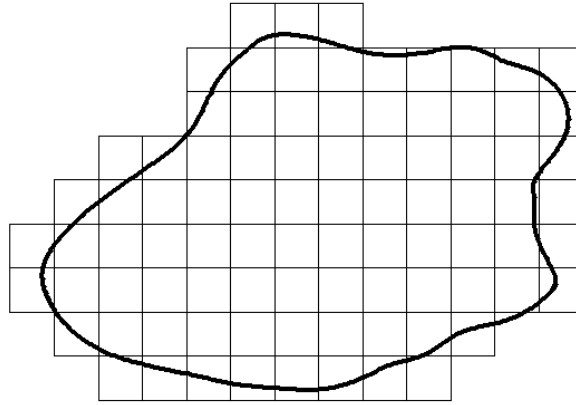


Fig.1. 2 Eulerian mesh/cells/grids for a shaped charge detonation simulation

Nevertheless, the position of free surfaces is not easy to be determined and is dependent upon the appropriate selection of free-surface tracking model. The MAC (Harlow and Welch, 1965) and VOF (Hirt and Nichols, 1981) methods are two of the most popular and robust free-surface tracking models applied in the Eulerian solvers. The former uses marker particles to define the free surface, while the latter solves a transport equation for the volumetric occupation rate of the fluid. These methods have been successfully applied to a variety of flow problems involving free surface fluid flows such as wave-structure interaction (e.g. Lohner et al., 2006) and breaking waves (e.g. Lin and Liu, 1998 and Hieu et al., 2004). Nevertheless, as in both MAC and VOF methods, the Navier-Stokes equations are solved on a fixed Eulerian grid, such methods have a drawback of numerical diffusion arising from the discretization of advection terms on the basis of a fixed grid. The numerical diffusion becomes significant when the free surface experiences large deformations and especially when the fragmentation and coalescence of fluid exist. Some algorithms such as the CIP (Constrained Interpolation Profile; Yabe et al., 2001) method have been proposed to suppress the numerical diffusion caused by the advection terms; nonetheless, all of the proposed algorithms would further increase the complexity of the amputation procedure for simulation of free-surface fluid flows.

1.3.3. Combined Lagrangian and Eulerian Grids

Different but complementary features of the Lagrangian and Eulerian descriptions suggest that it would be computationally beneficial to combine these two descriptions so as to strengthen their advantages and to avoid their disadvantages. This idea has led to the development of two complicated approaches that apply both the Lagrangian and Eulerian descriptions: the Coupled Eulerian Lagrangian (CEL) (Hans, 1999) and the Arbitrary Lagrange Eulerian (ALE) (Benson, 1992).

1.4. MESH-FREE BASED SOLVERS OF NAVIER-STOKES EQUATION

A recent interest has been focused on the development of the next generation computational methods namely, the gridless or mesh-less methods that are expected to become superior to the conventional grid-based methods. The main idea behind the gridless methods is to obtain accurate and stable numerical solutions for integral equations of Partial Differential Equations

with all kinds of possible boundary conditions with a set of arbitrarily distributed calculation points (nodes or particles) without the use of any mesh that provides the connectivity of these nodes or particles. In the gridless methods, calculation points are located in the vicinity of the target calculation point and they can either be fixed (Eulerian approach) or moveable (Lagrangian approach). The Lagrangian gridless method is called the particle method.

1.4.1. Particle methods, the Lagrangian gridless solvers

In particle methods, a set of finite number of particles is used to represent the state of a system and its evolution. In case of Computational Fluid Dynamics (CFD), particles are supposed to represent the fluid and its motion, while each particle possesses a set of field variables such as mass, momentum, position, etc. The evolution of the system is determined by the underlying equations of fluid motion, i.e. the momentum equation and the continuity equation are discretized by the moving particles. Particle methods have many advantages over conventional grid-based methods, the most important of which can be summarized as follows:

- 1- In particle methods, the continuum is discretized by particles without a fixed connectivity. As a result, treatment of large deformations is much easier compared to grid-based methods.
- 2- Features of the entire physical system can be easily obtained through tracing the motion of particles. Consequently, identifying free surfaces, moving interfaces and deformable boundaries is no longer a difficult task.
- 3- Convection is directly calculated without numerical diffusion because of fully Lagrangian treatment of particles.
- 4- More complex geometries and physics in the fluid dynamics can be analyzed; for example fluid fragmentation and coalescence.
- 5- Refinement of the particles is much easier to perform than a refinement of the mesh.

Particle methods have been classified based on the length scale and the mathematical model used. The particles can vary from very small (nano or micro) scale, to meso scale and to macro scale, dividing the gridless particle methods into three categories of Microscopic (e.g. MD; Molecular Dynamics), Mesoscopic (e.g. DPD; Dissipative Particle Dynamics, lattice gas Cellular

Automata) and Macroscopic (e.g. SPH; Smoothed Particle Hydrodynamics, PIC; Particle In Cell,

MPS; Moving Particle Semi-implicit). Another categorization is based on the mathematical model used, where the particle methods are divided into two branches of probabilistic or deterministic. Probabilistic particle methods (e.g. Molecular Dynamics, Direct Simulation Monte Carlo) are inherent in probabilistic nature based on statistical principles; on the other hand, deterministic particle methods (e.g. MPS, SPH) deal directly with the governing equations of physical law.

As one of the earliest particle methods, the Smoothed Particle Hydrodynamics (SPH; Lucy, 1977; Gingold and Monaghan, 1977) was initially developed as a probabilistic method for astrophysical applications. However, since then it has been modified and extended as a deterministic particle method to model the macroscopic continuum problems of computational solid (e.g. Libersky and Petschek, 1991) and fluid mechanics (e.g. Monaghan, 1994). The SPH method has been applied to solve the Navier-Stokes equation for simulating incompressible free-surface fluid flows by treating the flow as weakly (or slightly) Compressible (WCSPH; e.g. Morris et al., 1997) or strictly Incompressible (ISPH; e.g. Shao and Lo, 2003). Another macroscopic deterministic particle method is the Moving Particle

Semi-implicit (MPS; Koshizuka et al., 1996) method which was initially developed for the simulation of incompressible free-surface fluid flows. Unlike gridless Galerkin methods which estimate the weak form of PDEs, both MPS and SPH methods approximate the strong form of PDEs by particle-based discretizations through using specific mathematical models for differential operators. Both methods have proven useful in a wide variety of engineering applications; yet, there are some deficiencies associated with these particle methods:

1. An unavoidable pressure fluctuation exists in the particle methods (Gotoh et al., 2005) unless proper modifications or corrections are introduced.
2. A Particle-based discretization may violate the exact conservation of some physical principles such as momentum (Khayyer et al., 2008; Khayyer and Gotoh, 2008a, b) and mechanical energy.
3. The adjustment of resolution is not easy in the particle methods, since uniform particles are utilized. Additional particles might be injected to the place where high resolution is needed; however, those particles do not stay in their initial position because of the advection (Gotoh et al., 2005).
4. Inflow and outflow of fluid are not permitted in the particle methods since they are Lagrangian methods (Premoze et al., 2003). Nevertheless, they can be combined with an Eulerian approach to handle inflow and outflow (Premoze et al., 2003).

1.4.2. Eulerian gridless solvers

Eulerian gridless solvers do not have problems with inflow/outflow boundary conditions or resolution adjustment which are difficult to handle in particle methods. Meanwhile, the problem with Eulerian gridless solvers arises when they are supposed to simulate a convection-dominated system, a frequently occurring situation in fluid dynamics. In such a case, as a result of the Eulerian discretization of advection terms using fixed nodes, the numerical diffusion becomes dominant and significantly affects both the accuracy and stability of the calculation. To overcome the problem with stability, Fries and Matthies (2005) have proposed gridless Petrov-Galerkin methods by employing Petrov-Galerkin-Type stabilization techniques in a gridless solver of Navier-Stokes equation. Meanwhile, the problem of artificial numerical diffusion is still present in Gridless Petrov-Galerkin methods. As an alternative to simulate problems with inflow/outflow boundary conditions using particle methods, Yoon et al. (1999) proposed a Lagrangian-Eulerian method, namely, MPS with a Meshless Advection using Flow directional Local grid (MPS-MAFL). For the Lagrangian phase, original differential operator models of MPS method were used, while, for the Eulerian phase, a high-order finite difference scheme was utilized to approximate the convection of fluid.

In the present study, a fully Lagrangian gridless method, namely, weakly compressible SPH (SPH) method is selected and improved as reliable numerical tools for accurate simulation of geo-disasters problems accompanied with large deformations. The major outcomes of the thesis are summarized in the next section.

1.5. STRUCTURE OF THE THESIS

The thesis has seven chapters, with Chapter 1 as the introduction. This describes certain catastrophic Geo-disasters and their characteristics and introduces some background knowledge of numerical simulation. The features and limitations of the grid-based numerical

methods are discussed. The basic ideas of mesh-free and particle methods are briefed. Some general features of the mesh-free particle methods, especially smoothed particle hydrodynamics, are described. The inventions, development, applications of the SPH method are briefly addressed.

Chapter 2 provides the fundamentals of the SPH method such as the basic concepts and the essence of SPH formulations which will be useful in the later Chapters. The next three chapters focus on SPH applications to Geo-disaster modeling and analysis, including fluid flow problems involve free surfaces in complex geometry such as a collapse of a water column with a rigid obstacle, and dam break on a wet bed (Chapter 3), real snow avalanche as a Bingham fluid flow with different types of obstacles (Chapter 4), rapid free-surface granular flow past different types of obstructions (Chapter 5).

In Chapter 6, the advantages of SPH will be exploited to simulate the interaction between water and soil, in order to simulate soil scour and erosion behind the seawall. Finally, in chapter 7, general conclusions are presented.

Chapter 2

SPH Concept and Formulation

The Smoothed Particle Hydrodynamics (SPH) method is one of the earliest mesh-free methods of pure Lagrangian description, and has been widely used in many fields of engineering. In this chapter, the development history, basic concept, and essential formulations of SPH are introduced.

2.1 BASIC CONCEPT OF SPH

SPH is a true mesh-free particle method based on a pure Lagrange description, which was first developed to solve astrophysical problems in three-dimensional open space, particularly polytopes (Lucy 1977; Gingold and Monaghan 1977). Later, Monaghan and Lattanzio (1985) summarized basic concepts of discretization for the governing equations, including continuity, momentum, and energy. Selection of the smoothing kernel function and techniques used in deriving SPH formulations for complex partial differential equations (PDEs) has been discussed.

Considering the instability of the SPH numerical solution, Swegle et al. (1995), and Chen et al. (1999) proposed stabilization schemes. Johnson and Beissel (1996) put forth a calculation method for stress. The core of this method is fully implied in the three words Smoothed Particle Hydrodynamics. “Smoothed” represents the smoothed approximation nature of using weighted averages of neighboring particles for stability. “Particle” indicates that the method is based on mesh-free particle theory. The computing domain is treated using a discrete particle instead of continuous entities. “Hydrodynamics” points to the fact that the SPH method was first applied to hydrodynamics problems. The basic concept of SPH is that a continuous fluid is represented by a set of arbitrarily distributed particles. The moving particles possess material properties. By providing accurate and stable numerical solutions of hydrodynamic equations and tracking movements of each particle, the method can describe the mechanical behavior of an entire system.

Therefore, the key facet of SPH is how to solve the PDEs using a series of arbitrarily distributed particles carrying field variables, such as mass, density, energy, and stress tensors. In an actual situation, it is usually difficult to obtain an analytical solution of these PDEs, which gives rise to the need for numerical methods for them. The first step is to discretize the problem domain of the PDEs. Then, there is a need to approximate the variable function and its derivative for the arbitrary particles. Finally, the approximate functions are applied to the PDEs to obtain a series of discretization Ordinary Differential Equations (ODEs), which are only related to time.

The core concept of the SPH method can be summarized as follows:

1. In the SPH model, the problem domain is replaced by a series of arbitrarily distributed particles. There is no connectivity between these particles, which reflects the mesh-free nature of this method. The major concern of this method is how to ensure the stability of

numerical solutions, especially in applying the arbitrarily distributed particles to solve problems with derivative boundary conditions.

2. One of the most important steps is to represent a function in continuous form as an integral representation using an interpolation function. This step is usually called kernel approximation. The integral has a smoothing effect, similar to the weak form equations. In reality, the kernel approximation stabilizes numerical calculation of the SPH.
3. Another important step is that the value of a function at computing particle i is approximated using the averages of function values at all neighboring particles within the horizon of particle a . This step is termed particle approximation. The role of this approximation is to generate banded or sparse discretized system matrices, which are extremely important for calculation efficiency.
4. Using an explicit integration algorithm to solve differential equations can achieve fast time stepping. The time history of all field variables for all the particles can also be obtained. An appropriate method to determine the time step must be selected in the SPH method.

In summary, the mesh-free, adaptive, stable, and Lagrangian-description SPH method can be used as a dynamic problem solver.

2.2 SPH APPROXIMATION

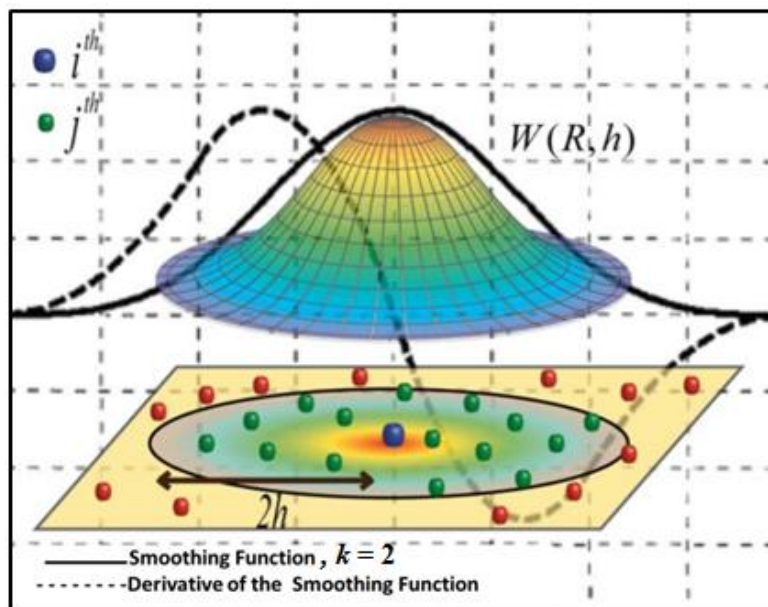


Fig 2.1 SPH concept figure (The influence domain is circular with a radius of kh , and the cubic spline kernel and its first derivative)

The SPH method is built on interpolation theory, with two essential aspects. The first is smoothed (or kernel) approximation, which represents a function in continuous form as an integral representation. The other is particle approximation, which represents the problem domain using a set of discrete particles within the influence domain to estimate field variables for those computing particles. The value of a function at computing particle i is approximated using the average of those values of the function at all particles in the influence domain of particle a , weighted by the smoothing function. The radius of influence domain is defined as h , depending on the precision of specific problems. As shown in **Fig. 2.1**, W is the smoothing kernel function, i is the computing particle, and j is the neighboring particles.

2.2.1 Kernel Approximation

The SPH method is a continuum-scale numerical method. The material properties $f(x)$, at any point x in the simulation domain are calculated according to an interpolation theory over its neighboring particles which are within its influence domain Ω as shown in **Fig. 2.1**, through the following formula,

$$\langle f(x) \rangle = \int_{\Omega} f(x') W(x - x', h) dx' \quad (2.1)$$

where h is the smoothing length defining the influence domain of the kernel estimate and $W(x - x', h)$ is the smoothing function, which must satisfy three conditions (Liu and Liu, 2003): the first condition is the normalization,

$$\int_{\Omega} W(x - x', h) dx' = 1 \quad (2.2)$$

the second one is the Delta function condition,

$$\lim_{h \rightarrow 0} W(x - x', h) = \delta(x - x') \quad (2.3)$$

and the third condition is the compact condition,

$$W(x - x', h) = 0 \quad \text{when } |x - x'| > kh \quad (2.4)$$

where k is a constant depending on the type of smoothing function. There are many possible types of smoothing functions, which can satisfy the aforementioned conditions and will be discussed in the following section.

The ‘kernel estimation’ for the spatial derivative of a vector quantity $\nabla \cdot f(x)$ is obtained simply by substituting $f(x)$ with $\nabla \cdot f(x)$ into an equation (2.1), which gives:

$$\begin{aligned} \langle \nabla f(x) \rangle &= \int_{\Omega} [\nabla \cdot f(x')] W(x - x', h) dx' \\ &= \int_{\Omega} \nabla \cdot [f(x') W(x - x', h)] dx' - \int_{\Omega} f(x') \cdot \nabla W(x - x', h) dx' \end{aligned} \quad (2.5)$$

Using the divergence theorem, the first integral on the right-hand side of the equation (2.5) can be converted into an integral over the surface S of the domain inside of integration Ω ,

$$\langle \nabla f(x) \rangle = \int_S f(x') W(x - x', h) n dS - \int_{\Omega} f(x') \cdot \nabla W(x - x', h) dx' \quad (2.6)$$

where n is the unit vector normal to the surface S . Since the smoothing function W is defined to have compact support, the surface integral on the right-hand side of the equation (2.6) is zero. Therefore, the ‘kernel estimation’ of the spatial derivative $\nabla \cdot f(x)$ now becomes,

$$\langle \nabla f(x) \rangle = - \int_{\Omega} f(x') \cdot \nabla W(x - x', h) dx' \quad (2.7)$$

Equation (2.7) is the most commonly used form of function approximation for $\nabla f(x)$.

2.2.2 Particle Approximation

In the SPH method, the calculation domain is represented by a finite number of particles, which carry mass and all field variable information such as density, pressure, stress, etc. (Liu and Liu, 2003). Assuming that the mass is flowing with density $\rho(x)$, it is divided into N volume elements. Masses of the volume elements are $m_1, m_2, m_3, \dots, m_N$, respectively, and positions of corresponding centers of mass are $x_1, x_2, x_3, \dots, x_N$, respectively. Accordingly, the continuous integral representation for $f(x)$ is approximated in the following form:

$$\langle f(x) \rangle = \int_{\Omega} f(x') W(x - x', h) dx' \approx \sum_{j=1}^N f(x_j) W(x - x_j, h) \frac{m_j}{\rho_j} \quad (2.8)$$

Using the equation (2.8), the approximation function for any particle i can be written as,

$$\langle f(x_i) \rangle = \sum_{j=1}^N \frac{m_j}{\rho_j} f(x_j) W_{ij} \quad (2.9)$$

where $W_{ij} = W(x - x_j, h)$

Equation (2.9) expresses that the value of any function at particle i is approximated utilizing the weighted average of all values of this function for all particles in the influence domain of particle i . Following the same argument, the particle approximation of the spatial derivative for a function at any particle i is,

$$\langle \nabla f(x_i) \rangle = \sum_{j=1}^N \frac{m_j}{\rho_j} f(x_j) \cdot \nabla_i W_{ij} \quad (2.10)$$

where

$$\nabla_i W_{ij} = \frac{x_i - x_j}{r_{ij}} \frac{\partial W_{ij}}{\partial r_{ij}} = \frac{s x_{ij}}{r_{ij}} \frac{\partial W_{ij}}{\partial r_{ij}} \quad (2.11)$$

Equation (2.10) states that the value of the gradient of a function at particle i is approximated using the average of those values of the function at all the particles in the support domain of particle i weighted by the gradient of the smoothing function.

In summary, for a given particle i , according to the particle approximation, the value of a function and its derivative for particle i can be calculated through equations 2.9 and 2.10 respectively. For example, if we substitute the function $f(x)$ with the density function ρ in equation (2.9), the SPH approximation of the density is obtained as follows,

$$\rho_i = \sum_{j=1}^N m_j W_{ij} \quad (2.12)$$

2.3 NUMERICAL ASPECTS OF THE SPH MODEL

2.3.1 Initial Settings

Appropriate initial settings should be made for different computational problems. For specific requirements of varying computing cases, the initial state, including the kernel function, particles coordinates, initial particle spacing, density, pressure, and velocity should be determined at the beginning of the calculation. The smoothing length (h) also should be chosen according to the weighting function type. Time-step (Δt) control is dependent on the CFL condition, the forcing terms and the viscous diffusion term (Monaghan; 1989). A variable time step Δt is calculated according to Monaghan and Kos (1999):

$$\Delta t = 0.3 \times \min(\Delta t_f, \Delta t_{cv}); \Delta t_f = \min\left(\sqrt{\frac{h_i}{|f_i|}}\right); \Delta t_{cv} = \min \frac{h_i}{c_i + \max \left| \frac{h_j v_{ij} r_{ij}}{r_{ij}^2} \right|} \quad (2.13)$$

Here Δt_f is based on the force per unit mass $|f_i|$, and combines the Courant and the viscous time-step controls.

2.3.2 Neighboring Particle Searching Algorithm (linked- list)

As mentioned above, SPH is a mesh-free method based on interactions with the closest neighboring particles. During the movement of each particle, the spatial location is constantly changing. Therefore, the neighbor list of each particle should be updated every time step. Therefore, creation of the neighbor list is important for high performance of the code. The efficiency of the SPH model strongly depends on the construction and use of this list.

There are different types of nearest neighboring particles searching approaches popular in SPH such as, all-pair search, linked-list search algorithm, and tree search algorithm. The linked-list search algorithm works well for cases with spatially constant smoothing length and we will use it in this study.

As pointed by Monaghan and Gingold (1983), substantial savings in computational time can be achieved by using cells as a bookkeeping device. If all the particles are assigned to cells and identified through linked- lists, the computational time can be greatly reduced since the nearest neighboring particles searching process is only necessary for a certain group of particles. Monaghan (1985) described the procedure for carrying out the nearest neighboring particle searching using linked-list.

In the implementation of the linked-list algorithm, a temporary mesh is overlaid on the problem domain (**Fig. 2.2**). The mesh spacing is selected to match the dimension of the support domain. For smoothing kernels having compact support of kh , the mesh spacing should be set to kh . Then for a given particle i its nearest neighboring particles can only be in the same grid cell or the immediately adjoining cells. Therefore, the search is confined only over 9 or 27 cells for two- or three-dimensional space, respectively, if $k = 2$. The linked-list algorithm allows each particle to be assigned to a cell and for all the particles in a cell to be chained together for easy access. If the average number of particles per cell is sufficiently small, the complexity of the linked-list algorithm is of order of (N). Thus, for a particle located inside a cell, only the interactions with the particles of neighboring cells need to be considered. In this way the number of calculations per time step and, therefore, the computational time diminishes considerably, from N^2 operations to $N \log N$, where N is the number of particles.

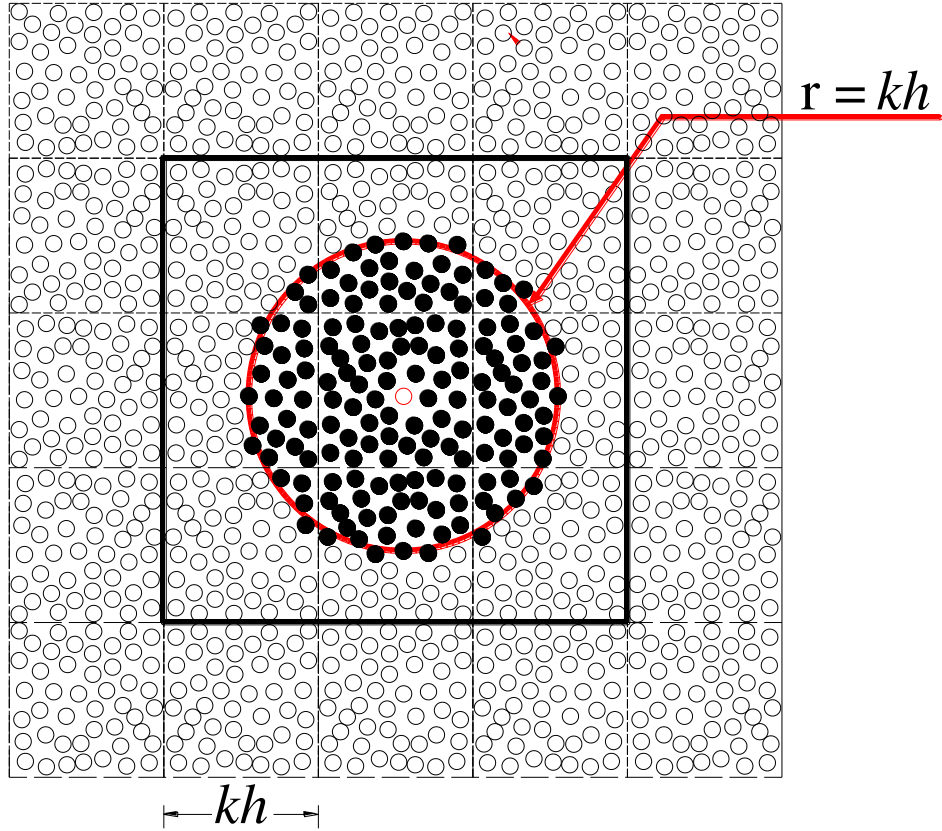


Fig 2.2 Set of neighboring particles in 2D. The possible neighbors of a fluid particle are in the adjacent cells, but this only interacts with particles marked by black dots.

2.3.3 Kernel Function

The performance of an SPH model is critically dependent on the choice of the weighting functions. They should satisfy several conditions such as positivity, compact support, and normalization. Also, $W_{\alpha\beta}$ must be monotonically decreasing with increasing distance from particle i and behave like a delta function as the smoothing length, h , tends to zero (Monaghan, 1992; Benz, 1990; Liu, 2003). Kernels depend on the smoothing length, h , and the non-dimensional distance between particles given by $R = (x - x')/h$, $(x - x')$ being the distance between particles i and j . The parameter h , often called influence domain or smoothing domain, controls the size of the area around particle i where the contribution from the rest of the particles cannot be neglected.

The following lists some of the most frequently used kernel functions in the SPH literature.

1) Gaussian:

$$W(x - x', h) = \left[\frac{1}{\sqrt{\pi} h} \right]^d \exp \left[-\frac{(x - x')^2}{h^2} \right] \quad (2.14)$$

where d represents the dimension of space.

2) Super Gauss kernel

$$W(x - x', h) = \left[\frac{1}{\sqrt{\pi h}} \right]^d \left[\frac{5}{2} - \frac{(x - x')^2}{h^2} \right] \exp \left[-\frac{(x - x')^2}{h^2} \right] \quad (2.15)$$

3) Exponential kernel

$$W(x - x', h) = \left[\frac{1}{8\pi h^3} \right]^d \exp \left[-\frac{(x - x')^2}{h^2} \right] \quad (2.16)$$

4) Quadratic:

$$W(x - x', h) = \alpha_d \times \left[\frac{3}{16} R^2 - \frac{3}{4} + \frac{3}{4} \right] \quad 0 \leq R \leq 2 \quad (2.17)$$

where α_d is $2/(\pi h^2)$ in 2D and $5/(4\pi h^3)$ in 3D

5) Cubic spline:

$$W(R, h) = \alpha_d \times \begin{cases} 1.5 - R^2 + 0.5R^3 & 0 \leq R < 1 \\ (2 - R)^3 / 6 & 1 \leq R < 2 \\ 0 & R \geq 2 \end{cases} \quad (2.18)$$

where

$$\alpha_d = \begin{cases} 15/7\pi h^2 & \text{2D space} \\ 3/2\pi h^3 & \text{3D space} \end{cases} \quad (2.19)$$

The cubic spline function has been the most widely used smoothing function in the SPH literature, since it resembles a Gaussian function while having a narrower compact support. In this study, the cubic spline function was selected as the kernel function.

2.3.4 Boundary Treatment

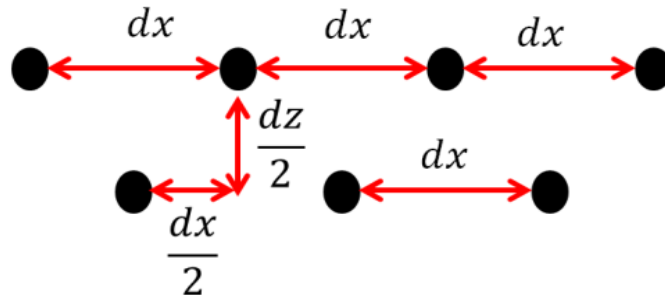


Fig 2.3 Arrangement of boundary particles

In this study, a dynamic boundary condition is used to represent the boundary particles, which are forced to follow the governing equations (continuity, momentum and state equations), but they are fixed. At the point when the particles are near to the boundary the density of the

boundary particles increases according to the continuity equation, which leads to an increase in the pressure following the equation of state. Subsequently, the force exerted on the approaching particles increases because of the pressure term in the momentum equation by generations of repulsion between the material particles and the boundary particles (Dalrymple, and Knio, 2001). The boundary particles are set in a staggered manner in order to prevent the particle leakage as shown in **Fig.2.3**.

2.3.5 Integration Schemes

To calculate the forces acting on the SPH particles after discretization, a neighbor list is created for each particle in the current configuration. In the subsequent calculations, the neighbor list is referred to, so the total force acting on a particle can be determined. Since the SPH method reduces the original PDEs to sets of ODEs, any stable time-step algorithm for ODEs can be introduced. The Predictor- Corrector algorithm introduced here for the time integration to update positions, velocities, and accelerations:

$$\left. \begin{aligned} v_i^{n+1/2} &= v_i^n + (\Delta t/2) * Dv_i(t) \\ \rho_i^{n+1/2} &= \rho_i^n + (\Delta t/2) * D\rho_i(t) \\ x_i^{n+1/2} &= x_i^n + (\Delta/2) * v_i^n \end{aligned} \right\} \quad (2.20)$$

And pressure calculated according to the equation of state as,

$$P_i^{n+1/2} = f(\rho_i^{n+1/2}) \quad (2.21)$$

Values of v , ρ , and x at the midpoint are then estimated using

$$\left. \begin{aligned} v_i^{n+1/2} &= v_i^n + (\Delta t/2) * Dv_i(t)^{n+1/2} \\ \rho_i^{n+1/2} &= \rho_i^n + (\Delta t/2) * D\rho_i(t)^{n+1/2} \\ x_i^{n+1/2} &= x_i^n + (\Delta t/2) * v_i^{n+1} \end{aligned} \right\} \quad (2.22)$$

Finally, these values are calculated at the end of the time step using

$$\left. \begin{aligned} v_i^{n+1} &= 2 * v_i^{n+1/2} - v_i^n \\ \rho_i^{n+1} &= 2 * \rho_i^{n+1/2} - \rho_i^n \\ x_i^{n+1} &= 2 * x_i^{n+1/2} - x_i^n \end{aligned} \right\} \quad (2.23)$$

And the pressure is calculated from density using:

$$P_i^{n+1} = f(\rho_i^{n+1}) \quad (2.24)$$

where Δt is the time step; and n is the time index. The stability of the Predictor-Corrector scheme is warranted using three criteria for time step. Following Monaghan (1989), the time

step Δt for a simulation chosen to be the minimum from (CFL) condition, the forcing terms and the viscous diffusion term.

2.3.6 Outputs of Calculation

Given the Lagrangian property of the SPH method, information on each particle, such as density, position, velocity, and pressure, can be captured at every time step. According to the actual needs of a study, these variable values can be selectively output, easily visualized, and rapidly analyzed, and time history curves can be readily obtained.

2.4 SUMMARY

SPH is a novel mesh-free particle method based on a pure Lagrangian description. The basic idea of the method is that a continuous fluid is represented by a set of arbitrarily distributed particles. By providing accurate and stable numerical solutions for hydrodynamic equations and tracking the movements of each particle, the mechanical behavior of the full system can be determined. SPH is characterized by a mesh-free, adaptive, and Lagrangian description, which makes it suitable for handling the problems of large deformation and free surfaces.

On a theoretical level, SPH can accurately describe the mechanical process as long as there are sufficient numbers of particles. Although the precision of results depends on particle arrangement, the requirement for this arrangement is much less stringent than the demands of a grid. Without the grid, there is no connectivity between the particles. Therefore, severe mesh distortions caused by large deformation are avoided, thereby improving computational accuracy. In addition, SPH can conveniently handle the interface of different materials. Another advantage of the method is the Lagrangian description, which avoids the difficult interface of the grid and material. Hence, the SPH method is especially suitable for solving complex flow problems. In particular, the method has the following advantages:

- (1) There is no migration term in the PDEs, so the program design is simple and efficient;
- (2) It is easy to track the time history of all field variables for all particles;
- (3) It can automatically exert the boundary condition to track the free surfaces, material interfaces, and moving boundaries;
- (4) It is easy to handle irregular and complex geometric shapes. SPH is therefore a novel and promising method for computational fluid mechanics.

Chapter 3

Two-dimensional and Three-dimensional Numerical Simulations of Free Surface Flow Problems Using SPH

Studying free surface flows in hydrodynamics are very important to industrial and environmental fields, but they are difficult to simulate because boundary conditions are required for an arbitrarily moving surface. Because of the successful applications of the SPH method in hydrodynamics, most SPH simulation studies of geo-disaster topics are concentrated in fields related to fluid dynamics, such as dam breaks and coastal engineering.

Usually, fluid flow problems often involve free surfaces in complex geometry and in many cases are highly transient. Examples in hydraulics are flowing over spillways, in rivers, around bridge pilings, flood overflows, flows in sluices, and a dam break. A capability of computationally model these types of flows are attractive if such computations can be done accurately and with reasonable computational resources. To be useful, simulations should be much faster and less expensive than using physical models. In this chapter, we consider the application of the smoothed particle hydrodynamics (SPH) method to free surface problems. Numerical simulations for three benchmark tests, dam break test, a collapse of a water column with a rigid obstacle, and dam break on a wet bed, are taken into consideration to examine the capability of the SPH method. Also, a comparison between the SPH method and the original version of the Moving Particle Semi-implicit (MPS) were done in order to stand on the difference between the two models.

3.1 INTRODUCTION

During a dam failure, a huge amount of water stored in the reservoir suddenly rushes downstream, destroying trees, dikes, buildings, and bridges. It is important to predict the effects of catastrophic dam break floods to minimize the human and financial toll. Because of the mesh-free, Lagrangian and particle nature of the SPH method, the technique has been considered and applied widely for studying free surface flows in complex geometry, three benchmark tests to examine the capability of the SPH method are selected.

3.2 GOVERNING EQUATIONS

The governing equations of water in the framework of SPH consist of continuity and momentum conservation equations as follows:

$$\frac{D\rho}{Dt} = -\rho \frac{\partial v^\alpha}{\partial x^\alpha} \quad (3.1)$$

$$\frac{Dv^\alpha}{Dt} = \frac{1}{\rho} \left(\frac{\partial \sigma^{\alpha\beta}}{\partial x^\alpha} \right) + f^\alpha \quad (3.2)$$

where α and β denote the Cartesian components x , y and z with the Einstein convention applied to repeated indices; ρ is the density; v is the velocity; $\sigma^{\alpha\beta}$ is the total stress tensor, f^α is the component of acceleration caused by external force, which is the gravity force in this study and D/Dt is the material (total) derivative, which is defined by:

$$\frac{D}{Dt} = \frac{\partial}{\partial t} + v^\alpha \frac{\partial}{\partial x^\alpha} \quad (3.3)$$

The stress tensor, $\sigma^{\alpha\beta}$, normally consists of two parts: an isotropic pressure P and a viscous shear stress, which is proportional to the shear strain rate denoted by ε through the viscosity μ ,

$$\sigma^{\alpha\beta} = -P\delta^{\alpha\beta} + \mu\varepsilon^{\alpha\beta} \quad (3.4)$$

where:

$$\varepsilon^{\alpha\beta} = \frac{\partial v^\alpha}{\partial x^\beta} + \frac{\partial v^\beta}{\partial x^\alpha} - \frac{2}{3} \left(\frac{\partial v^\gamma}{\partial x^\gamma} \right) \delta^{\alpha\beta} \quad (3.5)$$

3.3 DISCRETIZATION OF GOVERNING EQUATIONS

Using the SPH approximation discussed and summarized in chapter two, the system of partial differential equations (3.1) and (3.2) can be converted into the SPH formulations which will be used to solve the motion of fluid particles as follows:

$$\frac{D\rho_i}{Dt} = \sum_{j=1}^N m_j (v_i^\alpha - v_j^\alpha) \frac{\partial W_{ij}}{\partial x_i^\alpha} \quad (3.6)$$

$$\frac{Dv_i^\alpha}{Dt} = \sum_{j=1}^N m_j \left(\frac{\sigma_i^{\alpha\beta}}{\rho_i^2} + \frac{\sigma_j^{\alpha\beta}}{\rho_j^2} \right) \frac{\partial W_{ij}}{\partial x_i^\beta} + f^\alpha \quad (3.7)$$

Similarly, the SPH approximation of shear strain rate $\varepsilon_i^{\alpha\beta}$ for particle i is

$$\begin{aligned} \varepsilon_i^{\alpha\beta} = & \sum_{j=1}^N \frac{m_j}{\rho_j} (v_i^\alpha - v_j^\alpha) \frac{\partial W_{ij}}{\partial x_i^\beta} + \sum_{j=1}^N \frac{m_j}{\rho_j} (v_i^\beta - v_j^\beta) \frac{\partial W_{ij}}{\partial x_i^\alpha} \\ & - \left(\frac{2}{3} \sum_{j=1}^N \frac{m_j}{\rho_j} (v_i^\gamma - v_j^\gamma) \frac{\partial W_{ij}}{\partial x_i^\gamma} \right) \delta^{\alpha\beta} \end{aligned} \quad (3.8)$$

In order to solve Navier–Stokes equations for water the ‘‘equation of state’’ is used to estimate the pressure change of water. Following Monaghan (1994), the pressure can be calculated using the equation of Tait:

$$P = B \left[\left(\frac{\rho}{\rho_0} \right)^\lambda - 1 \right] \quad (3.9)$$

where λ is a constant ($=7$), ρ_0 is the reference density, B is a problem dependent parameter, which sets a limit for the maximum change of the density and will be calculated as

$$B = \frac{100 V_{type}^2 \rho_0}{\lambda}, \quad V_{type} = \sqrt{2 g H} \quad (3.10)$$

where V_{type} the typical speed of water and H is the depth of the water.

3.3.1 Moving the particles

Particles are moved using the XSPH variant. In the applications of the artificial compressibility to incompressible flows, it is useful to use the ‘‘XSPH’’ technique proposed by Monaghan (1989; 1992). In the XSPH, the particle moves in the following way.

$$\frac{dx_i}{dt} = v_i - \varepsilon \sum_{j=1}^N \frac{m_j}{\rho_j} (v_i - v_j) \frac{\partial W_{ij}}{\partial x_i} \quad (3.11)$$

where ε is a constant in the range of $0.0 \leq \varepsilon \leq 1.0$. It is clear that the XSPH technique includes the contribution from neighboring particles, and thus makes the particle move in a velocity closer to the average velocity of the neighboring particles. The XSPH technique, when applied to incompressible flows, can keep the particles more orderly; when applied to compressible flows, can effectively reduce unphysical penetration between approaching particle. In most circumstances $\varepsilon = 0.3$ seems to be a good choice in simulating incompressible flows.

3.3.2 Artificial viscosity

To prevent shock waves and the penetration of particles, an artificial viscosity has been introduced to the pressure term in the momentum equation. The most widely used type is proposed by Monaghan (1985), and specified as follows

$$\pi_{ij} = \begin{cases} \frac{-\alpha \bar{c}_{ij} \phi_{ij} + \beta \phi_{ij}^2}{\bar{\rho}_{ij}} & v_{ij} \cdot x_{ij} < 0 \\ 0 & v_{ij} \cdot x_{ij} \geq 0 \end{cases} \quad (3.12)$$

in which α and β are constants and are taken 0.01, 1.0 respectively, and c represent the speed of sound. As well as having beneficial effects, artificial viscosity can also introduce unwanted numerical defects in some cases, among which the excess dissipation and false shearing torque in rotating flows (Flebbe et.al., 1994).

3.4 NUMERICAL RESULTS

Three benchmark tests have been considered to assess the performance of the SPH model in simulation of free surface flows, and to show the models capabilities. Dam breaking

(Koshizuka, 2000), a collapse of a water column with a rigid obstacle (Koshizuka, 1995), and dam break on wet bed (Janosi et al., 2004) are used.

3.4.1 Dam breaking

Dam breaking is typically employed to demonstrate the ability of codes to compute transient fluid flow with breaking free surface. The corresponding experiment has been made by Martin and Moyce (1952), and more recently by Koshizuka (2000). The initial water column is 0.146 m wide and 0.292 m high, and the tank is 0.584 m wide. **Fig. 3.1** shows a schematic sketch of the experimental setup.

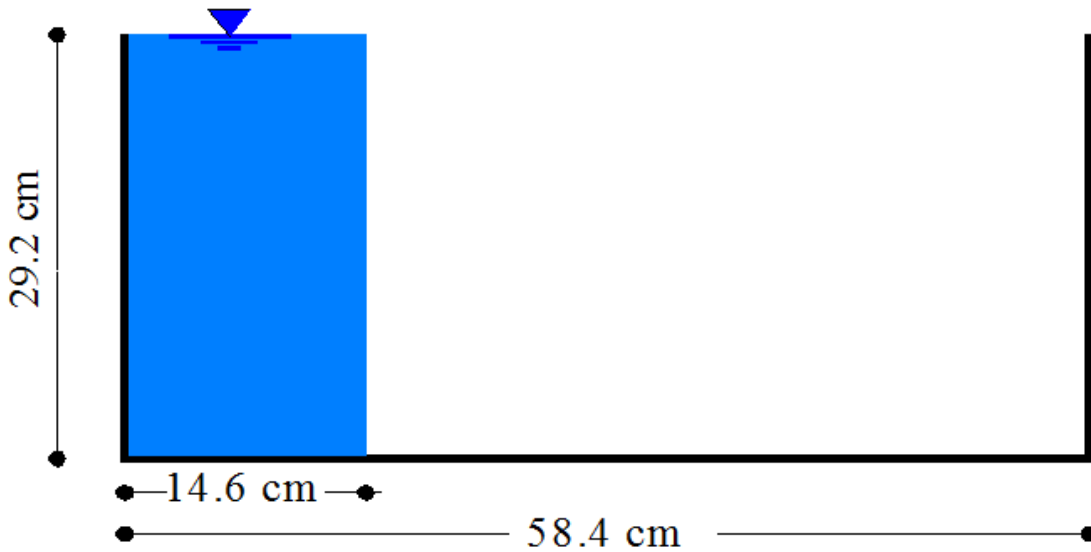


Fig 3.1 Schematic sketch of the experimental setup

3.4.2 Collapse of water column with a rigid obstacle.

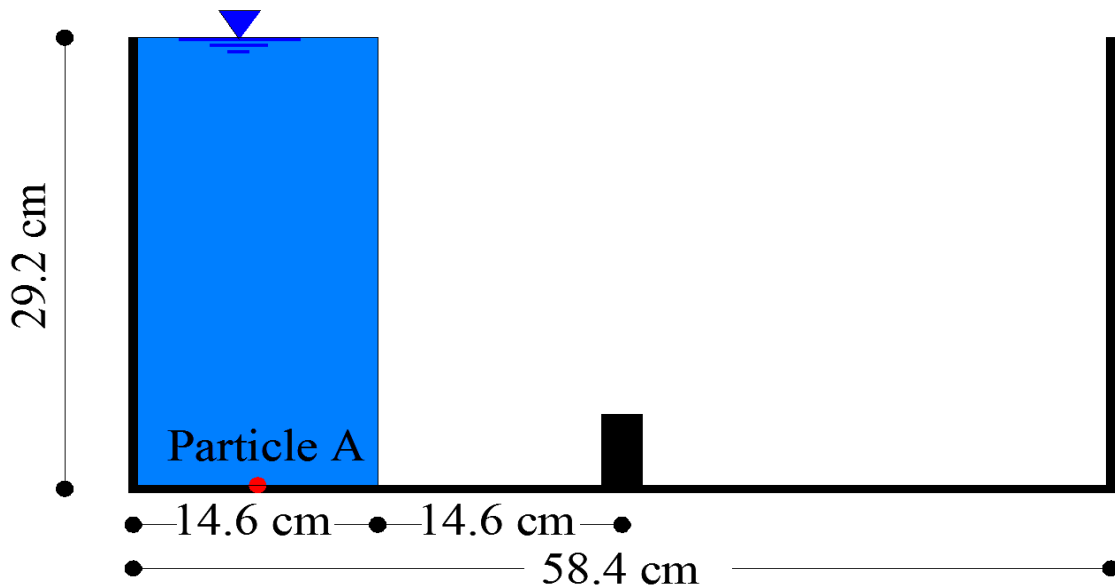


Fig 3.2 Initial geometry, location of the rigid obstacle, and location of point (A)

Fig. 3.2 shows a rectangular tank of 0.584 m wide contains a column of water with 0.146 m wide and 0.292 m high, a rigid obstacle is located in the middle of the bottom of the tank. This experiment was done by Koshizuka(1995). The number of fluid particles used in this simulation is 10658 with 0.002 m initial distance between particles. The gravitational force acts downwards with $g = 9.81 \text{ m/s}^2$. Density and viscosity are respectively equal to 1000 kg/m^3 and $10^{-6} \text{ m}^2/\text{sec}$.

3.4.3 Dam breaks on a wet bed

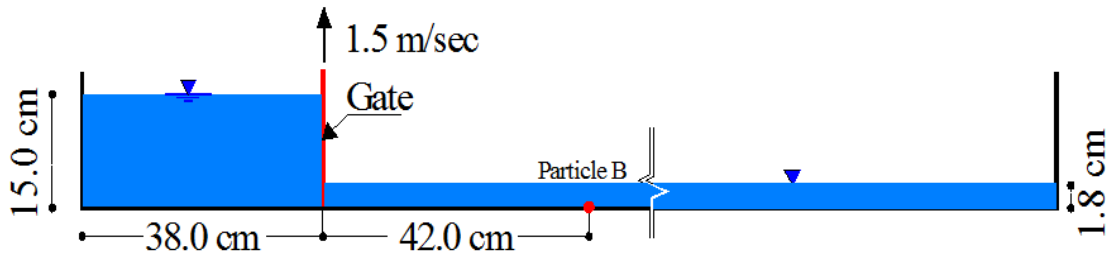


Fig 3.3 Experimental setup of the dam breaks on a wet bed, and the location of point (B)

This experiment was performed by Janosi et al. (2004). **Fig. 3.3** shows a schematic sketch of the experimental setup. Water column with depth equal 0.15 m and width equal 0.38 m is retained behind a gate; the initial downstream water depth is 0.018 m. In total 32250 fluid particles with an initial distance 0.002 m are used.

3.4.3.1 Results and analysis

Figs. 3.4-3.7 represents snapshots of the position of the particles, and free-surface shape at different times using the SPH method compared with the experimental results. A good agreement between simulated and experimental results is found when we used the suitable number of particles. Globally, the free surface profiles given by the SPH simulations are close to the experimental one, although the size of the entrapped bubble is underestimated in the SPH calculation. However, it has been remarked that by increasing the number of particles the size of the bubble is more and more accurate.




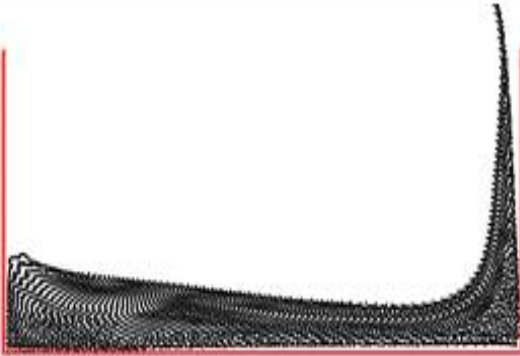
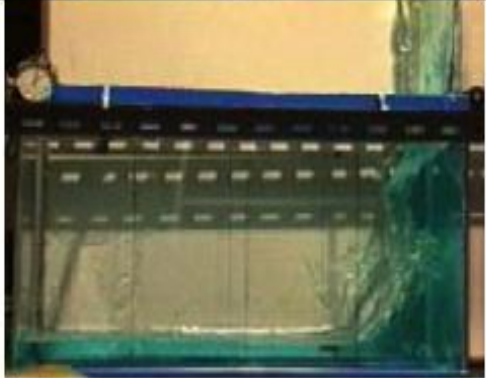
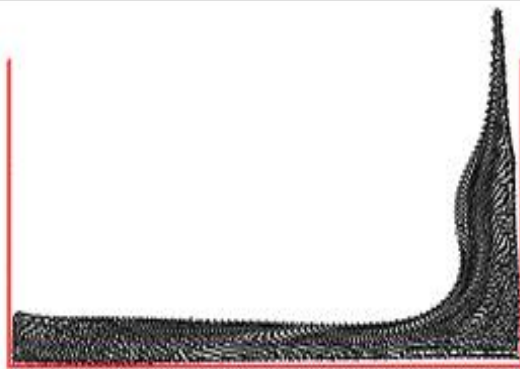

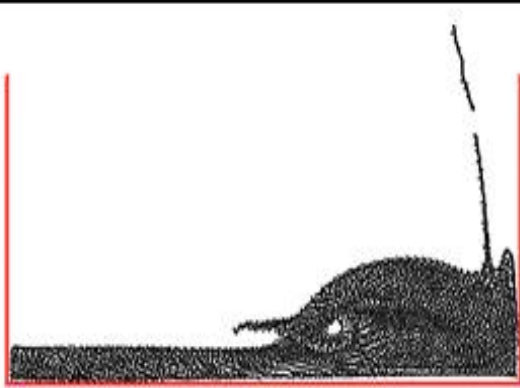
	Experimental (S. Koshizuka and Y. Oka) 2000	SPH
T=0.2 sec		
T=0.4 sec		
T=0.6 sec		
T=0.8 sec		

Fig 3.4 Comparison between experimental images and SPH simulation showing the position of the free surface at $t=0.2s$, $t=0.4s$, $t=0.6s$ and $t=0.8s$. (Dam break)

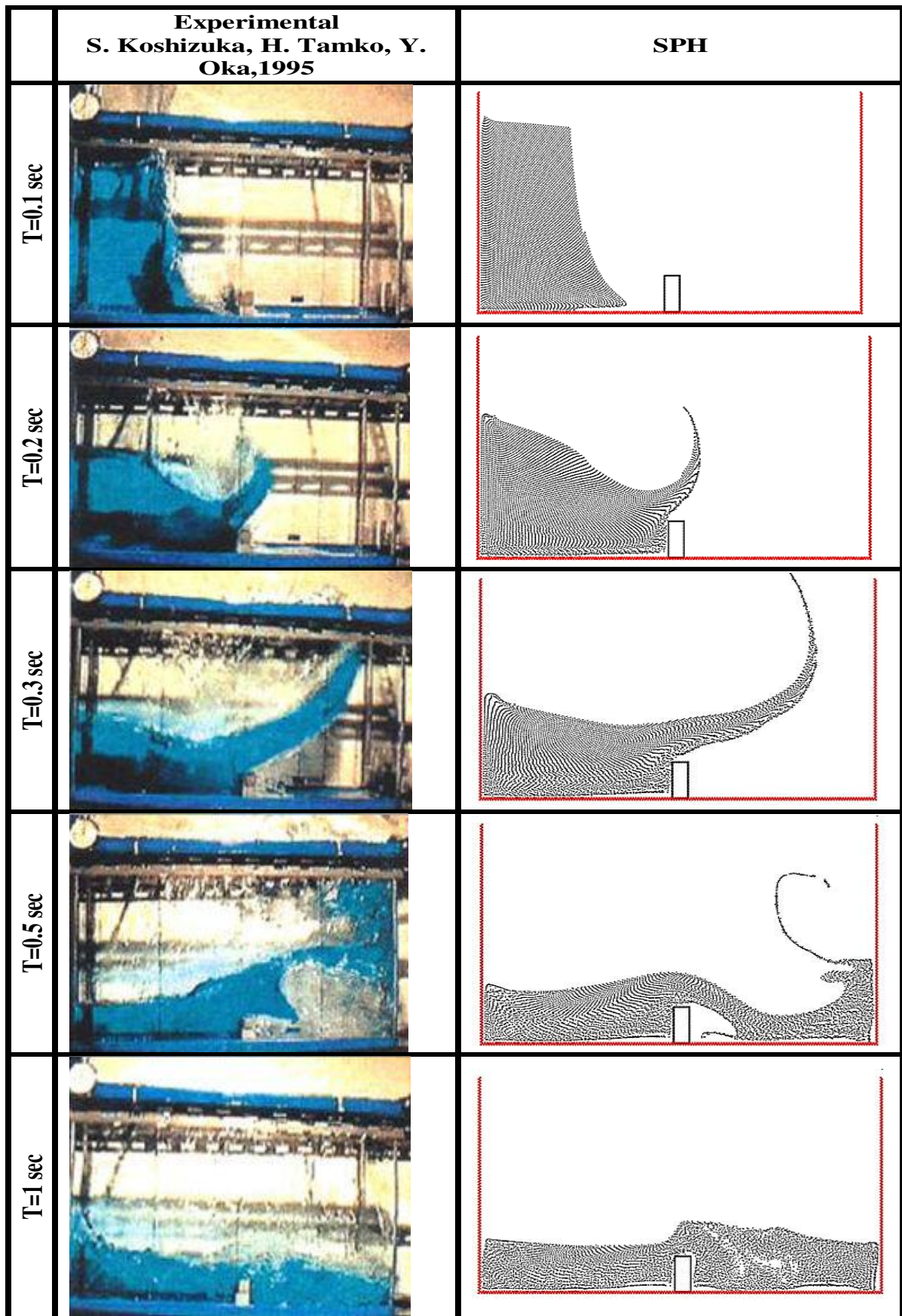


Fig 3.5 Comparison between experimental images and SPH simulation showing the position of the free surface at $t=0.1s$, $t=0.2s$, $t=0.3s$, $t=0.5s$, and $t=1.0s$

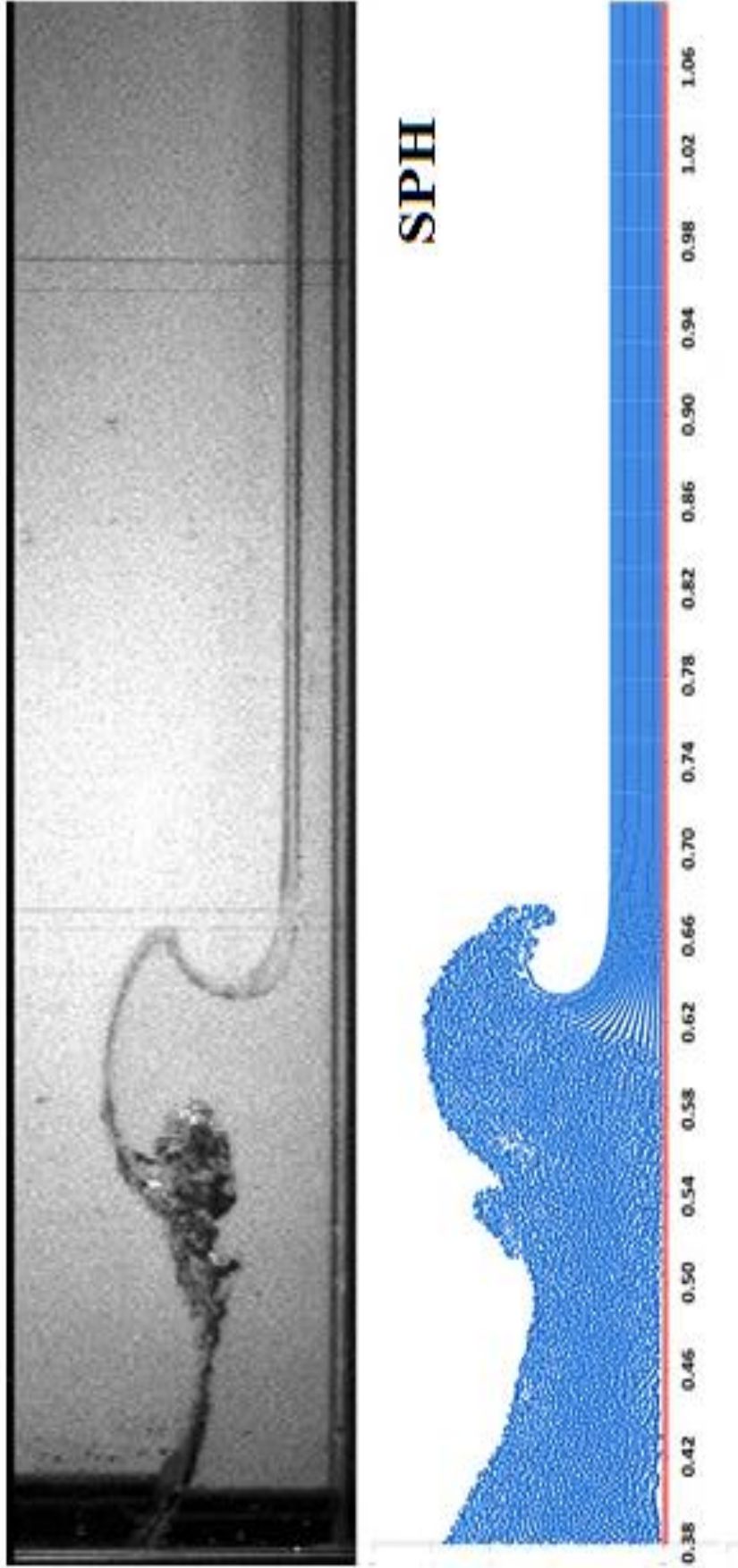


Fig 3.6 Snapshot of water particles at $t = 0.281$ Sec, numerical results (SPH) compared with experiment

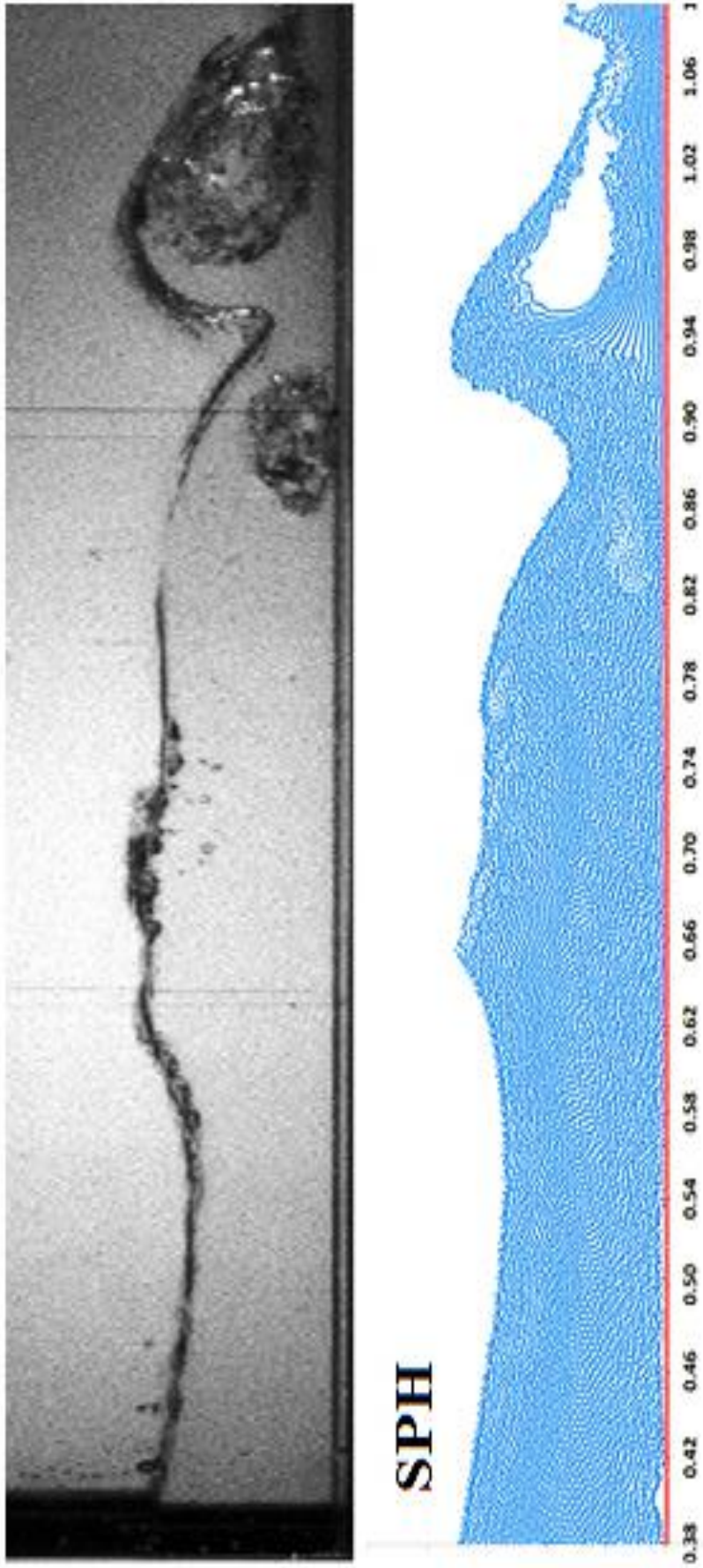


Fig 3.7 Snapshot of water particles at $t = 0.561$ sec, numerical results (SPH) compared with experimente

3.5 COMPARISON BETWEEN SPH AND MPS METHODS FOR NUMERICAL SIMULATIONS OF FREE SURFACE FLOW PROBLEMS

In this section a comparison between smoothed Particle Hydrodynamic (SPH) and the original version of Moving Particle Semi-implicit (MPS) methods in simulations of free surface flow problems were done. Numerical simulations for two cases (a collapse of a water column with a rigid obstacle, and dam break on a wet bed), using the both methods are compared with experimental data in order to know which method is appropriate and more efficient.

3.5.1 MPS model for water

If the particles are moving with a velocity equal v , and density equal ρ , the continuity and momentum equations for incompressible flow are:

$$\frac{D\rho}{Dt} = 0 \quad (3.13)$$

$$\frac{Dv}{Dt} = -\frac{1}{\rho} \frac{\partial p}{\partial x_i} + \nu \nabla^2 v + g \quad (3.14)$$

where ν is the kinematic viscosity; and g is the acceleration of the body force. In MPS method, the governing equations are transformed to particles interactions equations, which describe the particles interact with its neighbors covered with a weight function $w(r, r_e)$, where r is the distance between two particles, r_e the radius of the interaction area. There are many types of weight (kernel) function, and the commonly used one for viscid, incompressible flow is proposed by Koshizuka et.al (1996),

$$w(r) = \begin{cases} \frac{r_e}{r}, & r < r_e \\ 0, & r \geq r_e \end{cases} \quad (3.15)$$

The particle number density for particle i , is defined using the kernel function as:

$$\langle n \rangle_k = \sum_{j \neq i} w(|r_j - r_i|) \quad (3.16)$$

Based on the interpolation theory the gradient model and Laplacian model are expressed as follows (Gotoh and Sakai 2006),

$$\langle \nabla P \rangle_i = \frac{d}{n^o} \sum_{j \neq i} \left[\frac{P_j - P_i}{|r_j - r_i|^2} (r_j - r_i) w(|r_j - r_i|) \right] \quad (3.17)$$

$$\langle \nabla^2 v \rangle_i = \frac{2d}{\lambda n^o} \sum_{j \neq i} [(v_j - v_i) w(|r_j - r_i|)] \quad (3.18)$$

where d is the number of space dimensions, in this study $d = 2$, n^o is the particle number density which is constant and obtained from the initial conditions; λ is a coefficient introduced here so that the variance increase is equal to the analytical solution and given as:

$$\lambda = \frac{\sum_{j \neq i} [w(|r_j - r_i|) |r_j - r_i|^2]}{\sum_{j \neq i} [w(|r_j - r_i|)]} \quad (3.19)$$

3.5.2 Boundary conditions

In SPH method, we use a dynamic boundary condition to represent the boundary particles, which are forced to follow the governing equations (continuity, momentum and state equations), but they are fixed. When the fluid particles are close to the boundary, the density of the boundary particles increase according the continuity equation which leads to increase in the pressure following the equation of state. Therefore the force exerted on the incoming fluid particles increases due to the pressure term in the momentum equation by generation of repulsion between the fluid and boundary particles (Dalrymple 2001). While in MPS method we used the same type of boundary conditions in the original MPS method (Koshizuka 1998). The solid wall (boundary) is represented with three layers of fixed particles. Velocities are always zero in those three layers and pressure is calculated on the first inner layer only to repulse the fluid particles from the wall. The outer two layers are represented to keep the particle number density n^o , at the vicinity of the walls.

3.5.3 Difference in calculation

The differences between SPH and MPS methods can be summarized in the following points:

- 1- SPH is an explicit method, deals with water as an artificial fluid which is more compressible than the real one, and the pressure is calculated based on the equation of state, while MPS is an implicit method that deals with incompressible fluids, and the pressure is calculated from the Poisson equation.
- 2- The gradient of a function in SPH method is calculated using the gradient of smoothing function, $(\partial W_{ij}/\partial x_i)$, but in MPS method, the gradient of a function is calculated using algebraic operators with the weight function, $w(|r_j - r_i|)$ not using its gradient.
- 3- MPS has independence of parameters that usually require appropriate tuning, e.g. coefficients of artificial viscosity and XSPH scheme in the SPH method which in the practical viewpoint gives MPS superiority.
- 4- The comparison in this study is limited and it has under certain conditions. **Table 3.1** shows the terms used in each method.

Table 3.1 Differences in the used methods

	SPH	MPS
Numerical Stabilizer	Exist (Artificial Viscosity)	Not Exist
Velocity smoothing	Exist (XSPH)	Not Exist
Type of B.C	Dynamic B.C	Original MPS B.C

Two benchmark tests have been considered to assess the performance of the two numerical methods in simulation of free surface flows, to show the models capabilities and to stand on the difference between the two models. A collapse of a water column with a rigid obstacle (Koshizuka 1995), and dam break on wet bed (Janosi et al. 2004) are used.

3.5.4 Results and analysis

Figs. 3.8 and **3.9** present some snapshots of the position of the particles, and free-surface shape together with the pressure field (**Fig. 3.8**) and velocity field (**Fig. 3.9**) at different times using SPH and MPS methods compared with the experimental results. It is clear that the two methods can qualitatively simulate the free surface problems and capture the water free surface shape when we use a suitable number of particles. However the particle distributions in MPS method is more scattered than SPH method. The causes of these differences are that the particles in SPH method move using the XSPH variant (Monaghan, 1989), which makes its movement more smooth, however, one must be careful when choosing XSPH parameters because it can give inaccurate results in some cases like sharp velocity gradients (James 1999).

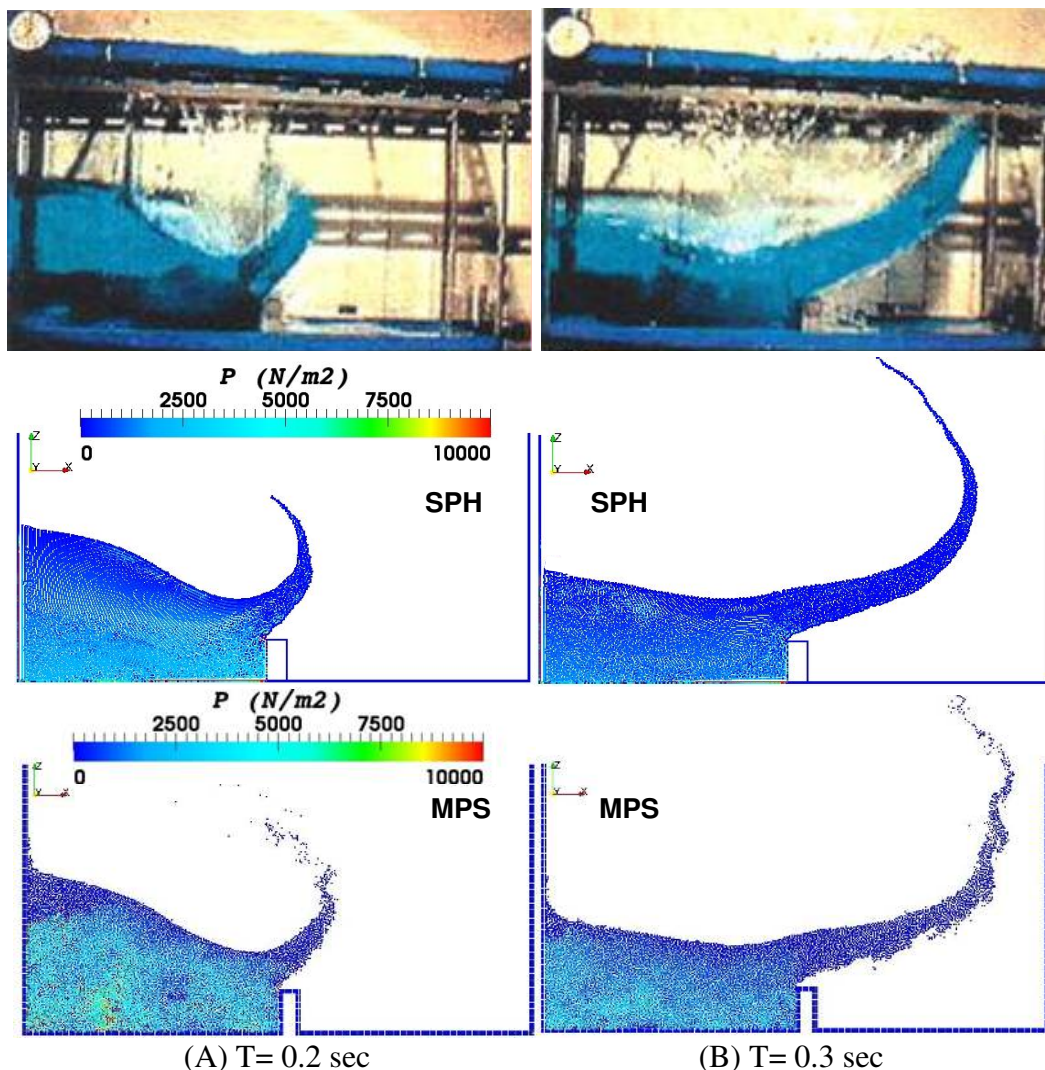


Fig 3.8 Snapshots of water particles together with the pressure field at (A) $t = 0.2$ sec, (B) $t = 0.3$ sec, numerical results (SPH & MPS) compared with experimental – case 1

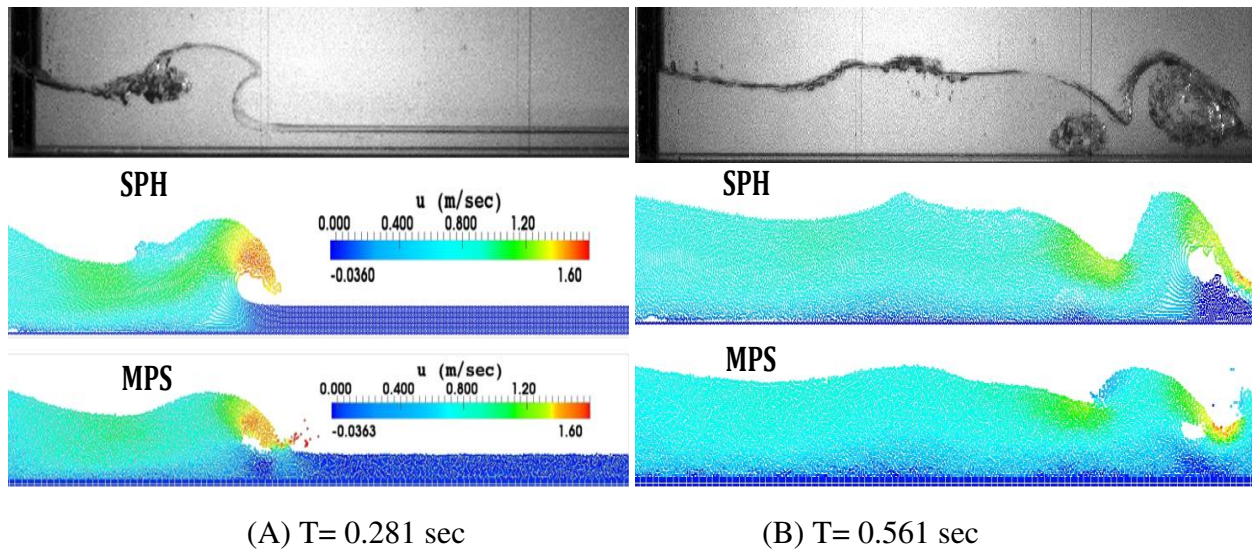


Fig 3.9 Snapshots of water particles together with the velocity field at (A) $t = 0.281$ and (B) $t = 0.561$ sec, numerical results (SPH &MPS) compared with experimental – case2.

In other hand, at MPS method when $r = 0$, the weight function, $w(r)$ will equal infinity. As a result of this, when two adjacent particles are close to each other, a rapid increase in the particle number density, $(n)_k$ happens and leads to increase in the pressure, and thus repulsion between particles occurs. Another important reason which gives scattered particles in MPS method is the numerical oscillation of pressure with high frequencies, which came from the source term of the Poisson equation. **Fig. 3.10** shows the values of pressure at wall particle (A) in case 1 and particle (B) in case 2. It is clear that the pressure from MPS method oscillates with severe fluctuation compared with SPH. Of course more accurate and stabilized simulation and less fluctuating pressure field would be obtained if we use the new improvements recently happened to the MPS method which include: introducing of a higher order source term in the Poisson equation (Khayer and Gotoh; 2011) or considering a slight level of compressibility (Shakibaeinia 2009), etc., and we will consider that in the future studies.

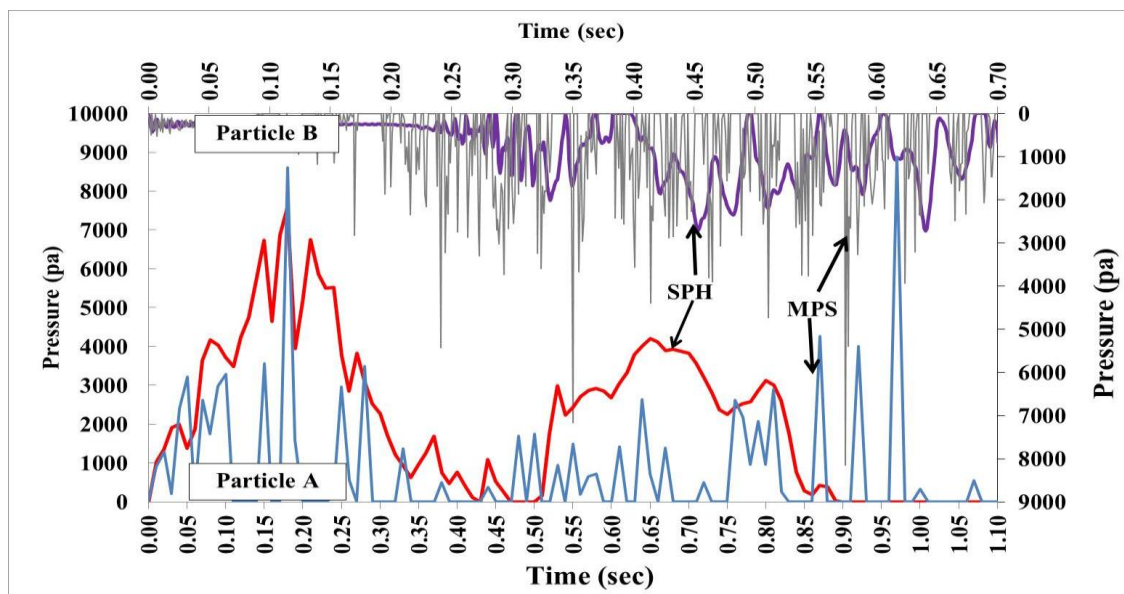


Fig.3.10 Temporal variations of pressure at particles (A) and (B)

3.5.4.1 Effect of the initial particles spacing

In order to investigate the convergence in this study and to know the effect of the initial particle spacing on the numerical results, three different initial particles spacing were selected in each case which are 0.008 m, 0.004 m, and 0.002 m. From figures 3.10 and 3.11, it is obvious that increasing the particles spacing decreases the number of fluid particles involving in the simulations, which leads to an inaccurate simulation and inconsistent shape of the free surface with the experimental results. Also in SPH method, if we use a suitable number of particles; not dense nor coarse; It gives comparatively smooth results and consistent free surface shape, unlike MPS method needs dense particles to capture the details of flow, but still the problem of scattered particles in MPS exists.

Also, we can notice from **Figs. 3.11** and **3.12** in the SPH results, as the distance between particles increases the particles move away from the boundaries noticeably. Might be the reason is using the dynamic boundary condition type.

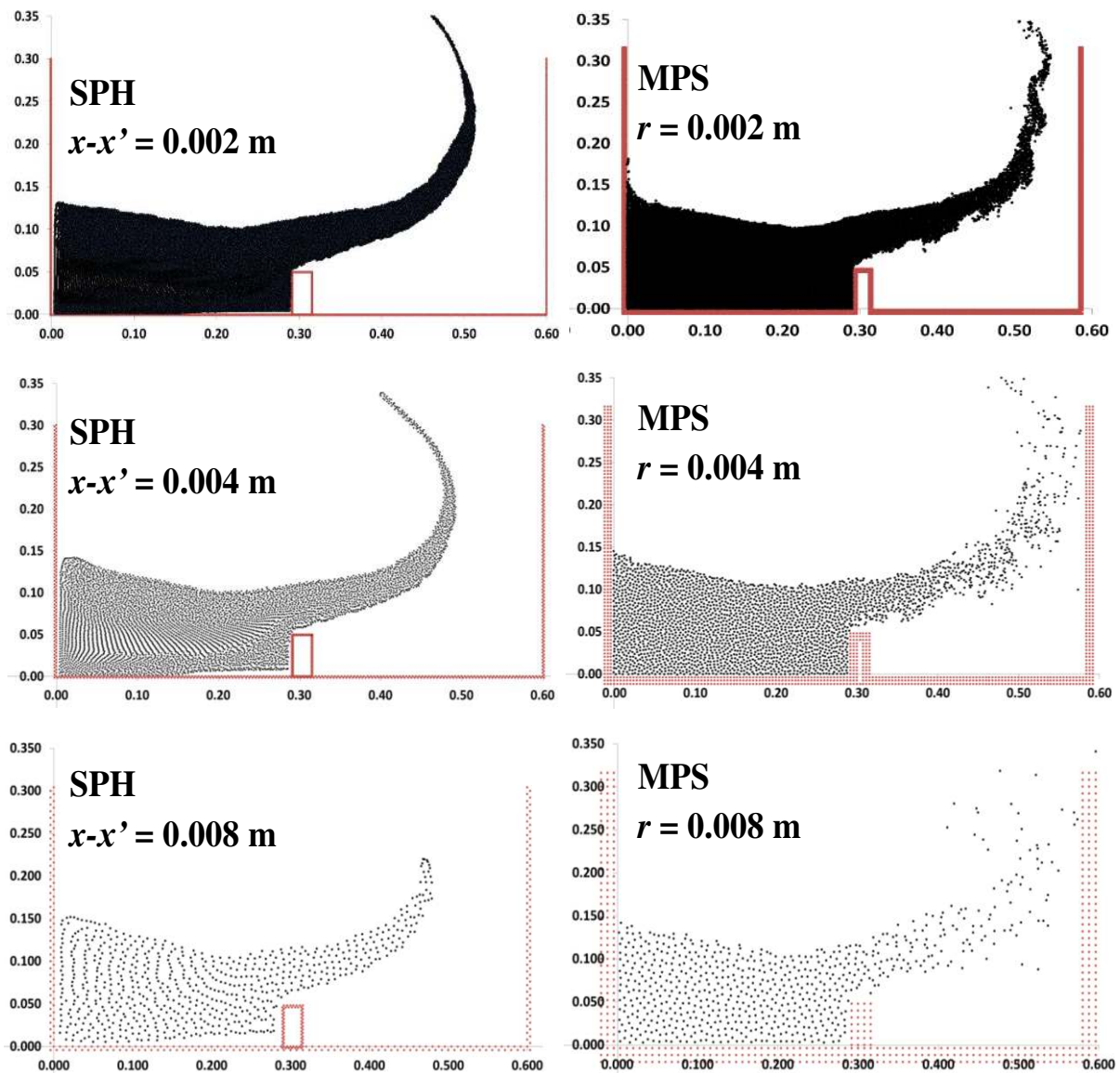


Fig 3.11 Particles positions and free surface shape using various initial particle spacing at $t=0.3$ sec (case1).

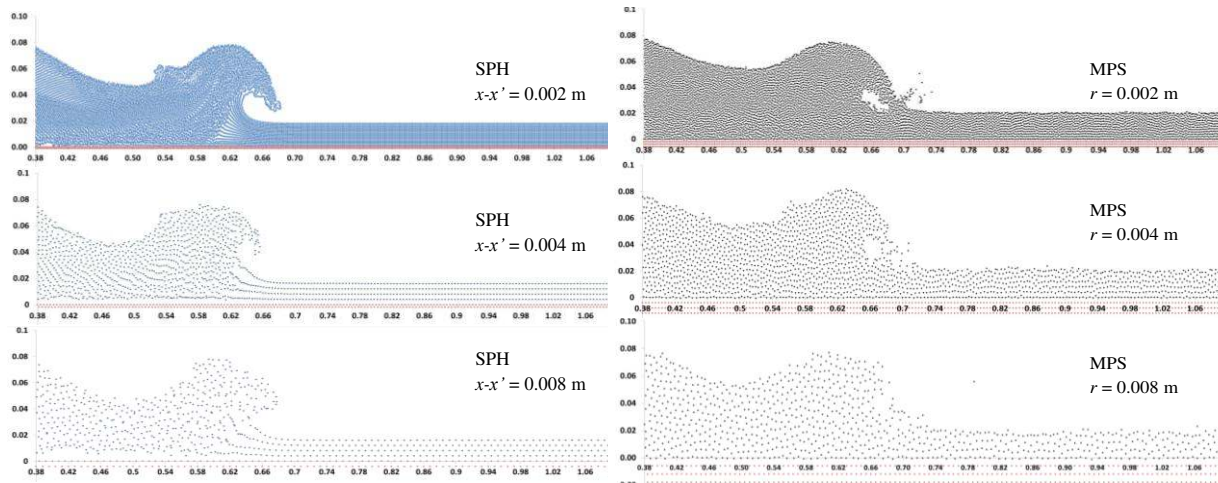


Fig 3.12 Particles positions and free surface shape using various initial particle spacing at $t = 0.281$ sec.

3.5.4.2 Computational efficiency

In order to know which method is more efficient, we have to consider the simulation time elapsed for each case. **Table 3.2** shows the elapsed time to simulate the first and last steps in the calculation of case 2, (from 0.00 to 0.001 and from 0.699 to 0.700).

It is clear that the difference between the two elapsed times in MPS method are bigger than the difference in SPH method, because in MPS method the pressure calculation using Poisson equation takes time at the beginning of the simulation, but after the wave breaks the pressure calculations time is reduced. In case of using 0.002 m spacing between fluid particles, the first step calculation is 2.33 times larger than the last step in MPS, while in SPH almost no difference, leading to increase the total computation time in MPS method.

Table 3.3 shows the total time elapsed in hour to simulate case 2 to reach 1.1 sec, and case 2 to reach 0.7 sec. We can notice that the total computational time using the SPH method is 1.98 times smaller than MPS method in the first case and 5.41 times in the second case when we used 0.004 m spacing between fluid particles. These differences become 4.37 times smaller in case 1 and 3.22 times in case 2 using 0.002 m spacing between fluid particles.

Table 3.2 First and last CPU time step (sec.) – case 3

	SPH method			MPS method		
	Distance between Particles (m)			Distance between Particles (m)		
	0.008	0.004	0.002	0.008	0.004	0.002
1st CPU time step	0.359	2.262	19.81	2.663	7.119	27.387
Last CPU time step	0.218	1.929	19.80	0.499	3.039	11.721

Table 3.3 Total time elapsed (hr.)

	Method	Distance between Particles		
		0.008 m	0.004 m	0.002 m
Case 2	SPH	0.112	0.794	6.069
	MPS	0.139	1.572	26.526
Case 3	SPH	0.068	0.488	6.819
	MPS	0.250	2.640	21.996

3.6 SUMMARY

The chapter presents a comparative study between SPH and the standard MPS methods which are mesh free, lagrangian, particle methods. The numerical results for a collapse of water column with a rigid obstacle and a dam break on wet bed were compared with the experimental results. The results showed that the two methods can deal with problems with large deformations of the water free surface. The particles distribution from the SPH method is more stable than MPS method, due to using the artificial viscosity, and the predicted free surface from SPH calculation is smoother than the free surface from MPS calculation which gives noisy and splashing free surface. An advantage of SPH method is that even if rather a coarse particles arrangement, it yields relatively smooth results and reduces the computation time. One of the features of using MPS method, it has independence upon parameters that usually require appropriate tuning unlike the SPH method. We only consider MPS method in original form. Recently, many studies have been done to improve MPS, in particular, correcting unreasonable pressure oscillations. In the next step, we want to consider such refined MPS methods to clarify such refinement effects and their advantages compared with SPH, also using other types of boundary conditions like repulsive boundary condition with the SPH method to stand on which type is better, and taking into consideration one of the important aspects which is compared in terms of 'volume conservation'.

Chapter 4

Numerical simulation of snow avalanche as a Bingham Fluid Flow using non-Newtonian 3D-SPH model

In many regions like Hokkaido prefecture in Japan, increasing the amount of snowfall in the winter, beside adverse weather conditions cause snow avalanches. Snow avalanches cause damage in infrastructures, property and lose of human life (i.e. the avalanche disaster in Niigata prefecture, 1918). Hence, it is in a major importance to establish effective prediction methods for analyzing the snow avalanche and flow behavior. Then the damage, yielding from avalanches may be reduced by constructing effective energy dissipation structures. Establishing field measurements for snow avalanches may be very dangerous; therefore prediction of the avalanche path and its runoff distance is a difficult task.

4.1. INTRODUCTION

Numerical methods are considered as a useful tool to predict the behavior of snow avalanches, and to provide avalanche hazard maps and assess the risk on infrastructure.

The mesh-based numerical methods, such as finite difference, finite volume and finite element methods, have been widely employed to solve the flow regime. Despite of their great success, they are limited to problems with small deformations and simple geometries. Moreover, one of the greatest deficiencies of these methods is the low-resolution discretization of the advection term which causes numerical diffusion (Gotoh et.al, 2013).

In this chapter, a 3D smoothed particle hydrodynamics method was applied the snow avalanches and predict the avalanche path and the run off distance. The snow was considered as a Bingham fluid and the snow viscosity was calculated based on the Bingham constitutive model, on the basis of Coulomb's failure criterion. An equivalent Newtonian viscosity is calculated to express the Bingham viscosity into Navier-Stokes equations. A simple and small scale snow avalanche experiment with different types of obstacles was simulated using the SPH method. Numerical results showed that, in the most cases, good agreements were found by the means of leading edge position and travel length.

4.2. GOVERNING EQUATIONS

The motions of snow in the framework of SPH can be described via the following continuity and momentum conservation equations:

$$\frac{D\rho}{Dt} = -\rho \frac{\partial v^\alpha}{\partial x^\alpha} \quad (4.1)$$

$$\frac{Dv^\alpha}{Dt} = \frac{1}{\rho} \left(\frac{\partial \sigma^{\alpha\beta}}{\partial x^\beta} \right) + f^\alpha \quad (4.2)$$

where α and β denote the Cartesian components x , y and z with the Einstein convention applied to repeated indices; ρ is the density; v is the velocity; $\sigma^{\alpha\beta}$ is the total stress tensor, f^α the gravity force; and D/Dt is the total derivative as follows,

$$\frac{D}{Dt} = \frac{\partial}{\partial t} + v^\alpha \frac{\partial}{\partial x^\alpha} \quad (4.3)$$

The stress tensor, $\sigma^{\alpha\beta}$ consists of two parts: anisotropic pressure, P , and viscous shear stress, $\tau^{\alpha\beta}$, as follows:

$$\sigma^{\alpha\beta} = p^{\alpha\beta} + \tau^{\alpha\beta} \quad (4.4)$$

where $p^{\alpha\beta} = -P\delta^{\alpha\beta}$.

The viscous shear stress is proportional to the shear strain through the viscosity in the case of the Newtonian fluids, but when dealing with non-Newtonian fluid, the relation between shear stress and the shear strain rate is given by the following relation:

$$\begin{cases} \tau^{\alpha\beta} = \mu \dot{\gamma} + \tau_{min} & \tau^{\alpha\beta} > \tau_{min} \\ \dot{\gamma} = 0 & \tau^{\alpha\beta} < \tau_{min} \end{cases} \quad (4.5)$$

where τ_{min} is the yield strength; and $\dot{\gamma}$ is the shear strain rate, which can be calculated from the following equation,

$$\dot{\gamma} = \sqrt{\frac{1}{2} \dot{e}^{\alpha\beta} \dot{e}^{\alpha\beta}} \quad (4.6)$$

where $\dot{e}^{\alpha\beta}$ is the second invariant of the deviatoric strain rate tensor. The shear strain rate $\dot{\gamma}$ is simplified in 3-D, as follows:

$$\dot{\gamma} = \sqrt{2 \left[\left(\frac{\partial u}{\partial x} \right)^2 + \left(\frac{\partial v}{\partial y} \right)^2 + \left(\frac{\partial w}{\partial z} \right)^2 \right] + \left(\frac{\partial u}{\partial y} + \frac{\partial v}{\partial x} \right)^2 + \left(\frac{\partial u}{\partial z} + \frac{\partial w}{\partial x} \right)^2 + \left(\frac{\partial v}{\partial z} + \frac{\partial w}{\partial y} \right)^2} \quad (4.7)$$

Equation number (4.5) is well known as a Bingham model or Bingham equation. From the characteristics of the Bingham fluid, it acts as a rigid body and does not deform when the value of the shear stress is less than the yield stress, but in case the shear stress is greater than the yield stress, flow failure occurs, leading to very large deformations. Therefore, in order to formulate the constitutive model for snow avalanches, the Bingham model is combined with the following Mohr-Coulomb equation:

$$s = c + \sigma_n \tan \phi \quad (4.8)$$

where s , c , σ_n and ϕ are the shear strength, the cohesion, the normal stress and the angle of repose, respectively. This was by substituting the shear strength and the normal stress with the

yield strength and the pressure, respectively, and then the following Bingham model is proposed:

$$\tau^{\alpha\beta} = \mu \dot{\gamma} + c + P \tan \phi \quad (4.9)$$

This model is simple and only required two parameters c and ϕ , which can be easily obtained from the previous studies, e.g. Matsuzawa et al., 2007.

In order to express the Bingham viscosity in the momentum equation, an equivalent Newtonian viscosity is calculated by dividing the equation (4.9) by the shear strain rate and defining the equivalent viscosity by μ ,

$$\dot{\mu} = \mu + \frac{c+P \tan \phi}{\dot{\gamma}} \quad (4.10)$$

To overcome the numerical difficulties corresponding to the discontinuity in the constitutive relations, when the yield point is approached, and to prevent the viscosity diversion due to the appearance of the shear rate in the denominator. The regularized model proposed by (Papanastasiou 1986) is used, which is continuous and applicable on both the yielded and the un-yielded regions. In this case the regularized Bingham model can be written as:

$$\dot{\mu} = \mu + \frac{c + P \tan \phi}{\dot{\gamma}} (1 - e^{-m\dot{\gamma}}) \quad (4.11)$$

where m is the stress growth exponent, a parameter related to the transition between the solid and fluid regimes. A value of 1000 (s) was used for m in the present study (Otsuka et.al, 2009).

4.3. SPH FORMULATION

Using the above SPH approximation, which discussed and summarized in chapter two, the system of partial differential equations (4.1) and (4.2), can be converted into the SPH formulations which will be used to solve the motion of snow particles as follows:

$$\frac{D\rho_i}{Dt} = \sum_{j=1}^N m_j (v_i^\alpha - v_j^\alpha) \frac{\partial W_{ij}}{\partial x_i^\alpha} \quad (4.12)$$

$$\frac{Dv_i^\alpha}{Dt} = \sum_{j=1}^N m_j \left(\frac{\sigma_i^{\alpha\beta}}{\rho_i^2} + \frac{\sigma_j^{\alpha\beta}}{\rho_j^2} \right) \frac{\partial W_{ij}}{\partial x_i^\beta} + f^\alpha \quad (4.13)$$

Also the derivatives appear in equations (4.7) can be converted to SPH formulations as follow:

$$\frac{\partial u_i}{\partial x} = \sum_{j=1}^N \frac{m_j}{\rho_j} (u_j - u_i) \frac{\partial W_{ij}}{\partial x} \quad (4.14)$$

$$\frac{\partial v_i}{\partial y} = \sum_{j=1}^N \frac{m_j}{\rho_j} (v_j - v_i) \frac{\partial W_{ij}}{\partial y} \quad (4.15)$$

$$\frac{\partial w_i}{\partial z} = \sum_{j=1}^N \frac{m_j}{\rho_j} (w_j - w_i) \frac{\partial W_{ij}}{\partial z} \quad (4.16)$$

The other derivatives can be calculated in the same manner. In order to solve Navier–Stokes equations, “equation of state” is used to estimate the pressure change. Following Monaghan & Kocharyan (1995), the pressure can be calculated using the equation of Tait:

$$P = B \left[\left(\frac{\rho}{\rho_o} \right)^\lambda - 1 \right] \quad (4.17)$$

where λ is constant and equal 7, ρ_o is the reference density, B is problem dependent parameter, which sets a limit for the maximum change of the density and will be calculated as

$$B = \frac{100 V_{type}^2 \rho_o}{\lambda}, \quad V_{type} = \sqrt{2 g H} \quad (4.18)$$

where V_{type} is the typical speed of snow; and H is the depth of the snow at the beginning of the calculation which is constant and is equals 0.3 m.

In order to damp out the unphysical stress fluctuation and to prevent shock waves and the penetration of sow particles through the boundaries, an artificial viscosity has been employed to the pressure term in the momentum equation. In this study, we used the most widely used one which is proposed by Monaghan & Lattanzio (1985). Finally the momentum equation after introducing the artificial viscosity becomes as follows:

$$\frac{Dv_i^\alpha}{Dt} = \sum_{j=1}^N m_j \left(\frac{p_i^{\alpha\beta}}{\rho_i^2} + \frac{p_j^{\alpha\beta}}{\rho_j^2} + \pi_{ij} \right) \frac{\partial W_{ij}}{\partial x_i^\beta} + \sum_{j=1}^N m_j \left(\frac{\tau_i^{\alpha\beta}}{\rho_i^2} + \frac{\tau_j^{\alpha\beta}}{\rho_j^2} \right) \frac{\partial W_{ij}}{\partial x_i^\beta} + f^\alpha \quad (4.19)$$

4.4. TEST CASE

In order to investigate and to show the SPH model’s capabilities for simulating non-Newtonian fluids with free surfaces, a 2-D unsteady mud-flow released from a reservoir of finite size onto a steep channel is simulated.

The problem is one of 69 unsteady flow experiments made by (Komatina & Jovanovic 1997), with different initial reservoir depth, bed slope, and volume concentration of mixtures. One of these experiments has been selected, in which the initial mixture length 2.0 m and the initial height 0.1 m, channel bed slope 0.1% is considered, and the volume concentration of mixtures is 27.4% which is corresponding to the mud of density 1200 kg/m³. In total 51051 fluid particles with an initial distance 0.002 m is used. The mud-flow properties for the Bingham model as reported on the experiment are shown in **Table 4.1**.

Table 4.1 The mud-flow properties

Parameter	Value
Density (kg/m ³)	1200
Yield strength (Pa.)	25
Viscosity (Pa.s)	0.07

Fig. 4.1 presents some snapshots of the position of particles, and free-surface shape at different times. The simulated flow patterns are very similar to the mudflow profiles observed experimentally by (Komatina & Jovanovic, 1997).

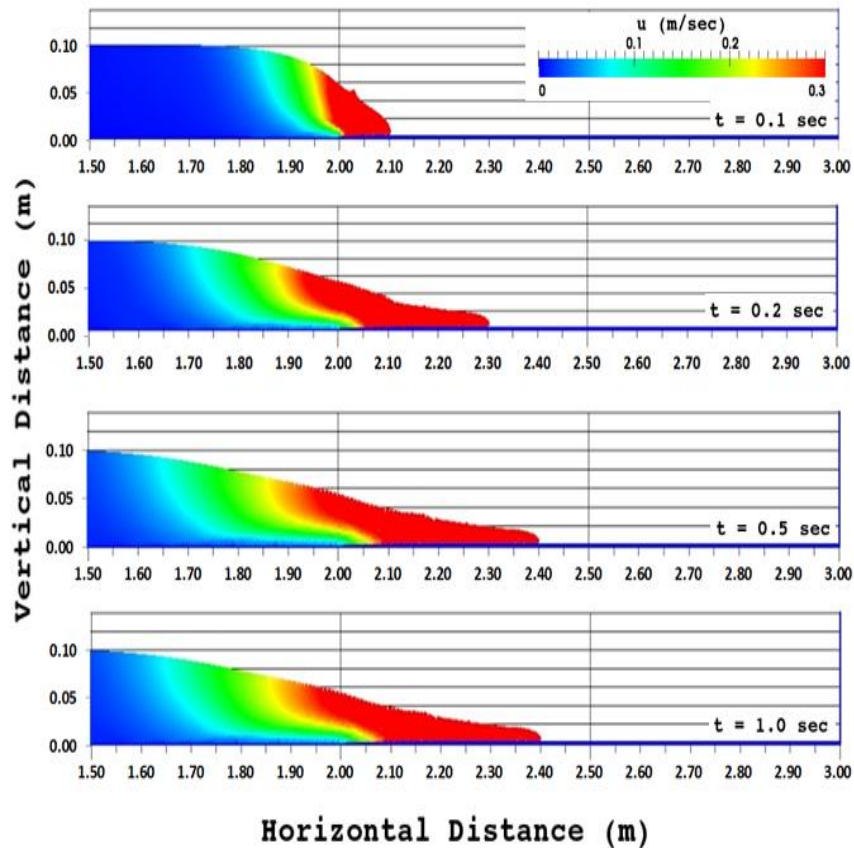


Fig 4.1 Particle distributions after collapse of dam at time $t = 0:1, 0.2, 0.5,$ and 1.0 s.

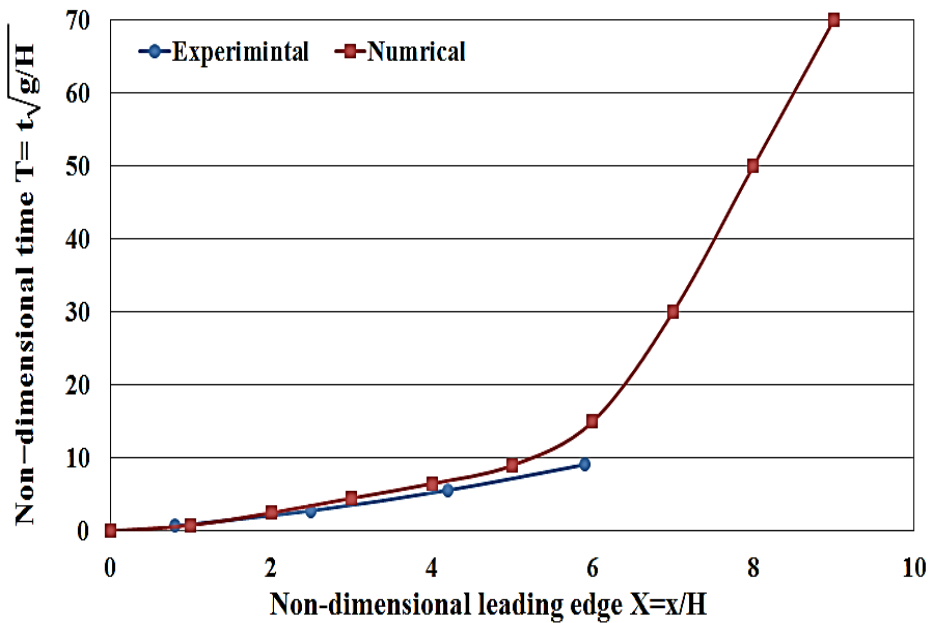


Fig 4.2 The relationship between the non-dimensional leading edge and time after a dam-break of water and mud-flow.

Fig. 4.2 shows the relation between the computed non-dimensional leading ledge of the mudflows $X = x/H$ starting from the dam site, where H is the initial height of the mudflow, with non-dimensional time for the mudflows compared with the experimental data. There is good agreement between SPH and the experimental results, indicating that this numerical method can be used for practical simulation of non-Newtonian fluid.

4.5. SNOW AVALANCHES MODEL TEST

The chances to observe real snow avalanche in nature is very low, therefore, data for nature avalanches are relatively not available.

Many snow avalanche experiments have been carried out using different materials, such as beads or foamed polystyrene (Hutter et al., 1995) instead of snow. However, most of these experiments were failed to reproduce the erosion and deposition process, especially in regions close to obstacles. In this study a simple snow avalanche experiment, held by Kato et al., (2011) on the open site using real snow, is replicated numerically using the proposed SPH model.

4.5.1. Model description

Fig. 4.3 shows the model slope. **Fig.4.4** is a schematic sketch showing the dimensions of the experiment and the initial position of the snow mass. The model was built using six wooden panels, each 1.80 m in width and 5.4 m in length, and an inclination of 45° . The connection between the horizontal panels and the inclined panels is smoothed out using real snow.



Fig 4.3 Model setup performed by Kato et al. (2012).

In order to determine the falling speed and position of snow leading edge, a red line with 20 cm intervals have been drawn in the slope as shown in **Fig.4.3**. The snow mass dimensions are (30 cm × 30 cm × 30 cm), which initially found in starting box above the end of the slope with a distance equal 0.55 m and fixed with experimental skeleton by two arms.

Four types of avalanche experiment with different shapes of obstacles in the bottom of the slope were conducted as shown in **Fig.4.5**:

- A. Slope only without obstacle.
- B. Stake rows with 2 cm spacing.
- C. Stake rows with 4 cm spacing.
- D. Obstacle with Notched Opening.

4.5.2. Numerical simulations

Simulation of snow avalanches model tests was carried out using the SPH model. The snow parameters could be found in many previous studies, e.g. Matsuzawa (2007), but these values have a wide range depending on many factors like type of snow, temperature, etc. In our study, we select these parameters by trial and error inside the known ranges to reach to the most accurate results compared with the experiment. **Table 4.2** shows the snow parameters used in the numerical simulation.

The number of snow particles used to simulate the snow mass was 29791, with 0.01 m initial distance between particles.

Table 4.2 Snow parameters used in the numerical simulation

Parameter	Value
Density (kg/m ³)	$\rho = 320$
Cohesion (Pa)	$C = 0.0$
Angle of repose	$\tan \phi = 0.87$

4.5.3. Results and analysis

Fig.4.6 presents an analysis of the falling stage, free-surface shape, and particle positions together with the velocity field at different times until the dormancy status using the SPH method, and it is compared with the experimental results for case 1. It is clear, from the obtained results, that the proposed model can qualitatively simulate the snow avalanche problems and capture the failure shape.

However, we have indicated differences between the experimental and numerical results in terms of the initial shape of the snow avalanche on the slope as well as the velocity of the avalanche at the beginning of the experiment. This is because of the differences in the initial release of the cubic snow in the experiment and in the simulation. In the simulation, the snow mass is assumed as powder materials, though it acted as a block at the time of the collision with the slope in the experiment. Therefore, the dynamics at the time of the collision are different between the experiment and the computation. But after 2.0 seconds of the experiment the avalanche state becomes very similar to that of numerical results, including the shape of the final deposition cone in the lower part of the slope as shown in **Fig.4.7**.

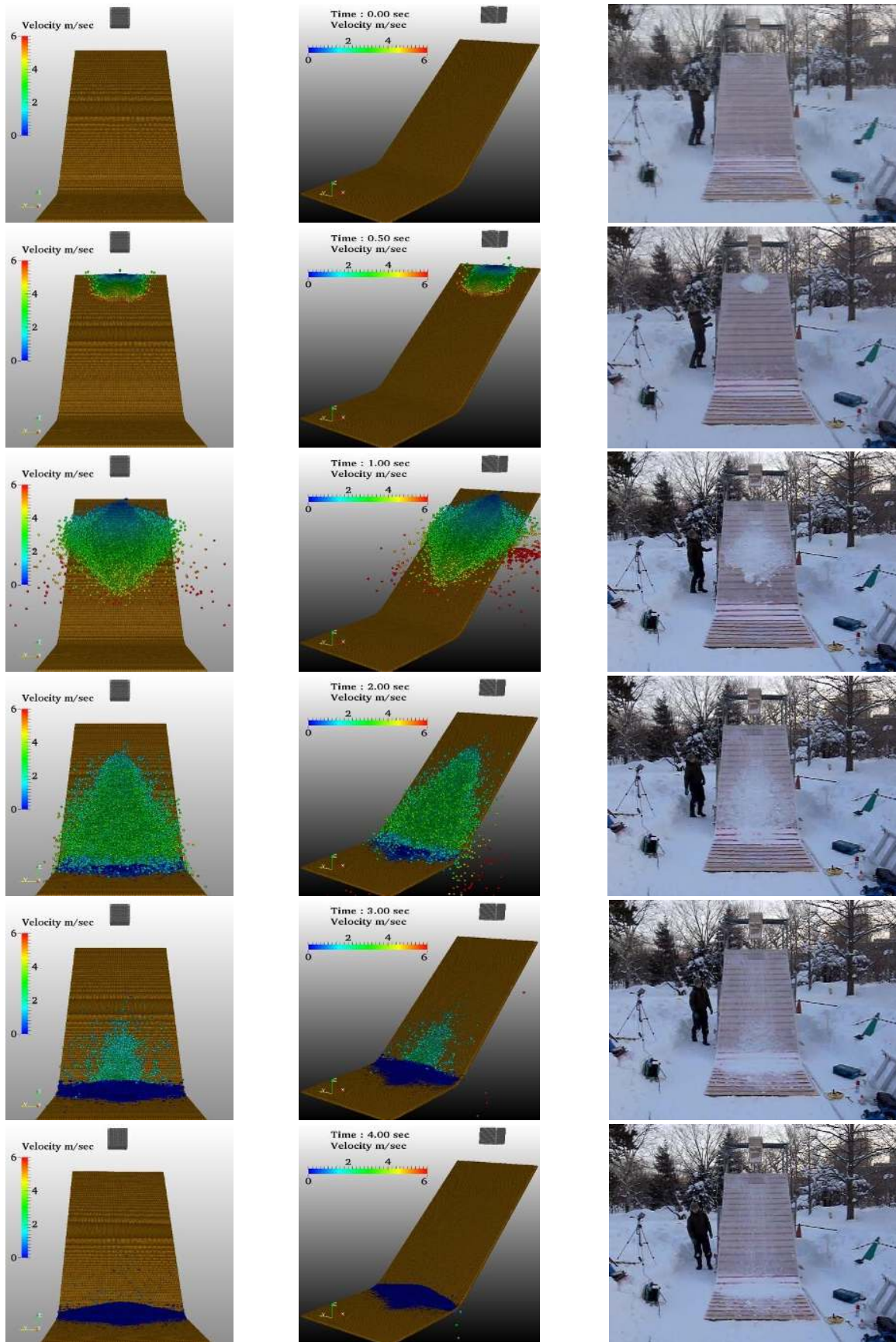


Fig 4.6 Comparison between computation and experiment results at different time steps ($t = 0, 0.5, 1, 2, 3,$ and 4 Sec)

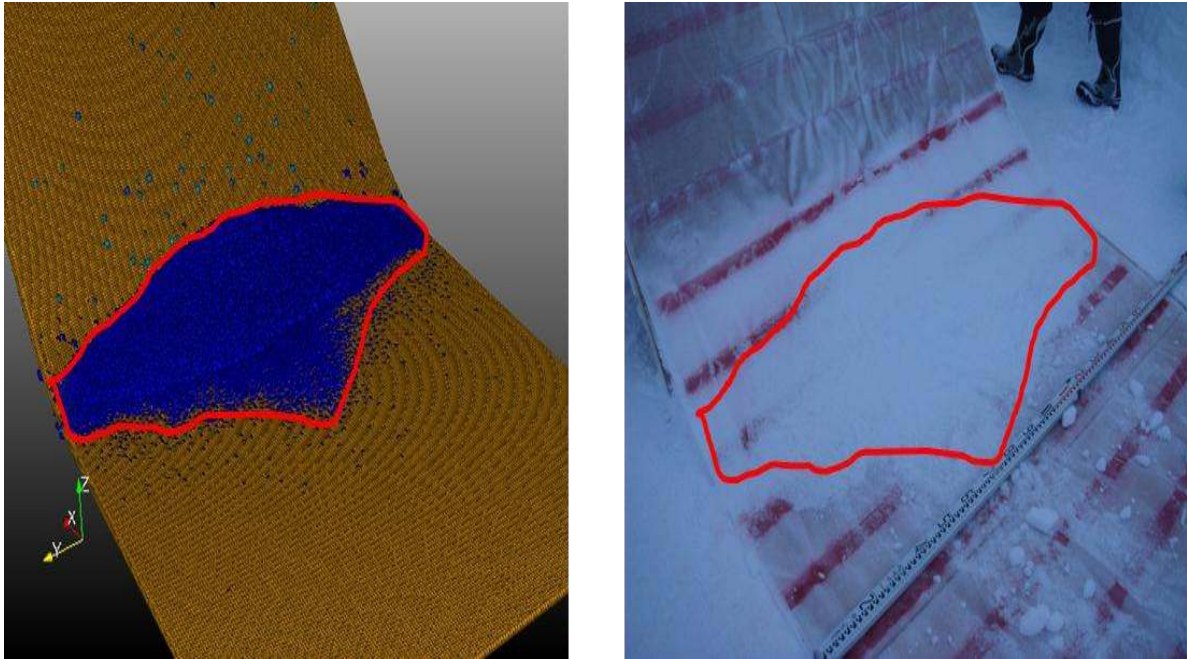


Fig 4.7 shape of the deposition cone in the lower part of the slope (case1)

Another difference in the term of particles spreading during the falling stage is probably due to the change in snow property in the simulation than the real case.

We also noticed some particles were fallen down from the slope sides in the simulated results, which was successfully confirmed by the experimental results.

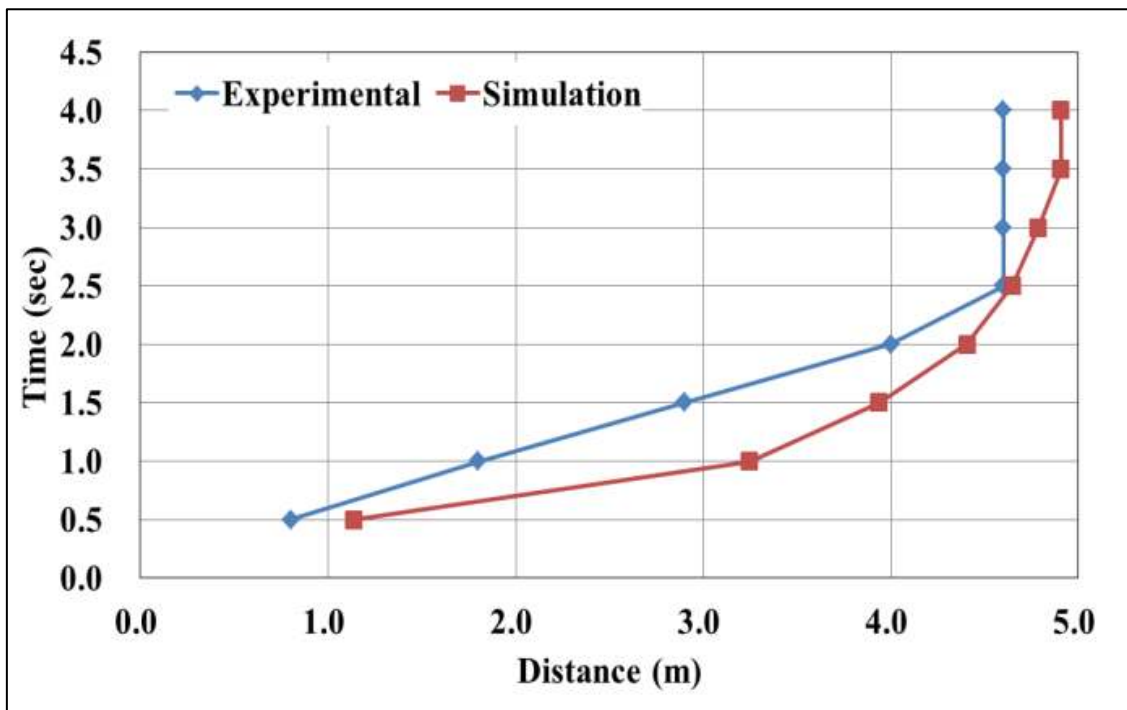


Fig 4.8 Comparison between experimental and numerical results in term of the position of snow leading edge with time (case 1)

Fig.4.8 represents a comparison between experimental and numerical results in term of the position of snow leading edge with time. There are small differences between SPH and the experimental results. It took about 2.5 seconds until the snow stopped in the experiment, whereas in the simulation, this time was more than 2.5 seconds. It is also noticed that the particles in the simulation move faster than the natural snow.

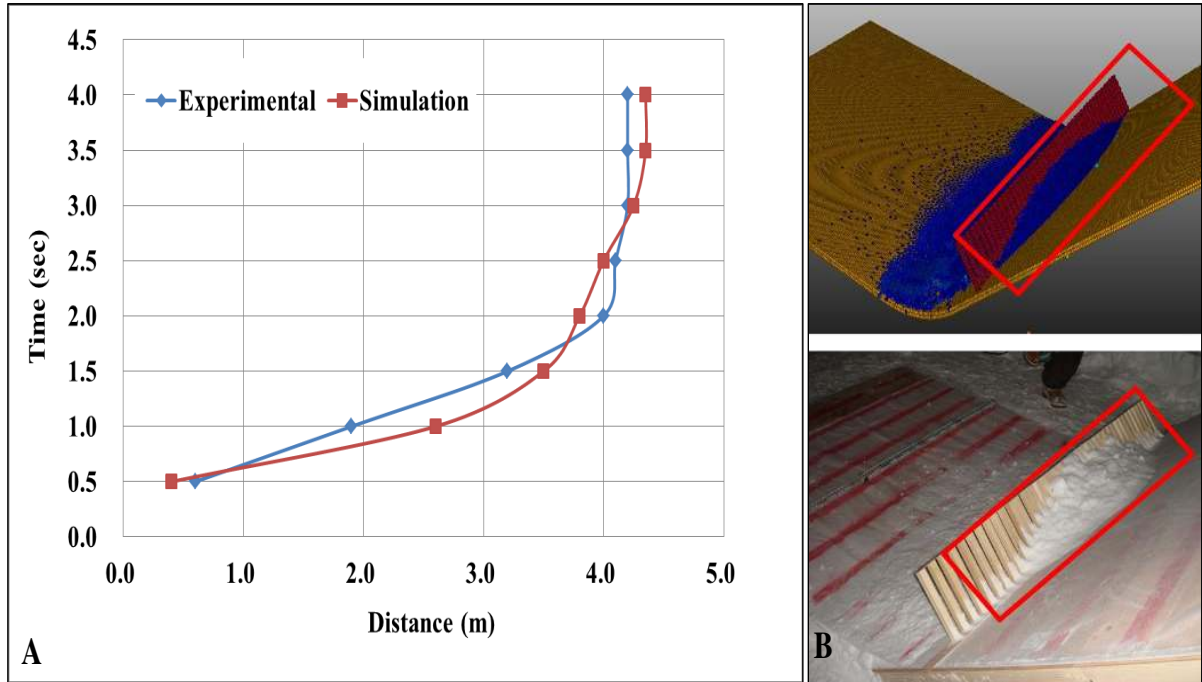


Fig 4.9 Case of Stake rows with 2 cm spacing: (A) Avalanche propagation, (B) Deposition shape in the simulation and the experiment at $t= 4$ Sec

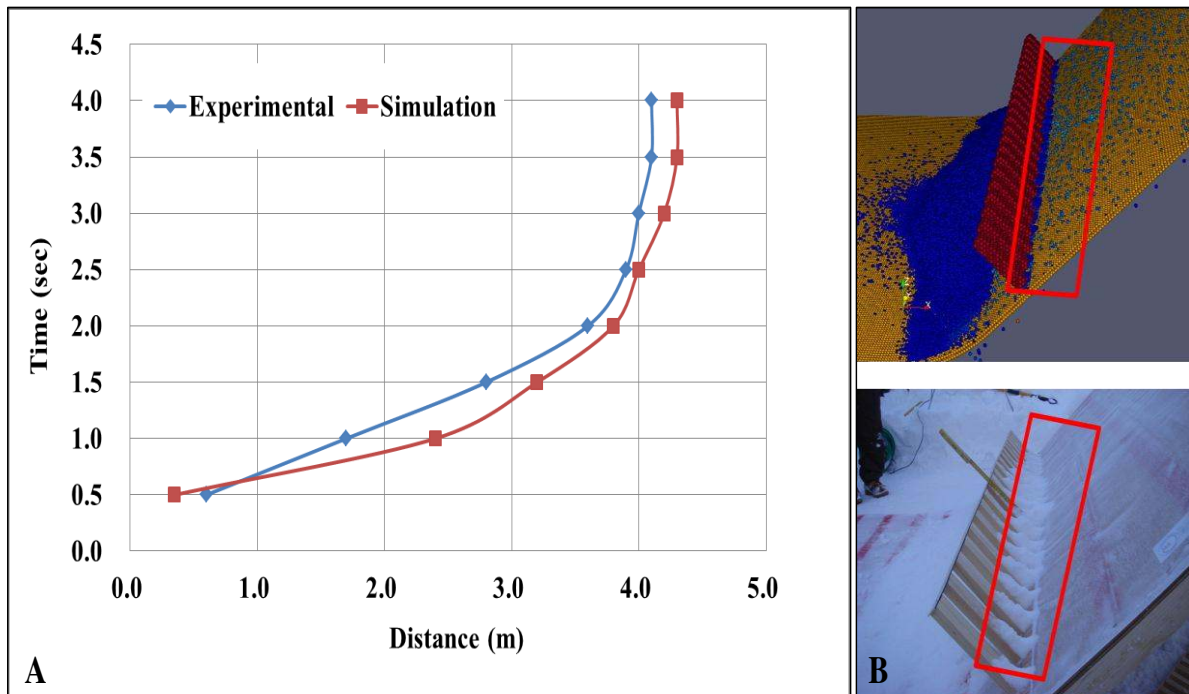


Fig 4.10 Case of Stake rows with 4 cm spacing: (A) Avalanche propagation, (B) Deposition shape in the simulation and the experiment at $t= 4$ Sec

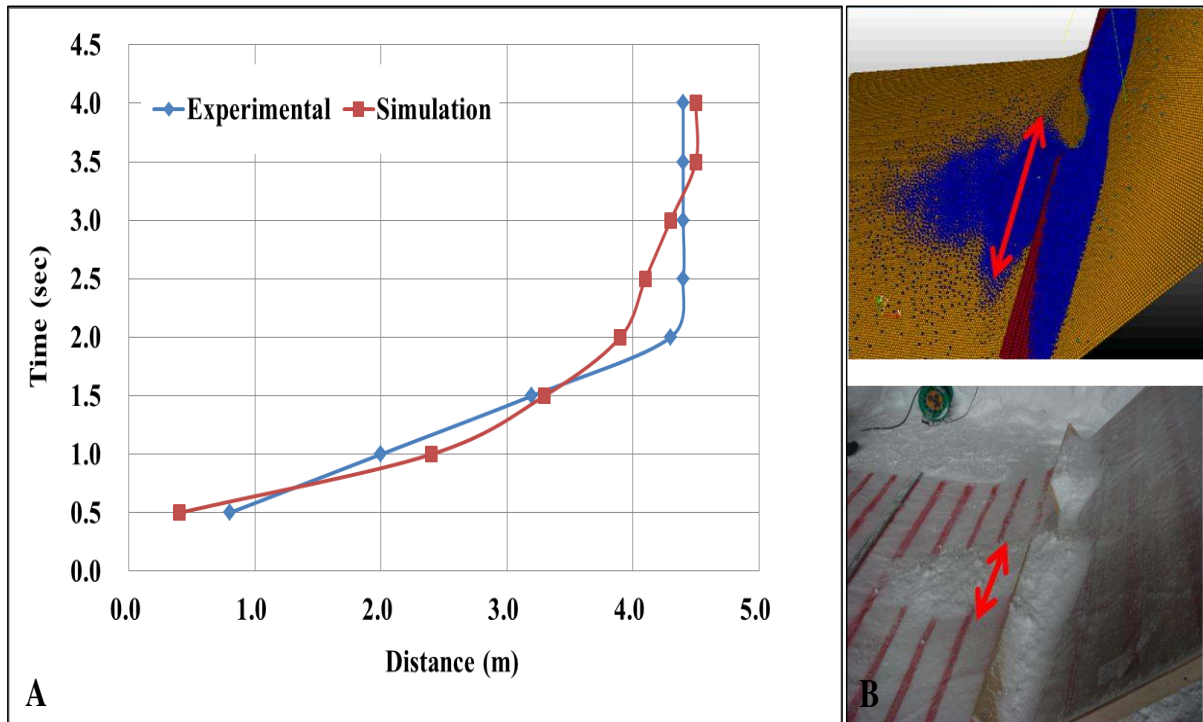


Fig 4.11 Case of obstacle with notched opening: (A) Avalanche propagation, (B) Deposition shape in the simulation and the experiment at t= 4 Sec

In case 2 when stakes raw were installed in the bottom of the slope part with narrow spacing, some snow was deposited above the stacks in the experimental results. It was successfully confirmed by the numerical results as shown in **Fig.4.9**.

In case 3 wider spacing between stake rows in the bottom of the slope part were installed. There was no snow deposition above the stakes raw in both experimental and numerical results as indicated in **Fig.4.10**.

In the case of the notched opening, we found a difference between the experimental and the numerical results. The particle spreading in the transverse direction is much wider in the numerical results than that of experiment (**Fig.4.11**). The simulated particles also continue on moving and gradually flow down from the edges, unlike the experimental results. This behavior of particles in simulated results is probably due including a change in snow properties.

Table 4.3 SPH computed water leading edge, compared with experimental data and MPS results.

Water Leading Edge	Results (m)		
	SPH	MPS	EXP
t = 0.5 s	0.40	0.45	0.50
t = 1.0 s	2.60	2.00	1.95
t = 2.0 s	3.90	3.80	4.00
t = 3.0 s	4.20	4.10	4.20
t = 4.0 s	4.25	4.15	4.20

In engineering practice, it is more common to study the macro flow such as the position of the leading edge. To provide useful information on this and also quantify the simulation errors, the SPH computed snow leading edge at five time instants ($t = 0.5$ s, 1.0 s, 2.0 s, 3.0 s and 4.0 s) are compared with the experimental data and MPS results for case 2 in **Table 4.3**. It shows that both numerical models can reasonably predict the experimental observations. Generally speaking, MPS seemed to better predict the early stage of the avalanche flow while SPH better predict the later stage.

Table 4.4 shows the total time elapsed in hour to simulate all cases. We can notice that the total computational time using SPH method is 1.50 times smaller than MPS method. (The same spacing between particles was used).

Table 4.4 Total time elapsed (hr.)

	Total time elapsed (hr.)	
	SPH	MPS
Case 1	29.25	43.86
Case 2	28.18	41.55
Case 3	29.48	42.35
Case 4	28.22	43.10

4.6. SUMMARY

A 3-D simulation of 5.4 m long inclined snow avalanches experiment with different types of obstacles was conducted using the SPH method. SPH is a mesh free, Lagrangian and particle-based method. This method is based on a discretization of the Navier-Stokes equations through employing particles and its interactions to simulate snow as a flow regime. Bingham model was employed to calculate the snow viscosity with implementation of Mohr-Coulomb failure equation.

The results of different cases of the snow Avalanches experiment were compared with the simulated results and a good agreement has been observed. This agreement includes similarities in the leading edge positions, the travel length of snow and spreading of the particles. Results show that the proposed model provides an accurate prediction and could be considered a powerful tool for estimating the behavior of snow avalanches.

Chapter 5

Simulation of three-dimensional rapid free-surface granular flow past different types of obstructions using the SPH method

In nature, when hazardous geophysical granular flows impact on an obstacle as they stream down on a slope, rapid changes in flow depth, direction, and velocity will occur. It is important to understand how granular material flows around such obstacles in order to enhance the design of defense structures. In this study, a 3D-SPH model is developed to simulate granular flow past different types of obstacles. The elastic-perfectly plastic model with implementation of the Mohr-Coulomb failure criterion is applied to simulate the material behavior, which describes the stress states of soil in the plastic flow regime. The model was validated by simulating the collapse of a 3D-column of sand with two different aspect ratios, the results showed that the SPH method is capable of simulating granular flow. The model is then applied to simulate the gravity-driven granular flow down an inclined surface obstructed by a group of columns with different spacing, a circular cylinder, and a tetrahedral wedge. Numerical results are then compared with experimental results, and two different numerical solutions. The good agreements obtained from these comparisons have demonstrated that the SPH method could be a powerful method for simulating granular flow and can be extended to design protective structures.

5.1. INTRODUCTION

Natural granular flows such as soil liquefaction, debris flows and snow avalanches cause damage to properties and lead to the loss of human life (Armstrong et. al., 1992). Such types of flows frequently impact on obstructions as they stream down on an inclined surface, producing fast changes in flow height and velocity in their neighboring region (e.g. Tai and Gray, 2001; Stuart B Savage, 2001; Johnson and Gray, 2001; Gray et. al., 2003; Hakonardottir and Hogg, 2005; Cui et. al., 2007; Gray and Cui 2007; Vreman et. al., 2007; Jóhannesson et. al., 2009). Studying granular materials and their deformation mechanism around such obstacles is very important for designing defenses and dissipating structures (e.g. Sigurdsson et. al., 1998; Tai et. al., 1999; Cui et. al., 2007; Hauksson et. al., 2007; Jóhannesson et. al., 2009), such as, straight or curved walls, pyramidal (tetrahedral), and cylindrical type structures to save lives and infrastructure.

The simulation of granular flow often involves modeling large motions of discrete particles, as well as modeling the deformation of the soil mass. In previous studies, many methods such as the Discrete Element Method (Silbert et. al., 2001; Faug et. al., 2009), the Finite-Element Method (Kabir et. al., 2008), and the depth-averaged shallow-water type theories that have additional momentum source terms (e.g. Grigourian et. al., 1967; Savage and Hutter 1989; Iverson 1997; Gray et. al., 1999, 2003; Mangeney-Castelnau et. al., 2003) have been utilized to solve problems dealing with granular materials. However, using the Discrete Element Method is limited to small-scale problems because it is computationally demanding.

Moreover, the Finite-Element Method cannot handle problems with large deformations at which mesh distortion may occur.

Recently a new class of numerical methods, which are called mesh-free methods, has been developed. Mesh-free methods do not require Eulerian grids and they deal with a number of particles in a Lagrangian framework. They are considered more effective than Eulerian methods in dealing with large-scale problems involving large deformations. The key idea of these methods is to provide an accurate and a stable numerical solution of partial differential equations using a set of distributed particles in the physical domain without using any grids.

Many mesh-free methods have been developed in the last decades, such as the Moving Particles Semi-implicit Method (MPS), the Diffuse Element Method (DEM), the Element-Free Galerkin Method (EFG / EFGM), and the Finite Pointset Method (FPM), etc. Among these methods, the Smoothed Particle Hydrodynamics (SPH) method is widely used. Smoothed Particle Hydrodynamics is a mesh-free lagrangian method developed independently by Lucy in 1977 and Gingold & Monaghan in 1977 in order to solve astrophysical problems in three-dimensional open space. It has been successfully applied to a huge range of applications such as the dynamic response of material strength (Libersky and Petschek, 1991), free surface fluid flow (Monaghan, 1994; Abdelrazek et. al., 2014), incompressible fluid flow (Cummins and Rudman, 1999), multi-phase flow (Monaghan and Kocharyan, 1995), turbulent flow (Monaghan, 2002), and snow avalanches (Abdelrazek et. al., 2014). In the SPH method, each particle in the domain conveys all fields' variable data such as density, pressure, and velocity, and it moves with the material velocity. The governing equations in the form of partial differential equations are converted to the particle equations of motion and after that they are solved using a suitable numerical scheme (the Predictor-Corrector algorithm). In the present study, the elastic–perfectly plastic model based on Mohr–Coulomb's failure criterion is implemented in SPH formulations to model the granular movement.

The motivation of this study is to test the predictive power of the SPH method to simulate 3D granular flows past different types of obstacles which involve large deformations. First of all, the model was validated by simulating the collapse of 3D axisymmetric sand columns with two aspect ratios to check the applicability of SPH in simulating the granular flow. The results showed a good agreement with experimental results in terms of the final runoff distance and the deposition shape. Secondly, the model applied to simulate the gravity granular flow down an inclined plane obstructed by three different types of obstacles. The numerical results from these three cases are then compared with experimental data. They are also compared with the hydraulic avalanche model solution for the second case, and the Savage and Hutter theory solution for the third case. The results obtained from this study indicate a good agreement in terms of the formation of shock waves, dead zones and granular vacuums, and have shown that SPH could be a powerful method for simulating granular flows. In the following sections, the governing equations in the SPH method are discussed, as well as the implementation of soil constitutive models in the SPH framework. The results of the calculations are then introduced and discussed.

5.2. GOVERNING EQUATIONS

The governing equations of dry soil in the framework of SPH consist of linear momentum and continuity equations expressed as follows:

$$\frac{Dv^\alpha}{Dt} = \frac{1}{\rho} \left(\frac{\partial \sigma^{\alpha\beta}}{\partial x^\alpha} \right) + f^\alpha \quad (5.1)$$

$$\frac{D\rho}{Dt} = -\rho \frac{\partial v^\alpha}{\partial x^\alpha} \quad (5.2)$$

where α and β denote the Cartesian components x , y and z with the Einstein convention applied to repeated indices, ρ is the density, v is velocity, $\sigma^{\alpha\beta}$ is stress tensor, f^α is the component of acceleration caused by external force, and D/Dt is material derivative, which is defined as,

$$\frac{D}{Dt} = \frac{\partial}{\partial t} + v^\alpha \frac{\partial}{\partial x^\alpha} \quad (5.3)$$

Usually the stress tensor, $\sigma^{\alpha\beta}$, consists of two parts: anisotropic pressure P and a deviatoric stress S ,

$$\sigma^{\alpha\beta} = -P\delta^{\alpha\beta} + S^{\alpha\beta} \quad (5.4)$$

5.3. CONSTITUTIVE EQUATIONS FOR SOIL

Modeling the behavior of dry soil using the SPH method is similar to that of water, in which the soil is presumed to behave as quasi compressible material. The soil is approximated by an artificial material which is more compressible than the real one; this is called the artificial compressibility technique (Liu and Liu, 2003). The key difference between these two models is in the calculating of the stress tensor, in which the pressure and stress-strain relationship of soil are calculated differently. Following Bui et. al., 2007 the soil is assumed herein to be an elastic-plastic material. The pressure term in equation (5.4) is normally calculated using “equation of state”, which has a function of density change (One of the fundamentals of the SPH method); the pressure equation of soil will obey Hooke’s law (Bui et. al., 2007):

$$P = -K \frac{\Delta V}{V} = K \left(\frac{\rho}{\rho_0} - 1 \right) \quad (5.5)$$

where K is bulk modulus, $\Delta V/V$ is the volumetric strain, and ρ_0 is the initial density of soil. Using the real value of K will result in a stiff behavior of soil. Therefore, K should be chosen as small as possible in order to ensure the nearly incompressibility condition and to avoid the stiff behavior (minimizing pressure fluctuations). This study chooses $K = 50 \rho_0 g H_{max}$ for the pressure equation (50 times the maximum initial pressure).

Since the soil is assumed to have elastic behavior (Bui et. al., 2007, 2008 and 2010; Yaidel et. al., 2012), the rate of change of deviatoric shear stress, dS/dt , can be calculated using shear modulus, μ , using the Jaumann rate from the following constitutive equation:

$$\frac{dS^{\alpha\beta}}{dt} = 2\mu \left(\dot{\varepsilon}^{\alpha\beta} - \frac{1}{3} \dot{\varepsilon}^{\gamma\gamma} \delta^{\alpha\beta} \right) + S^{\alpha\gamma} \omega^{\beta\gamma} + \omega^{\gamma\beta} S^{\alpha\gamma} \quad (5.6)$$

where $\dot{\varepsilon}^{\gamma\gamma} = \dot{\varepsilon}^{xx} + \dot{\varepsilon}^{yy} + \dot{\varepsilon}^{zz}$, $\dot{\varepsilon}$ is the strain rate tensor and $\omega^{\gamma\beta}$ is the rotation rate tensor. It can be defined by,

$$\dot{\varepsilon}^{\alpha\beta} = \frac{1}{2} \left(\frac{\partial v^\alpha}{\partial x^\beta} + \frac{\partial v^\beta}{\partial x^\alpha} \right) \quad (5.7)$$

$$\omega^{\alpha\beta} = \frac{1}{2} \left(\frac{\partial v^\alpha}{\partial x^\beta} - \frac{\partial v^\beta}{\partial x^\alpha} \right) \quad (5.8)$$

5.4. DISCRETIZATION OF GOVERNING EQUATIONS

Using the concept of the SPH approximation the system of partial differential equations (5.1) and (5.2) can be converted into the SPH formulations which will be used to solve the motion of the particles representing the soil as follows:

$$\frac{D\rho_i}{Dt} = \sum_{j=1}^N m_j (v_i^\alpha - v_j^\alpha) \frac{\partial W_{ij}}{\partial x_i^\alpha} \quad (5.9)$$

$$\frac{Dv_i^\alpha}{Dt} = \sum_{j=1}^N m_j \left(\frac{\sigma_i^{\alpha\beta}}{\rho_i^2} + \frac{\sigma_j^{\alpha\beta}}{\rho_j^2} \right) \frac{\partial W_{ij}}{\partial x_i^\beta} + f^\alpha \quad (5.10)$$

Similarly, the SPH approximation of the strain rate tensor and the rotation rate tensor for particle i can be expressed as following:

$$\varepsilon_i^{\alpha\beta} = \frac{1}{2} \sum_{j=1}^N \left(\frac{m_j}{\rho_j} (v_i^\alpha - v_j^\alpha) \frac{\partial W_{ij}}{\partial x_i^\beta} + \frac{m_j}{\rho_j} (v_i^\beta - v_j^\beta) \frac{\partial W_{ij}}{\partial x_i^\alpha} \right) \quad (5.11)$$

$$\omega_i^{\alpha\beta} = \frac{1}{2} \sum_{j=1}^N \left(\frac{m_j}{\rho_j} (v_i^\alpha - v_j^\alpha) \frac{\partial W_{ij}}{\partial x_i^\beta} - \frac{m_j}{\rho_j} (v_i^\beta - v_j^\beta) \frac{\partial W_{ij}}{\partial x_i^\alpha} \right) \quad (5.12)$$

By combining Equations (5.6), (5.11) and (5.12), the deviatoric shear stress components can be calculated. Then, they are compared with the maximum shear stress ($S_f = c + P \tan\phi$) in the plastic flow regime of the soil, which determined by the Mohr–Coulomb failure criterion. Here c is soil cohesion and ϕ is the angle of internal friction of the soil.

In order to damp out the unphysical stress fluctuation, prevent shock waves, and to prevent unphysical penetration for particles approaching each other, an artificial viscosity (π_{ij}) has been employed to the pressure term in the momentum equation. The most widely used type is proposed by Monaghan and Lattanzio (1985), and the momentum equation after introducing the artificial viscosity becomes in the following form:

$$\frac{Dv_i^\alpha}{Dt} = \sum_{j=1}^N m_j \left(\frac{\sigma_i^{\alpha\beta}}{\rho_i^2} + \frac{\sigma_j^{\alpha\beta}}{\rho_j^2} + \pi_{ij} \right) \frac{\partial W_{ij}}{\partial x_i^\beta} + f^\alpha \quad (5.13)$$

5.5. TEST CASE

In order to validate our model and show its capability, numerical simulations were conducted to simulate the experiments done by Lube (2004) on the collapse of a vertical, three-dimensional, axisymmetric column of sand. Lube (2004) pointed out that the flow behavior of

granular columns relies on the aspect ratio $a = H_i/R_i$, where H_i and R_i are the initial height and radius of the granular column, respectively.

They concluded that the final runoff distance and collapsed column height can be expressed only in terms of aspect ratio and the initial radius, and is independent of any friction coefficient. Two experiments were selected with an aspect ratio equal to 0.9 and 2.75, and simulated using the SPH model.

The initial radius of the column was 0.1 m and the numbers of fluid particles used in these simulations were 22590 and 69025, with 0.005 m initial distance between particles. The used values of the Young's modulus, the Poisson ratio, friction angle, and density are 5 Mpa, 0.3, 30o and 2600 Kg/m³, respectively.

Fig. 5.1 shows a comparison between the numerical and experimental results for the collapse of the sand column with $a = 0.9$. The numerical results show a good agreement with the experimental results in terms of the final run-out distance and deposit profile. However, we have indicated differences in terms of the final top shape of the cone and its sharpness. Lube et. al., (2004) indicate that a very sharp cone at the top of the final cone remains at the initial height, but in the SPH simulation, a slight decrease in the final height is observed as shown in figure 3 (c). This is probably because the number of particles is not adequate to give smooth and reliable results or because of the truncation error that resulted from the approximation of spatial derivatives. Many modifications and improvements have been proposed to the SPH method to overcome these types of errors (Amicarelli et. al., 2011; Hopkins, 2014), but they are not considered in this study. Moreover, a zero dilation angle of sand is assumed for simplicity, which led to a weaker soil in the SPH model (Chen and Qiu, 2012). In addition, the angle of repose, after the soil collapse in the simulation, is slightly smaller than that obtained from the experimental results.

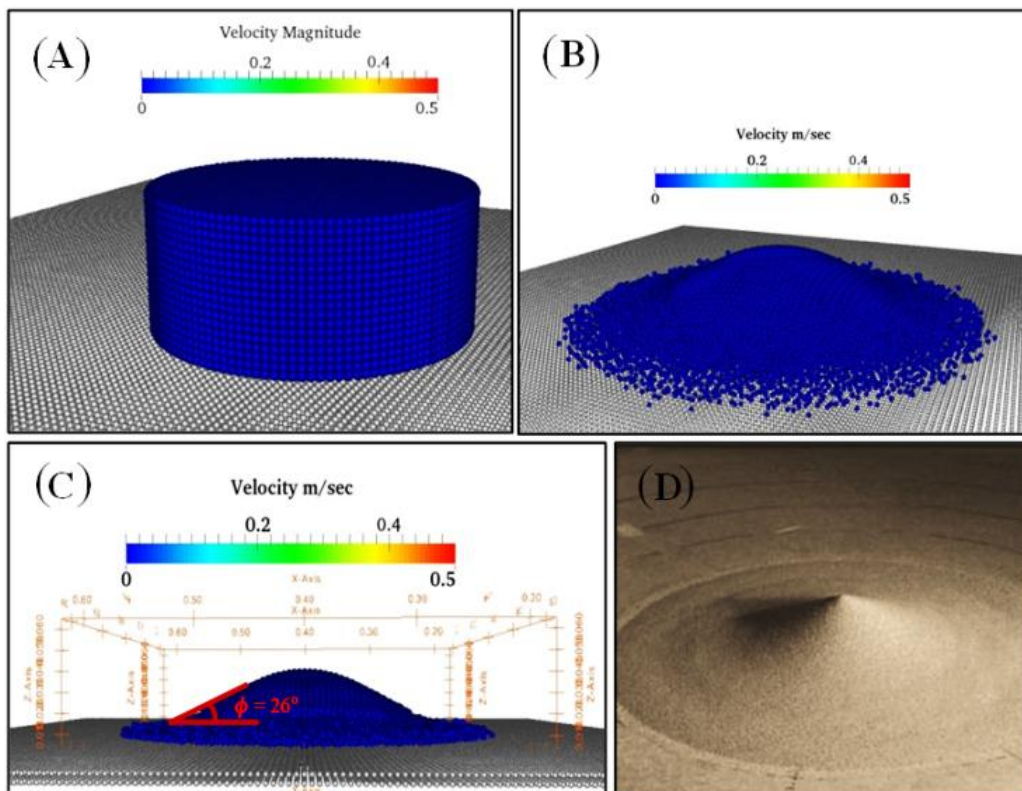


Fig 5.1 Comparison between experimental and numerical results: (A) initial shape of sand column; (B) simulated final profile; (C) side view of the simulated final profile; (D) experimental final profile (Lube et al. 2004)

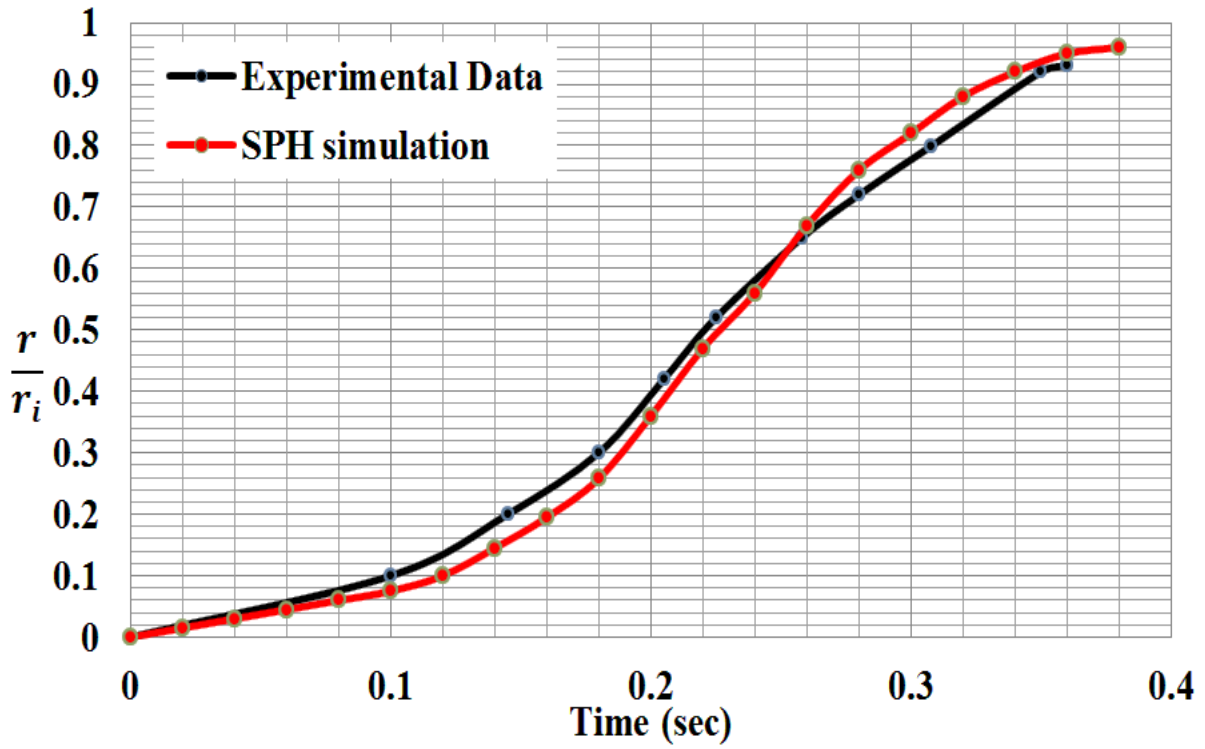


Fig 5.2 Typical radial displacements as functions of time

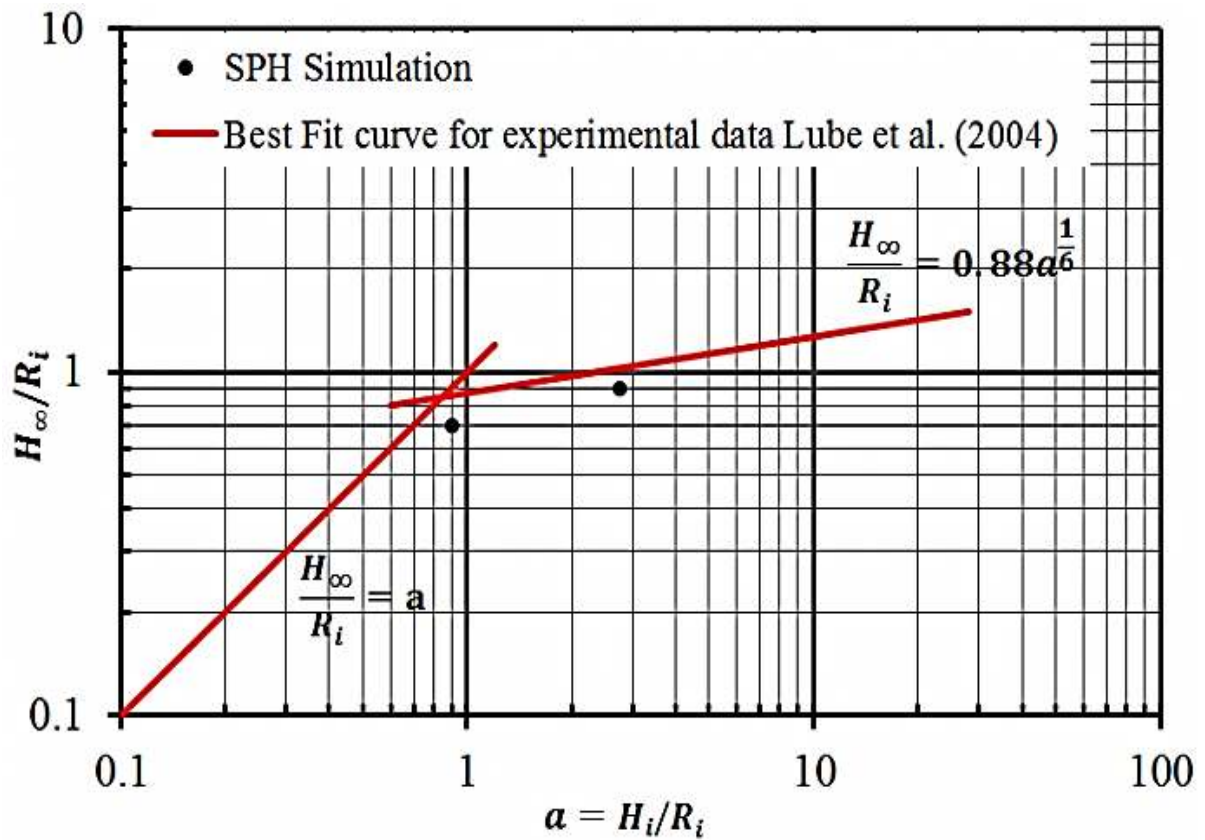


Fig 5.3 Comparison of normalized final deposit height between the simulations and experimental results

Fig. 5.2 represents a comparison between experimental and numerical results in terms of the radius of the flow front as functions of time for the case with an aspect ratio equal to 0.9. Even though there are small differences between the SPH and experimental results, the model is in a good quantitative agreement with the experiment, both in the position of the radius of the flow front and the time scale for their formation. Also, the flow patterns in both experiment and simulation have a primary acceleration phase followed by a deceleration phase.

Fig. 5.3 shows a comparison of the normalized final deposit height of the SPH simulations in the two cases, together with a fit curve from the experimental data observed by Lube et. al, (2004). It illustrates that the computed final deposit height is slightly lower than the values predicted from the experimental data.

5.6. RESULTS AND DISCUSSIONS

In this section, SPH will be applied to simulate Geotechnical materials through three main problems to test the abilities of the proposed method. First, SPH will be applied to simulate a small-scale granular avalanche flow down an inclined surface obstructed by a group of stake rows with different spacing. Through this case study, we will show that SPH can capture the deposition shape at the end of the slope. Next, the SPH model is applied to simulate the 3D granular free-surface flow around a circular cylinder which considers common obstacles such as tree trunks, and is a fundamental practical interest to the design of pylons that are able to show steadfastness in front of such kinds of flows (Sovilla et. al., 2008).

Finally, the SPH method will be used to carry out 3D simulations of the gravity granular flow past a pyramid wedge (tetrahedral) which is used as a typical defense structure to divert flow and guide avalanches to pass the protected buildings and areas.

5.6.1. Gravity granular flows past a group of stake rows

5.6.1.1. Model description

This laboratory experiment was conducted by Yellin and others (2013) in the Hydraulics Research Laboratory at Hokkaido University. **Fig. 5.4** shows a schematic diagram illustrating the dimensions of the experiment and the initial position of the sand mass. The model was built from two wooden panels; each of them is 1.80 m long and 0.90 m wide. The first panel was inclined at 20° with the horizontal and the obstacles were placed at a distance of 30 cm from its top. The inclination of the second panel was 45° . An amount of quartz sand (2.04 kg) was initially filled in the starting box, located 30 cm from the top of the second panel. Grid lines were drawn on the panels, with 10 cm intervals in order to know the particle positions and their speed.

These experiments were originally conducted as a starting point to design energy dissipators for the snow avalanche. We used three different types of obstacles as shown in **Fig. 5.5**:

Case1: 1cm square columns with 1 cm spacing.

Case2: 2cm square columns with 2 cm spacing.

Case3: 1cm square columns in a staggered shape.

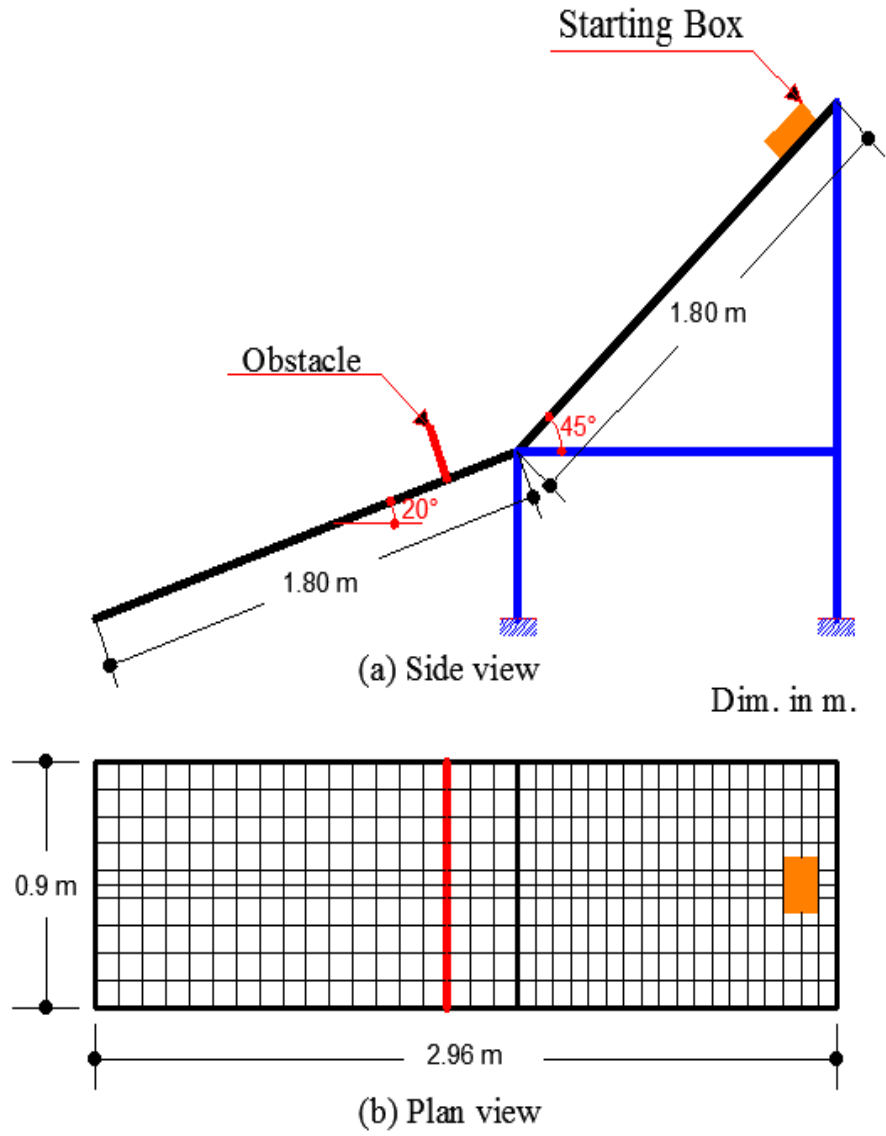


Fig 5.4 Schematic sketch of the avalanche experiment

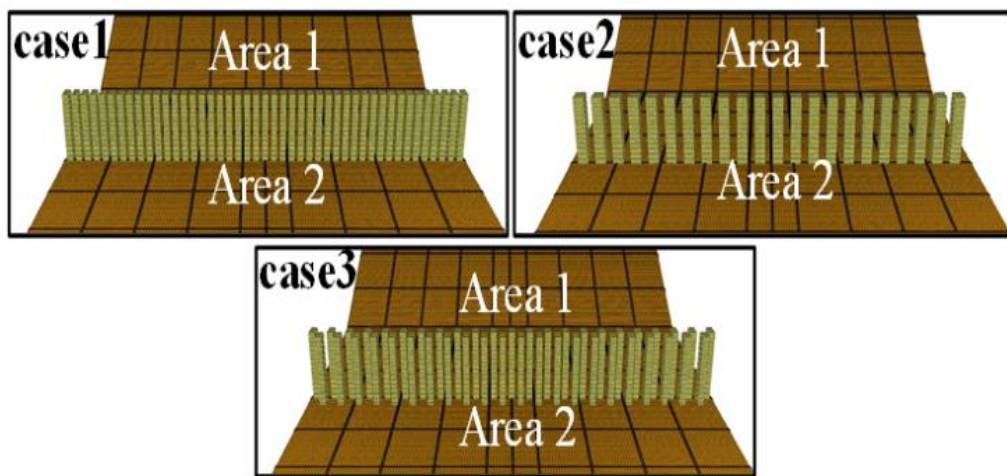


Fig 5.5 The different types of obstacles and areas name

5.6.1.2. Numerical simulations

The simulation of the granular flows was carried out using the proposed SPH model. The number of particles used to simulate the soil mass was 12054, with 0.005 m initial distance between particles. These particles had the following properties: density $\rho = 1500 \text{ kg/m}^3$, Young's modulus $E = 150 \text{ Mpa}$, internal friction angle $\phi = 32^\circ$, and passion ratio $\nu = 0.3$.

5.6.1.3. Results and analysis

Figs. 5.6 – 5.8 show a comparison between the experimental and numerical results in terms of the final deposition shape and particles spreading at the three cases. A good agreement between simulated and experimental results is found when we used a suitable number of particles. However, we can notice that the final simulated deposition shapes are almost symmetrical around the longitudinal centerline unlike the deposition forms resulting from the experiments. Also, in Cases 1 and 3, some particles deposited above the obstacle in the experimental results while in Case 2, with the wider spacing between obstacles, there is no deposition above the obstacle. Those results are successfully confirmed by the numerical results.

Fig. 5.9 represents a comparison between experimental and numerical results in terms of the position of the leading edge versus time for Case 1. Although there are small differences between the SPH and experimental results, the positions of the leading edge stay almost the same in both numerical and experimental results until $t = 1.4 \text{ s}$. After that, the speed of the particles in the experiment decreased, and finally stopped at $t = 3.0 \text{ s}$, while the simulated particles moved faster until $t = 1.7 \text{ s}$, then gradually stopped at $t = 3.2 \text{ s}$.

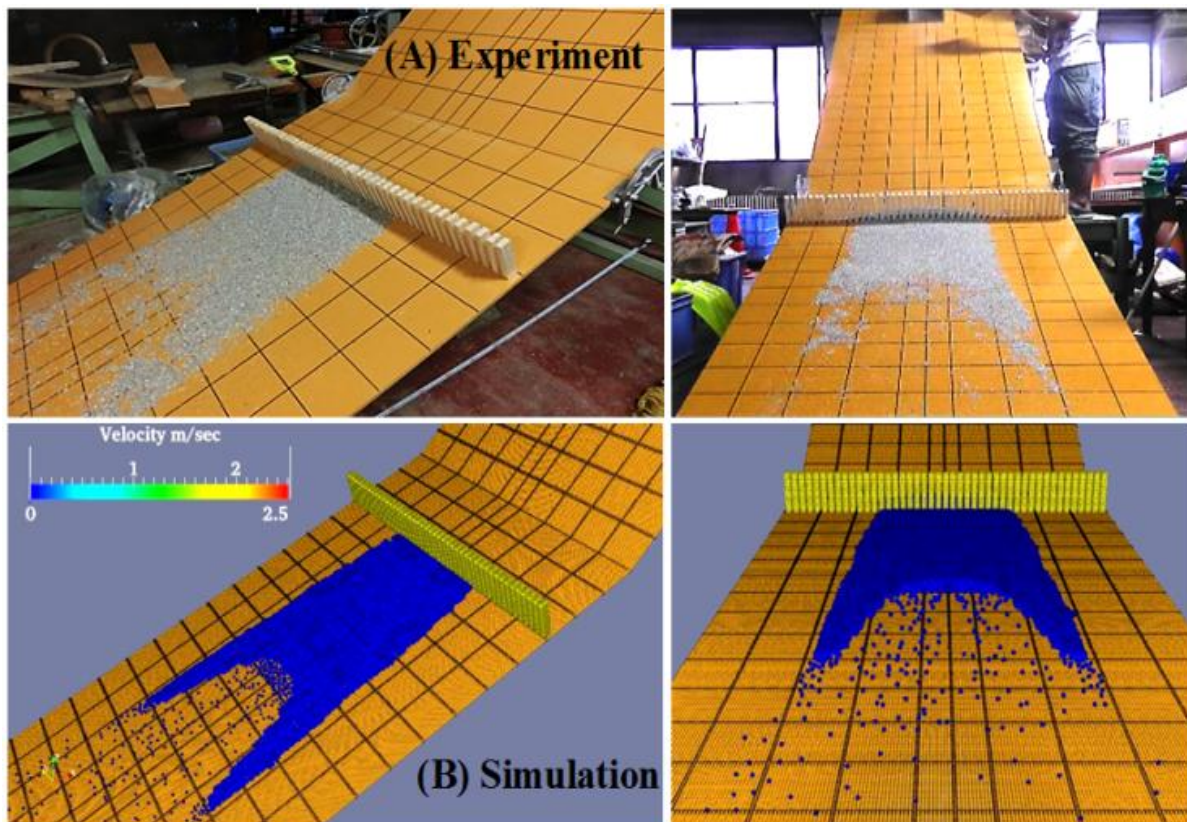


Fig 5.6 Comparison between the (A) experimental and (B) numerical results in term of the final deposition shape (case1).

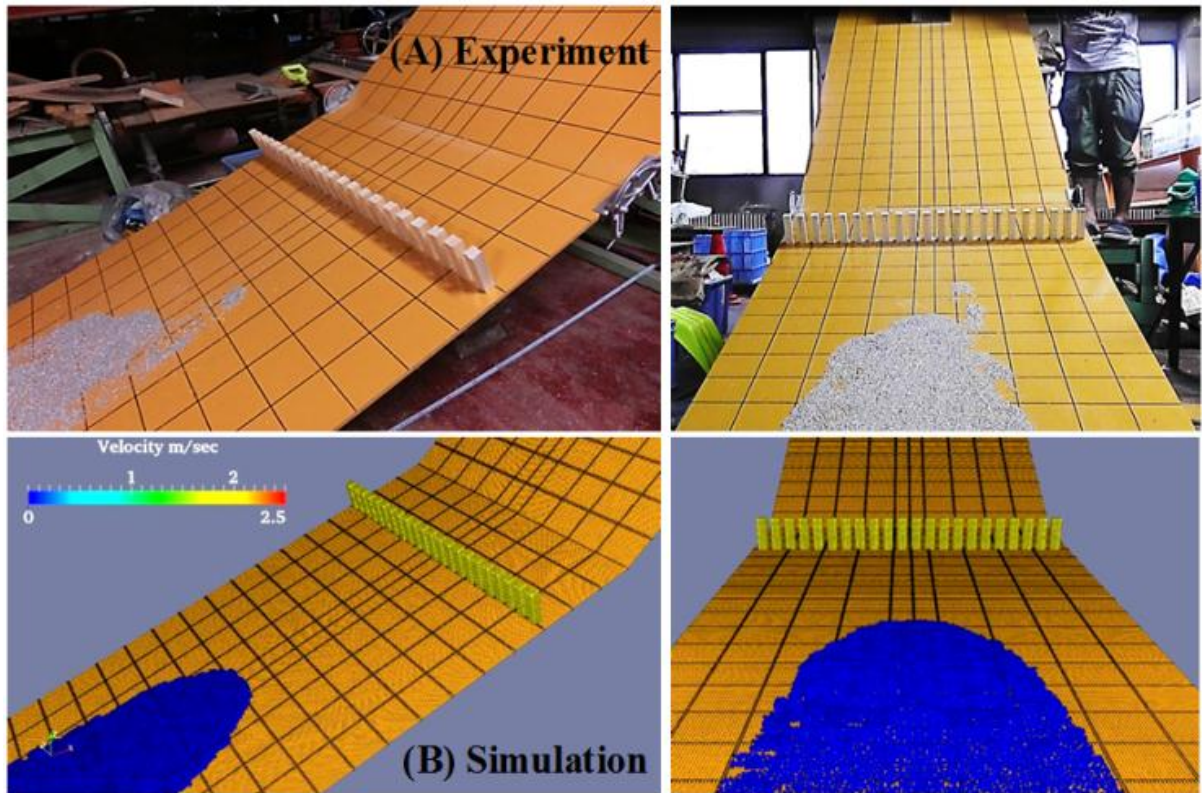


Fig 5.7 Comparison between the (A) experimental and (B) numerical results in term of the final deposition shape (case2)

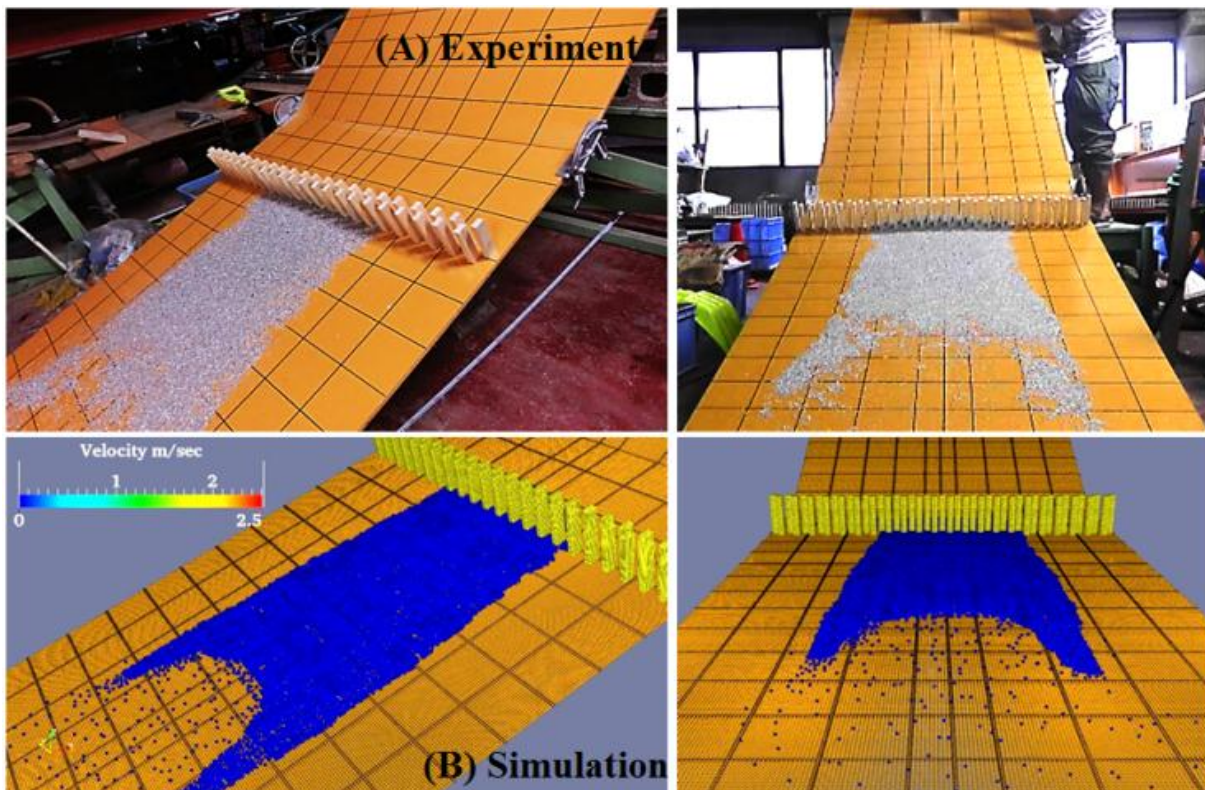


Fig 5.8 Comparison between the (A) experimental and (B) numerical results in term of the final deposition shape (case3)

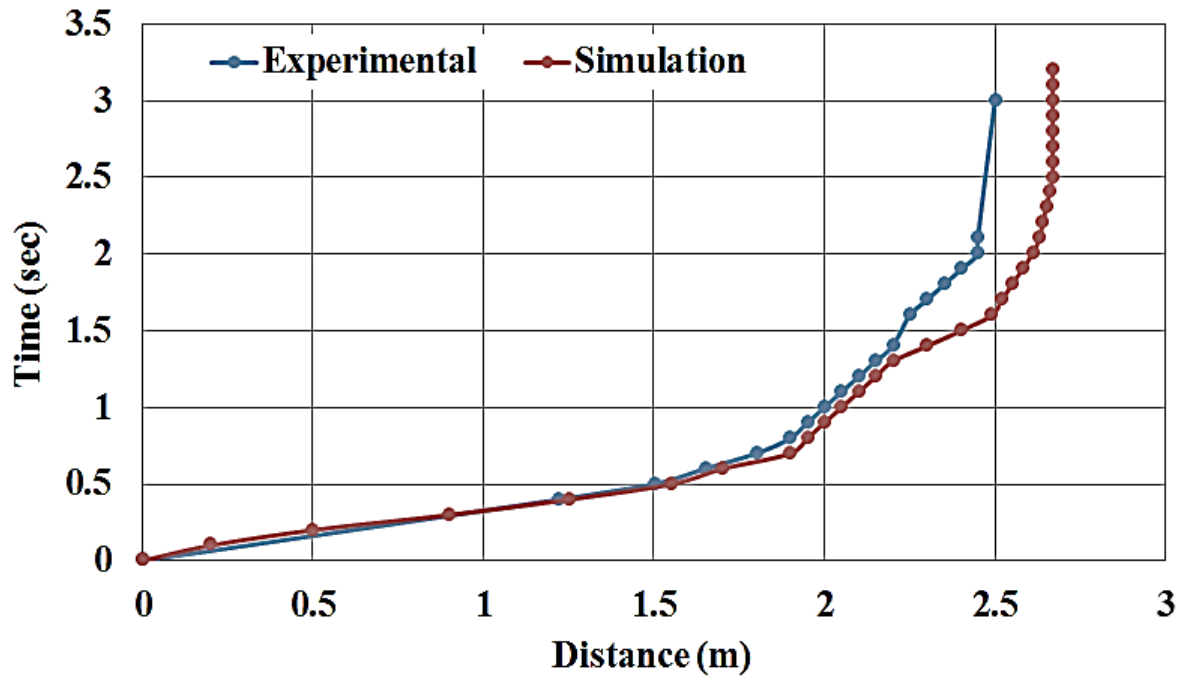


Fig 5.9 Position of leading edge with time (case1)

In order to investigate the efficiency of the obstacles, Yellin (2013) named the area upstream the obstacles as Area 1, and the area downstream the obstacles as Area 2, as shown in **Fig. 5.5**, and then they measured the weight of deposited sand in each area to derive an efficiency factor of the obstacles as, $\text{Efficiency factor} = (A1+A2 / 2.04 \text{ kg}) \times 100\%$. In our simulations, we counted the number of deposited particles in those areas. **Table 5.1** shows the efficiency factor for the experimental and simulated results. Although the efficiency factor from the experimental results in all cases is slightly greater than that calculated from the SPH results, the error is about 5 %.

Table 5.1 Efficiency factor for the different cases

		Area 1	Area 2	Efficiency factor %
Case 1	Exp. (Kg)	0.45	1.1	76
	SPH (No.)	2943	5736	72
Case 2	Exp. (Kg)	0.06	0.92	48
	SPH (No.)	0	5184	43
Case 3	Exp. (Kg)	0.38	1.25	80
	SPH (No.)	2107	7054	76

5.6.2. Granular free-surface flow around a circular cylinder

5.6.2.1. Model description

Small-scale experiments were carried out by Cui X. et.al, (2013) used to investigate the gravity-driven free-surface flow of a granular avalanche around a circular cylinder.

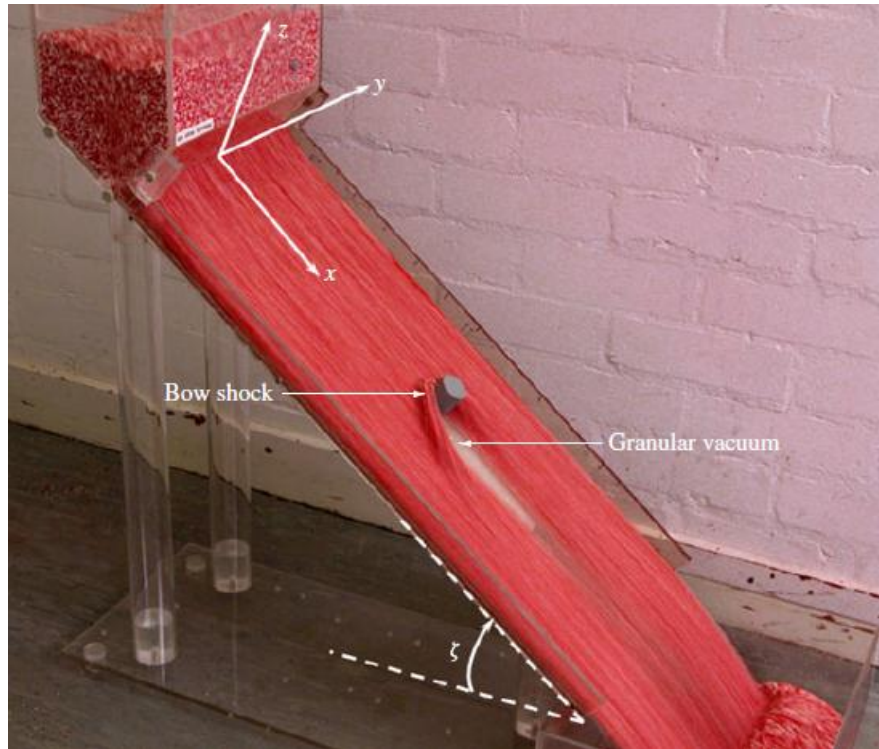


Fig 5.10 Experimental set-up showing the flow past a circular cylinder on a chute inclined at an angle ζ to the horizontal.

The experimental setup was built using a smooth Plexiglas chute that is 300 mm wide and 600 mm long and is inclined at an angle $\zeta = 36^\circ$ to the horizontal as shown in **Fig. 5.10**.

The sand was loaded into a hopper at the top of the chute, and a gate was used to control the height and flux of material entering the chute. A 30 mm diameter circular metal cylinder is attached to the center of the chute 300 mm downstream from the inflow gate, so that its axis is normal to the inclined plane.

All phases of the experiments were totally registered with a video and photo camera with a shutter speed of 1/20 of a second. In one second 25 pictures was taken (1 picture / 0.04 Sec), in order to show how the bow shock and the granular vacuum are formed in a close-up region near the cylinder.

5.6.2.2. Numerical simulations

In total 234675 soil particles with an initial distance 0.002 m are used to simulate the sand mass which initially found in the hopper at the top of the chute.

Table 5.2 Soil parameters

Parameter	Value
Density (kg/m^3)	$\rho = 1500$
Young's modulus (MPa)	$E = 150$
Friction angle	$\phi = 26^\circ$
Passion ratio	$\nu = 0.3$

Table 5.2 shows the values of the parameters used to simulate the flow of a granular avalanche around a circular cylinder.

The gate opening height is 0.4 dimensionless units since the cylinder diameter $D = 30$ mm is used in dimension scaling (30 mm = 1 dimensionless unit), and the velocities are scaled by $\sqrt{Lg} = 0.54$ m. s⁻¹ and time is scaled by $\sqrt{L/g} = 0.055$ sec.

5.6.2.3. Results and analysis

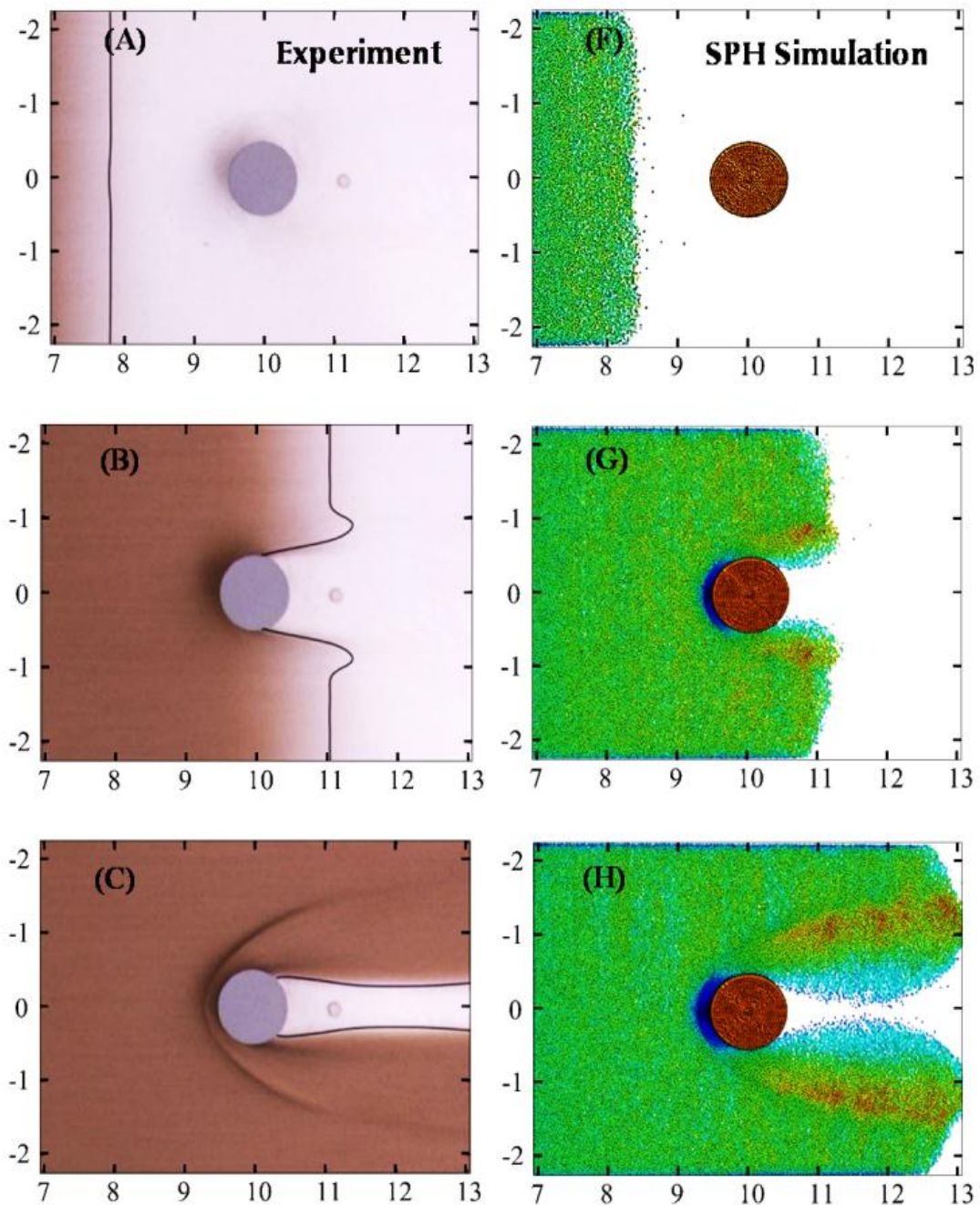


Fig 5.11 Comparison between computation and experiment results at different time steps ($t = 7.4, 8.12$ and 9.56 dimensionless units) showing the continuation of the time-dependent development of a bow shock and a vacuum boundary

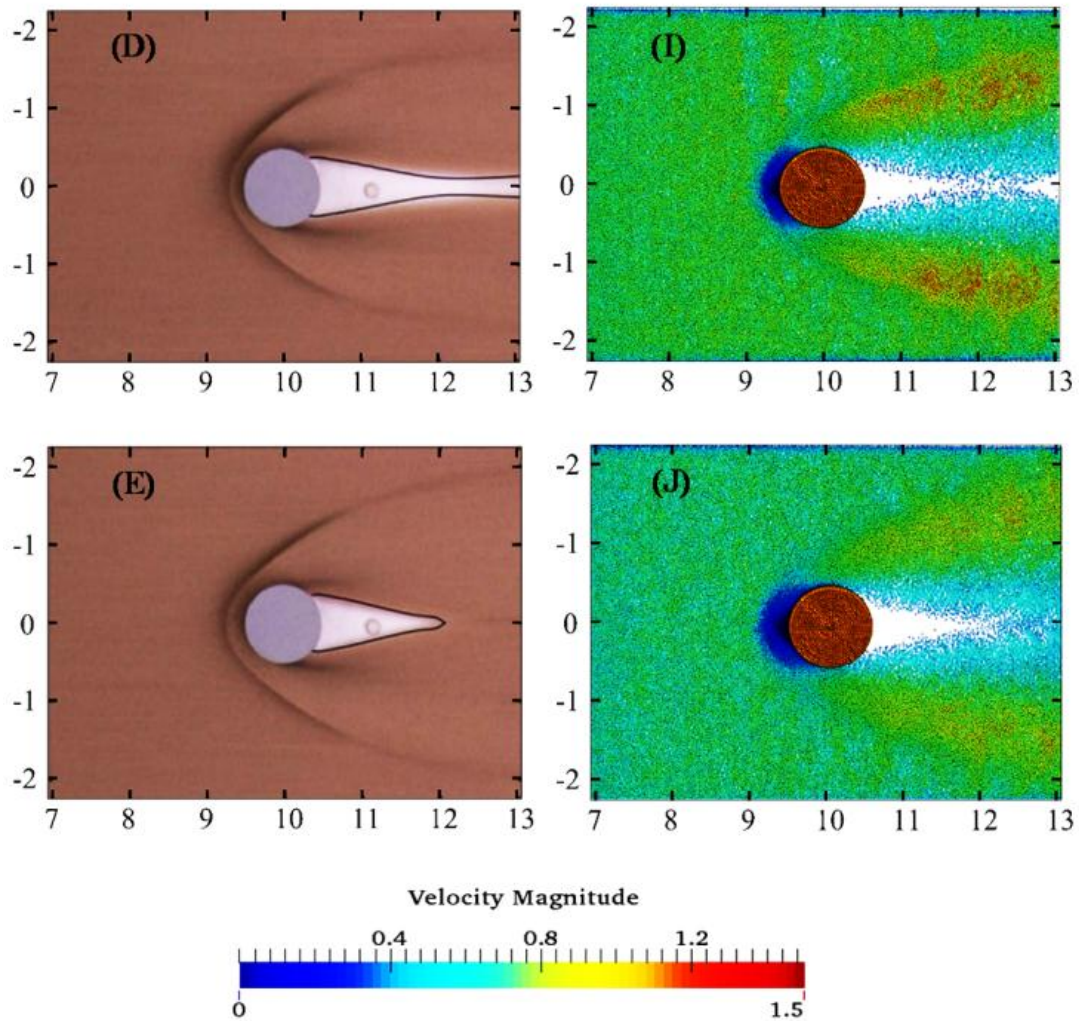


Fig 5.12 Conti- Comparison between computation and experiment results at different time steps ($t = 10.28$ and 12.44 dimensionless units) showing the continuation of the time-dependent development of a bow shock and a vacuum boundary

Figs. 5.11 and **5.12** present a series of snapshots of the avalanche hitting the circular cylinder, showing the particles positions and free-surface shape together with the velocity field at different times. The result obtained by the SPH method is compared with the experimental images and the superimposed computed boundary obtained from the hydraulic avalanche model solution by Cui et.al, (2013). The time intervals between snapshots are equal to 0.72 non-dimensional units. Since the gate was not in the camera shots, the comparison of the simulation and the experiment starts from the distance $x = 8$ units at the time $t = 7.4$ units.

When the particles released from the gate, the flow front starts to propagate uniformly, and the flow was fast and thin. When the particles start to hit the cylinder the flow continues to propagate downstream except the particles which collide with the obstacle and are largely affected by the obstacle (**Fig. 5.11 B, G**). A jump in flow thickness and velocity, which is named as “bow shock wave” start to developed at the front of the cylinder by $t = 8.84$ units (**Fig. 5.11 C, H**).

The bow shock continues to grow slightly in the height and to move upstream until the oblique shocks on either side of the obstacle are almost fully developed by $t = 10.28$ (**Fig. 5.12 D, I**). By $t = 12.44$ units, (**Fig. 5.12 E,J**), the flow reach a steady-state regime with no

further growth within the field of view, and the granular vacuum clearly appears downstream of the cylinder and forms a triangular shape.

The developing process of the bow shocks by the present computation is in a close agreement with the experimental results. For the vacuum boundary, the closed triangular region obtained by the simulation seemed to be bigger than the one formed in the experiment. Generally, we can indicate that this model captures most of the essential aspects of the present phenomena.

5.6.3. Gravity granular flows past tetrahedral wedge

5.6.3.1. The model description

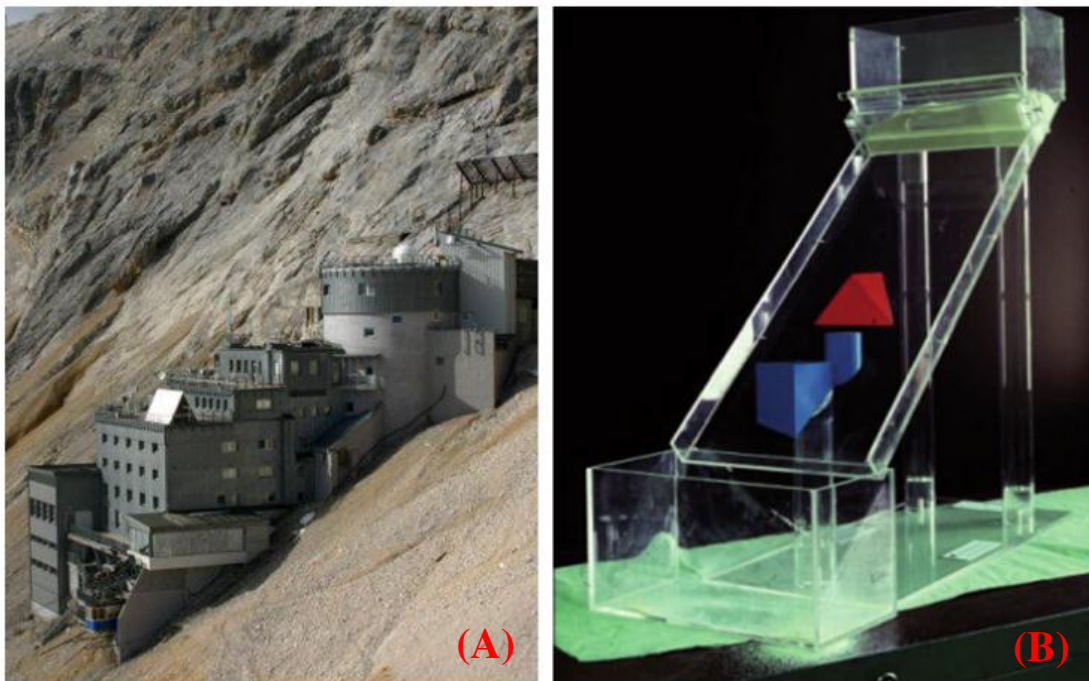


Fig 5.13 (A) The Schneefernerhaus at the Zugspitze, Germany at 2700 m on a rather planar mountain slope inclined at an angle approximately 45° . (B) A model reproduction together with tetrahedral wedge type avalanche protection

The tetrahedral wedge was proposed to protect the Schneefernerhaus at Zugspitze, Germany, against a large avalanche with a 100-year recurrence that equals to a snow layer of 8 m depth moving down the mountain (Yih-Chin T et.al., 1999). The Schneefernerhaus was an old hotel, and then it was renovated and transferred into a research laboratory for environmental and climatological research in 1999. It is situated on a mountain slope inclined by approximately 45° , shown in **Fig. 5.13_A**. In a first study of protecting this building against such an event, a tetrahedral wedge was designed that should divert the flow and guide the snow to pass the building on either side. Yih-Chin T. (2000) decided to carry out a laboratory experiments to simulate this event. Two models of the scales 1:100 and 1:300 were used to perform these experiments. In this study, the two scale experiments were simulated using the current SPH model. In the experiments, the mountain flank modeled as an inclined plane of a 45° slope angle is made from Plexiglas. The models of Schneefernerhaus and of the wedge were cut from plastic and wood blocks, respectively. Semolina flour with 0.8 mm in diameter and plastic beads were used as the model of “dry snow”. The internal angle of friction of these

materials is within the range of the snow. The used materials are initially filled in a tank with a gate at the upstream end of the slope. **Fig. 5.13_B** shows the experimental setup with scale 1:300.

5.6.3.2. Numerical simulations

The number of particles used to simulate the semolina mass was 165000, with 0.002 m initial distance between particles. The material constants used in the calculation for the two cases are illustrated in **Table 5.3**.

Table 5.3 Semolina parameters

parameter	Value	
	Semolina	Plastic beads
Density (kg/m ³)	$\rho = 600$	$\rho = 890$
Young's modulus (MPa)	$E = 5000$	$E = 900$
Friction angle	$\phi = 35^\circ$	$\phi = 38^\circ$
Passion ratio	$\nu = 0.49$	$\nu = 0.42$

5.6.3.3. Results and analysis

Fig. 5.14 shows three snapshots of the motion of a layer of semolina. This layer represents the motion of an 8 m layer down the slope, past and around the obstacle and the Schneefernerhaus building at three different stages compared with numerical results of the SPH simulations.

From the snapshots, we can see obviously how the obstacle diverts the flow. A normal shock is formed at the pyramid top and extends on both sides of the flanks of the pyramid to consist an oblique shock, which can be clearly seen from the streamlines in the photograph as well as the particles spreading in the numerical simulation. At the downstream region of the obstacle, the flow rapidly spreads in the transverse direction and forms an expansion fan far from the protected area, which is also well described by the SPH simulation.

Fig. 5.15 shows a comparison of three different results, the experimental results (scale 1:100), the numerical results obtained from applying the Savage and Hutter theory using the two-dimensional NOC scheme (Jiang and Tadmor, 1997), and the SPH simulation, representing the steady flow past the defence structure. The oblique shocks on both sides of the defence structure are clearly seen from the streamlines in the experiment, computed flow thickness from the two-dimensional NOC scheme, as well as the particle distribution together with the velocity field. Also, the particle-free region was formed, which shows that the protected zone is well described in the SPH results. From the above results, it is clear that the SPH method can well describe the properties of the flow around the tetrahedral obstacle and can quantitatively describe the protection region.

Fig. 5.16 demonstrates a horizontal cross section of the flow depth along the line $x = 5.6$ deimensionless units, which crosses the upper part of the pyramid at $t = 10$ dimensionless units. The Solid line represents the Savage and Hutter theory solution utilizing the two-dimensional NOC scheme, and the particles distribution gives the cross sectional shape obtained by the SPH simulation. The shocks are visible on either side of the defense structure. Behind the shock, the avalanche thickness is approximately four times that of the Savage and Hutter theory solution, and three times that of the present SPH model as large as in front of the shock. In the two solutions, the shocks are symmetrical though they have different shapes.

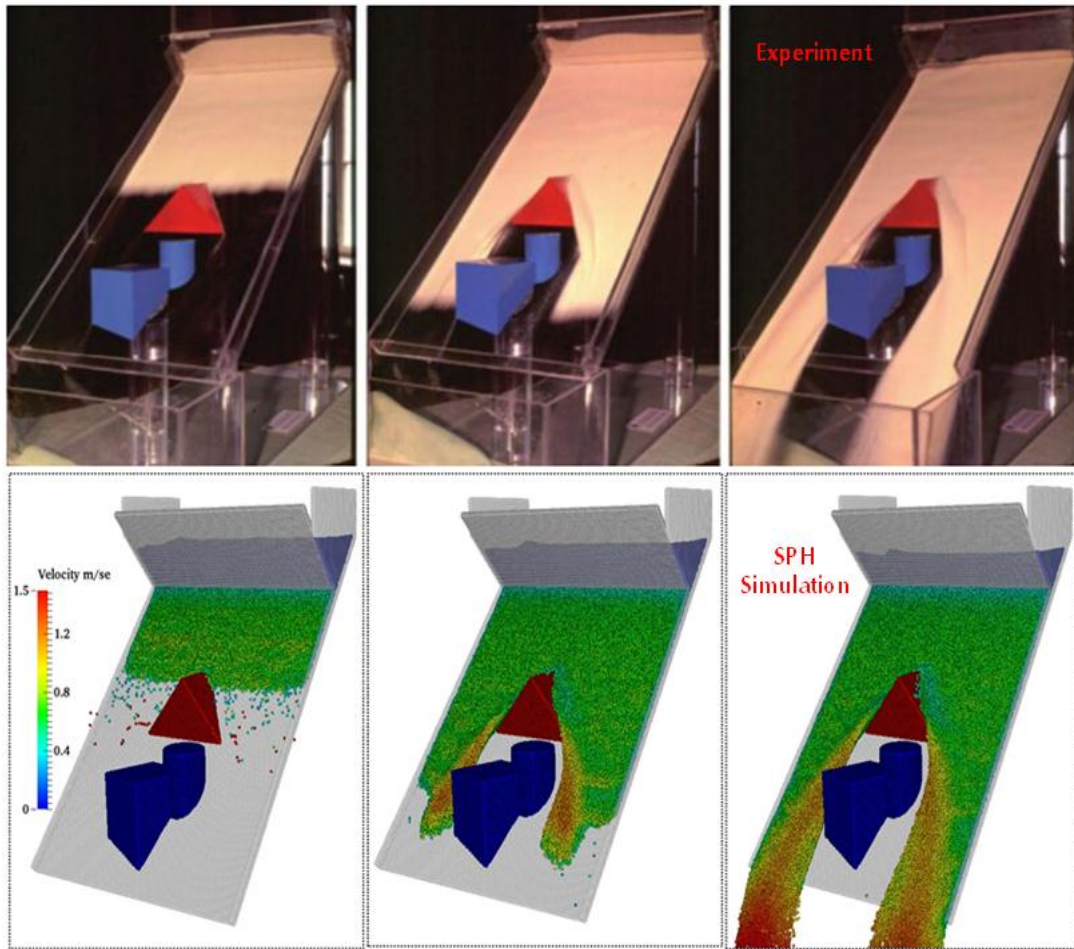


Fig 5.14 Comparison between experimental and numerical results at three different stages showing the motion of a layer of semolina past and around the obstacle and the Schneefernerhaus building

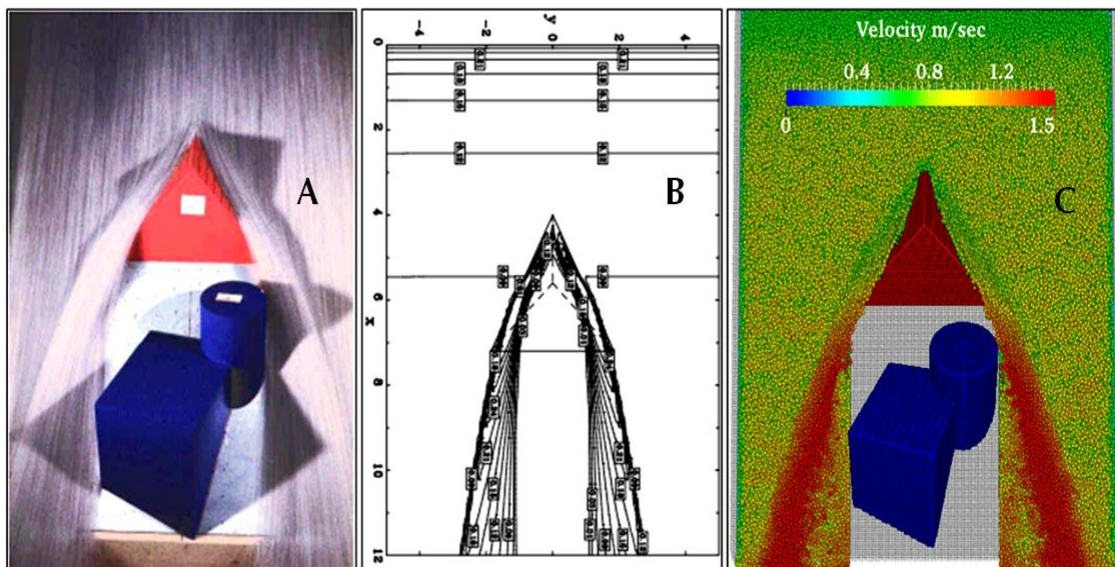


Fig 5.15 Comparison between (A) the experimental results (scale 1:100), (B) numerical results obtained from the two dimensional NOC scheme and, (C) SPH simulation representing the steady flow past the defence structure

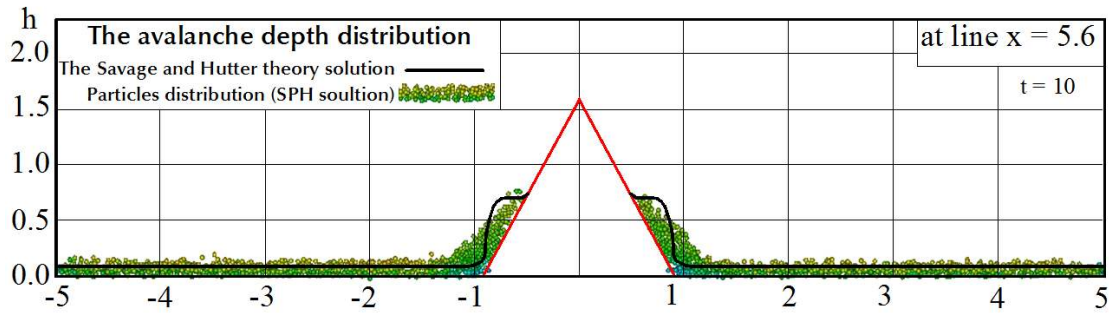


Fig 5.16 Cross section of the avalanche depth distribution along the line $x = 5.6$ through the top of the pyramid

5.6.4. Numerical Investigation of the Propagation of Shock Waves and Dead Zones in Rapid Flows of Granular Materials

When a thin surface avalanche of granular material flows around an obstacle or over a change in the bed topography usually shock waves, dead zones and particle-free regions formed. Understanding and modeling such features is of considerable practical interest in industrial processes, as well as for the design of defences to protect buildings, structures and people from snow avalanches, debris flows and rock falls. These types of flows are generated around a pyramidal obstacle, which is typical of some of the defensive structures in use today.

In this section, our three dimensional SPH model is applied to simulate the gravity granular flows down an inclined plane obstructed with two types of obstructions, Forward-facing pyramid and rearward-facing pyramid. The numerical results are then compared with experimental data, and numerical results obtained from quasi-two-dimensional flows model. The results got from this study indicate a good agreement in terms of formation of shock waves, dead zones and granular vacuum, and have shown that SPH could be a powerful method for simulating granular flows.

5.6.4.1. The model description

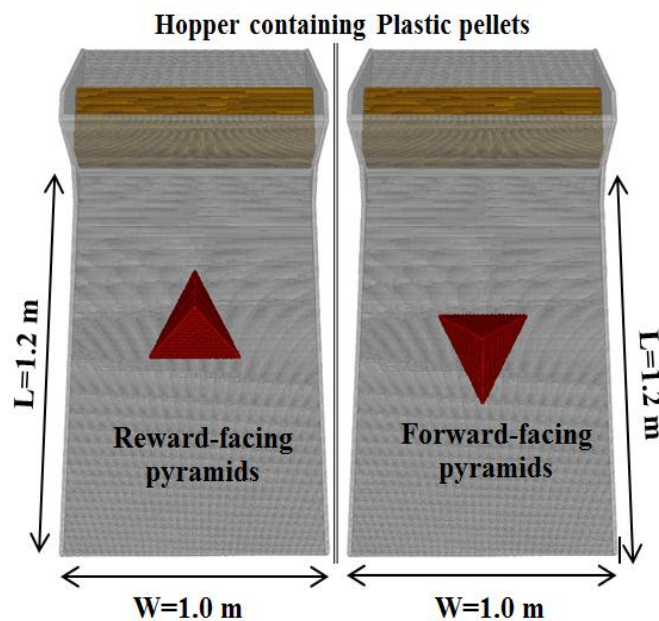


Fig 5.17 Schematic sketch of the granular avalanche experiment

A laboratory experiments were performed by Gray et al. (2003) similar to the experiments done by Yih-Chin T. (2000). The purpose of the new experiment is to simulate the granular flow past two types of obstacles. The first one is the forward-facing pyramids, which has been proposed to protect the Schneefernerhaus at the Zugspitze, Germany, against a large avalanche with a 100-year recurrence, that equals to a snow layer of 8 m depth moving down the mountain (Yih-Chin T. et al. 2000). The second obstacle is the rearward-facing pyramid, which represents defences structures with a blunt face facing upslope.

In the experiments, the mountain flank modeled as an inclined metallic plane 1 m wide and 1.2 m long, with inclination angle 42° and 34° in case of using forward-facing pyramid and rearward-facing pyramid; respectively. Plastic pellets of 2–3 mm in size, is released onto the plane from a hopper at the top of the inclined plane, as shown in **Fig. 5.17**.

5.6.4.2. Numerical simulations

Simulation of the granular flow avalanche was carried out using the proposed SPH model. The number of particles used to simulate the plastic pellets was 165000, with 0.002 m initial distance between particles which equals to the diameter size of the plastic pellets. The material parameters used in the calculation are illustrated in **Table 5.4**.

Table 5.4 Materials parameters

Parameter	Value
Density (kg/m^3)	$\rho = 890$
Young's modulus (MPa)	$E = 900$
Friction angle	$\phi = 38^\circ$
Passion ratio	$\nu = 0.42$

5.6.4.3. Results and analysis

Fig. 5.18 present a series of snapshots of the avalanche hitting the forward-facing pyramids, showing the particles positions and free-surface shape together with the velocity field at different times. The result obtained by the SPH method is compared with the experimental images and the computed boundary obtained from the quasi two dimensional model solutions by Gray et al. (2003). The time intervals between snapshots are equal to 1.27 non-dimensional units. When the particles released from the gate, the flow front starts to propagate uniformly, the flow was fast and thin. As soon as the flow hits the pyramid, a normal shock is formed at the pyramid top and extends on both sides of the flanks of the pyramid to consist an oblique shock at which the flow thickness increases.

The oblique shocks on both sides of the defence structure are clearly seen from the streamlines in the experiment, computed flow thickness from the quasi two dimensional model solutions, as well as the particle distribution in SPH results. Also, the particle-free region was formed, which shows that the protected zone is well described in the SPH results.

The SPH results show that the position of the deflected front is slightly further downslope than the undeflected front at $t = 2.55$ units, which is in a good agreement with the experiment and the results from the quasi two dimensional model solution. At $t = 6.37$ units the flow has reached to the steady state. From this comparison the results show that the current SPH model is sufficient to capture all the qualitative features of the flow, such as the formation of the oblique shocks, expansion waves and the granular vacuum on the lee-side of the pyramid.

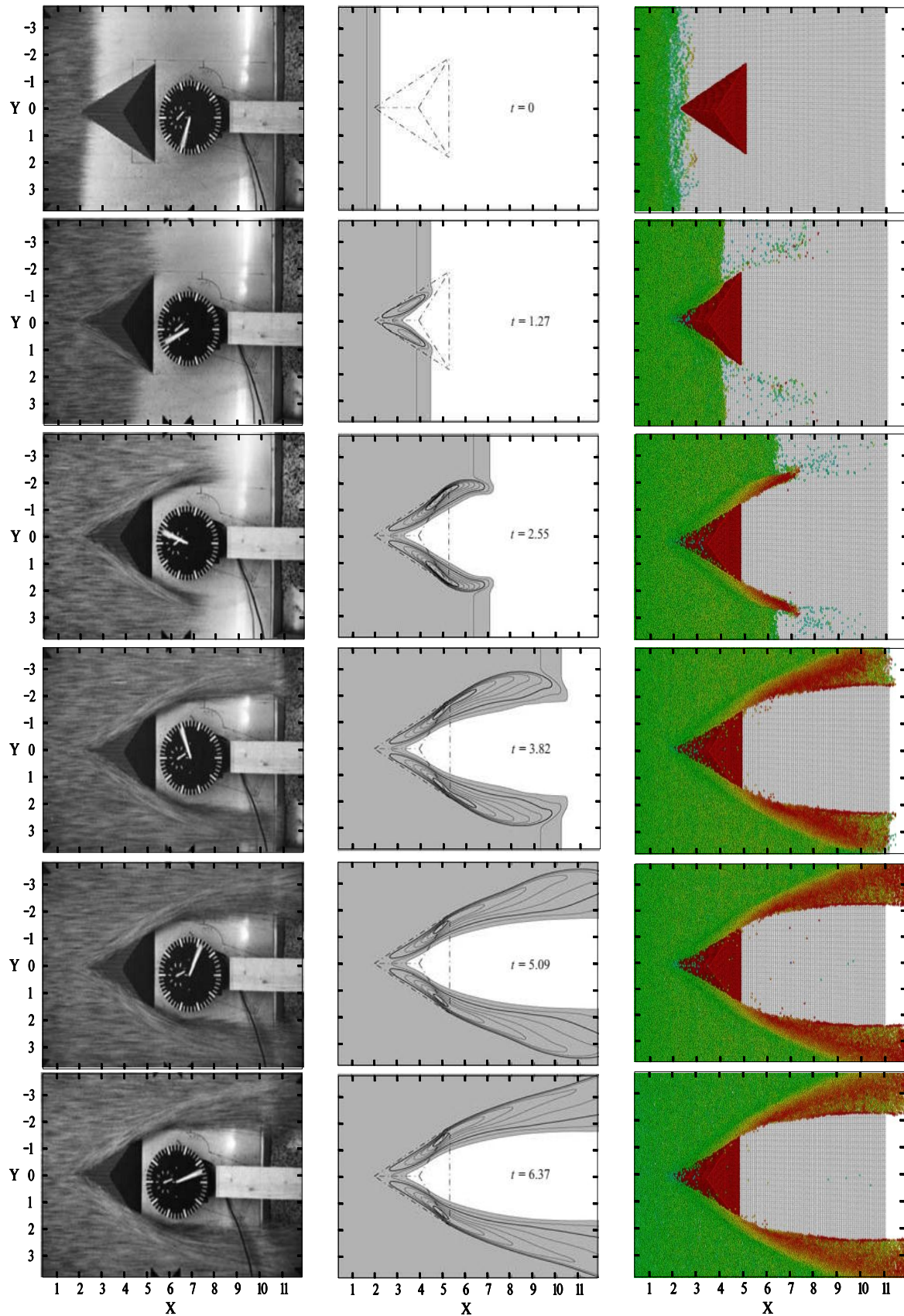


Fig 5.18 Comparison between (A) the experimental results, (B) numerical results obtained from the quasi-2d model solution and, (C) SPH simulation representing the steady flow past and around the Forward-facing pyramids at different time steps.

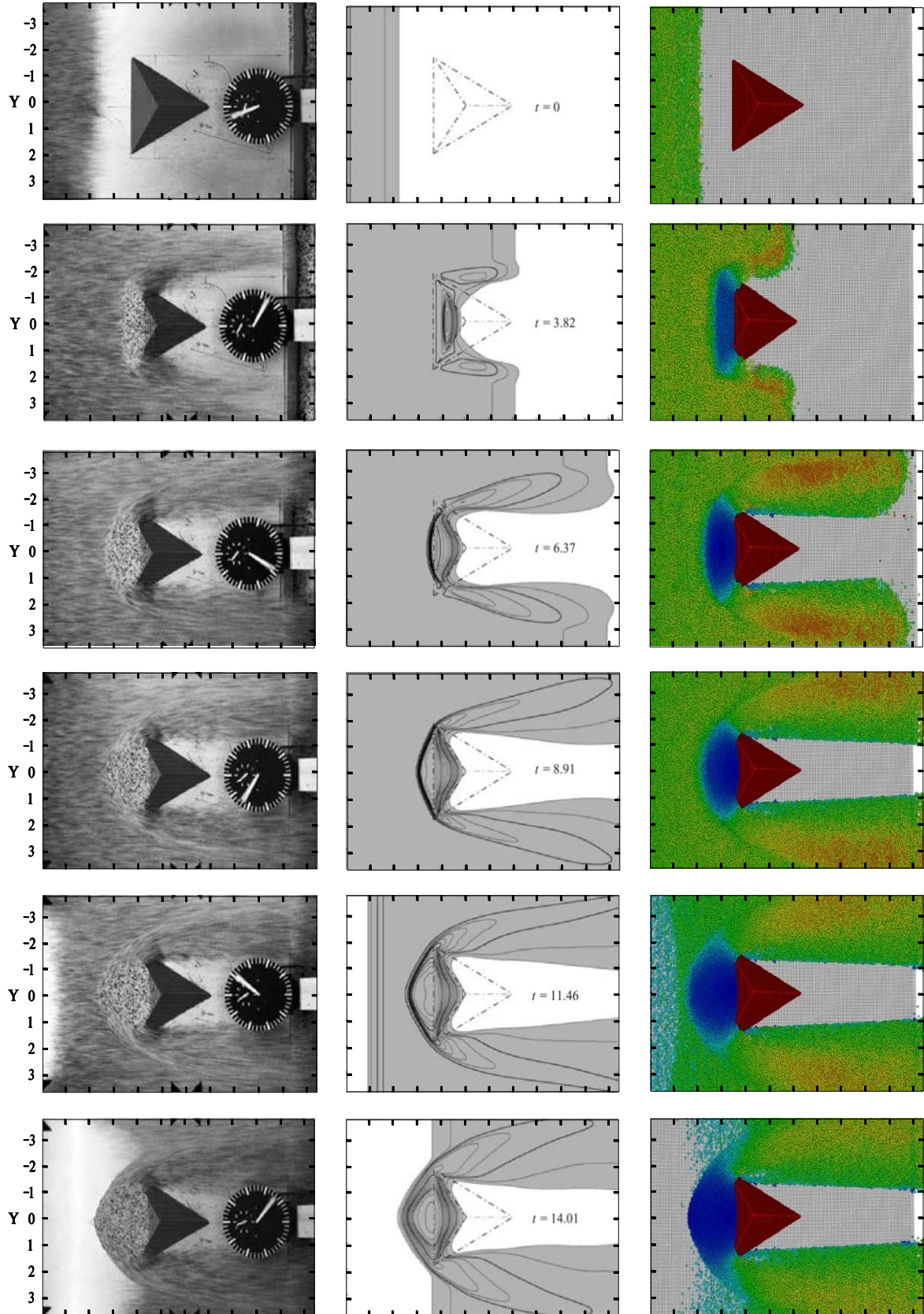


Fig 5.19 Comparison between (A) the experimental results, (B) numerical results obtained from the quasi-2d model solution and, (C) SPH simulation representing the steady flow past and around the rearward-facing pyramids at different time steps.

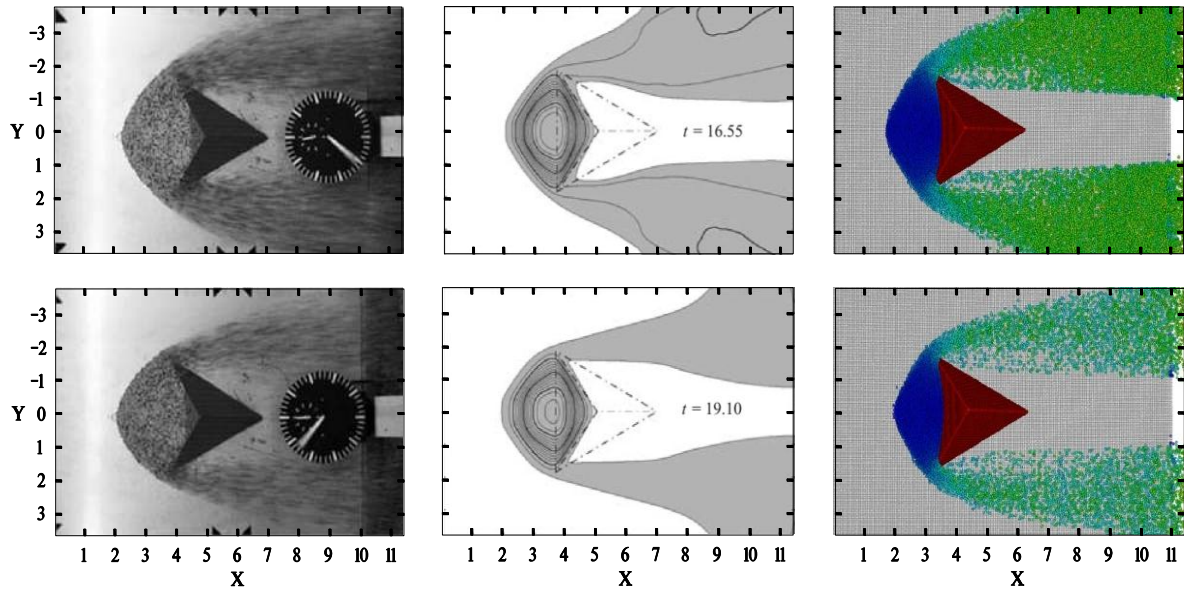


Fig 5.20 Conti-Comparison between (A) the experimental results, (B) numerical results obtained from the quasi-2d model solution and, (C) SPH simulation representing the steady flow past and around the rearward-facing pyramids at different time steps.

The model is also in very good quantitative agreement with the experiment, both in the position of the captured features and the time scale for their formation.

Figs.5.19 and **5.20** represents a sequence of numerical snapshots of the avalanching motion of a granular material particles hitting the reward-facing pyramids at different times and it is compared with the experimental images and the computed boundary obtained from the quasi two dimensional model solutions by Gray et al. (2003). When the flow first Collide with the front face of the pyramid the topography gradients are sufficient to bring the material to rest and form a thick stationary deposit, or dead zone.

With time the dead zone grows in size until it saturates, creating a detached shock upslope of the obstacle which deflects the flow into two streams. The width of these streams is greater than in the case of the forward-facing pyramid. The SPH simulation and the experiment are nevertheless in good qualitative and quantitative agreement with one another, indicating that the SPH model is sufficient to capture the formation of the dead zone. The granular vacuum appears in the downstream of the pyramid; however, it is much narrower and affords much less protected than the forward-facing pyramid.

From the above results, it is clear that the SPH method can well describe the properties of the flow around the tetrahedral and can quantitatively describe the protection region.

5.7. SUMMARY

A novel three dimensional computational model based on the SPH method has been developed for simulating the granular flow past different types of obstacles. The elastic–perfectly plastic model has been implemented in the SPH framework to model the granular materials. The present model was validated by the experiment on the collapse of 3D axisymmetric column of sand. A good agreement was observed between the numerical and experimental results.

Granular flow past three types of obstacle, a group of stake rows with different spacing, circular cylinders, and tetrahedral wedge have been numerically simulated using the present SPH model. The computational results were compared with experimental results and two existing numerical results to check the capabilities of the proposed model. The numerical results in the first case in terms of the final granular deposition shapes, spreading of the particles and the position of the leading edge are found to be in good agreements with the experimental results. Although the efficiency factor from the experimental results in all cases is slightly greater than the calculated values from the SPH results, though the error is less than 1 %.

Simulation of granular free-surface flow around a circular cylinder, and tetrahedral obstacle show that SPH method can capture and describe the formation of the bow shock, normal shock oblique shock around the obstacle, dead zones and can describe the protected area as observed in the experiments, different numerical solutions.

This study suggests that SPH could be a powerful method for solving problems dealing with granular materials subjected to large deformation and could be used to design real avalanche defences.

Chapter 6

SPH modeling of Fluid–Soil interactions (Scouring behind Seawall)

In 2011, Tohoku-Kanto earthquake, tsunami caused serious damage on the infrastructures. Soil scour and erosion behind the seawall had occurred during the overflow (return flow), and it may become one of the main reasons for the collapse of seawall. Fluid-Soil coupling simulation is desired for a systematic comprehension of the seawall collapse mechanism, and it may help to develop next disaster prevention method. In this chapter, a new numerical simulation tool for the Fluid-Soil interaction problem is developed as a fundamental study related to the soil scour and erosion. Water is modeled as a viscous fluid with weak compressibility and soil is modeled as an elastic–perfectly plastic material. The Mohr–Coulomb failure criterion is applied to describe the stress states of soil in the plastic flow regime. Interaction between soil and water is taken into account by means of pore water pressure and seepage force. First, the model was validated by simulating of the Louvain erosional dam-break experiment presented by Fraccarollo and Capart (2002). Finally, the model applied to simulate the return flow scouring experiment done by Yamamoto (2011). Numerical results obtained in this study have shown that SPH could be a valuable method for simulation of complex problem in soil mechanics.

6.1. INTRODUCTION

The interaction between water and soil poses problems in different areas of marine, geomechanics and hydraulic engineering. Numerical predictions for such interactions in the case of large deformations could provide useful knowledge for engineering practice and design. There are some traditional numerical methods for deformation and failure of geometries in the framework of continuum mechanics, such as finite element method, finite difference method and boundary element method. These methods have been successfully implemented. On the other hand, in the case of large deformation problems, the previous methods produce instabilities due to excessive distortion of a mesh.

In this chapter, the advantages of SPH will be exploited to simulate the soil–water interaction.

6.2. SPH MODEL FOR WATER

For a fluid like water, it is customary to model it as exactly incompressible. However, the approach in SPH is different; the real fluid is approximated by an artificial fluid which is more compressible than the real one, while still possessing a speed of sound which is much

larger than the flow speed, and which therefore has very small density fluctuation. The governing equations for fluid flow are the well-known Navier–Stokes equations, which in the Lagrangian description state the conservation of mass and momentum as follows:

$$\frac{D\rho}{Dt} = -\rho \frac{\partial v^\alpha}{\partial x^\alpha} \quad (6.1)$$

$$\frac{Dv^\alpha}{Dt} = \frac{1}{\rho} \left(\frac{\partial \sigma^{\alpha\beta}}{\partial x^\alpha} \right) + f^\alpha \quad (6.2)$$

where α and β denote the Cartesian components x , y and z with the Einstein convention applied to repeated indices; ρ is the density; v is velocity; $\sigma^{\alpha\beta}$ is stress tensor, f^α is the component of acceleration caused by external force, and D/Dt is material derivative.

The stress tensor, $\sigma^{\alpha\beta}$, normally consists of two parts: an isotropic pressure P and a viscous shear stress, which is proportional to the shear strain rate denoted by ε through the viscosity μ ,

$$\sigma^{\alpha\beta} = -P\delta^{\alpha\beta} + \mu\varepsilon^{\alpha\beta} \quad (6.3)$$

Where:

$$\varepsilon^{\alpha\beta} = \frac{\partial v^\alpha}{\partial x^\beta} + \frac{\partial v^\beta}{\partial x^\alpha} - \frac{2}{3} \left(\frac{\partial v^\gamma}{\partial x^\gamma} \right) \delta^{\alpha\beta} \quad (6.4)$$

Using the SPH concept discussed in chapter two, the system of partial differential equations (6.1) and (6.2) can be converted into the SPH formulations which will be used to solve the motion of fluid particles as follows:

$$\frac{D\rho_i}{Dt} = \sum_{j=1}^N m_j (v_i^\alpha - v_j^\alpha) \frac{\partial W_{ij}}{\partial x_i^\alpha} \quad (6.5)$$

$$\frac{Dv_i^\alpha}{Dt} = \sum_{j=1}^N m_j \left(\frac{\sigma_i^{\alpha\beta}}{\rho_i^2} + \frac{\sigma_j^{\alpha\beta}}{\rho_j^2} \right) \frac{\partial W_{ij}}{\partial x_i^\beta} + f^\alpha \quad (6.6)$$

Similarly, the SPH approximation of shear strain rate $\varepsilon_i^{\alpha\beta}$ for particle i is

$$\begin{aligned} \varepsilon_i^{\alpha\beta} = & \sum_{j=1}^N \frac{m_j}{\rho_j} (v_i^\alpha - v_j^\alpha) \frac{\partial W_{ij}}{\partial x_i^\beta} + \sum_{j=1}^N \frac{m_j}{\rho_j} (v_i^\beta - v_j^\beta) \frac{\partial W_{ij}}{\partial x_i^\alpha} \\ & - \left(\frac{2}{3} \sum_{j=1}^N \frac{m_j}{\rho_j} (v_i^\gamma - v_j^\gamma) \frac{\partial W_{ij}}{\partial x_i^\gamma} \right) \delta^{\alpha\beta} \end{aligned} \quad (6.7)$$

The final equation needed to solve the above Navier–Stokes equations for water is the “equation of state” which is used to estimate the pressure change of water

$$P = B \left[\left(\frac{\rho}{\rho_0} \right)^\lambda - 1 \right] \quad (6.8)$$

where λ is a constant ($=7$), ρ_0 is the reference density, B is a problem dependent parameter, which sets a limit for the maximum change of the density and will be calculated as

$$B = \frac{100 V_{type}^2 \rho_0}{\lambda}, \quad V_{type} = \sqrt{2 g H} \quad (6.9)$$

where V_{type} the typical speed of water and H is the depth of the water.

6.3. SPH MODEL FOR SOIL

Modeling the behavior of soil using the SPH method is similar to that of water. The SPH form of conservation equations (6.1) and (6.2) are still used to estimate the density and motion of soil particles. The key difference between these two models is the calculation of the stress tensor appearing in Eq. (22) in which the pressure and stress–strain relationship of soil are calculated differently from those of water; soil is assumed herein to be an elastic–plastic material. The stress tensor of soil is made up of two parts: isotropic pressure P and deviatoric shear stress S ,

$$\sigma^{\alpha\beta} = -P\delta^{\alpha\beta} + S^{\alpha\beta} \quad (6.10)$$

Since soil is assumed to have elastic behavior (Bui and others, 2007; Yaidel and others 2012), so the pressure equation of soil will obey Hooke’s law, as follows,

$$P = -K \frac{\Delta V}{V} = K \left(\frac{\rho}{\rho_0} - 1 \right) \quad (6.11)$$

where K is bulk modulus; $\Delta V/V$ is the volumetric strain; and ρ_0 is the initial density of soil. The rate of change of deviatoric shear stress dS/dt can be calculated using shear modulus, μ , using the Jaumann rate from the following constitutive equation,

$$\frac{dS^{\alpha\beta}}{dt} = 2\mu \left(\varepsilon^{\alpha\beta} - \frac{1}{3} \varepsilon^{\gamma\gamma} \right) + S^{\alpha\gamma} \omega^{\beta\gamma} + \omega^{\gamma\beta} S^{\alpha\gamma} \quad (6.12)$$

where $\varepsilon^{\gamma\gamma} = \varepsilon^{xx} + \varepsilon^{yy} + \varepsilon^{zz}$, is the strain rate tensor and $\omega^{\gamma\beta}$ is the rotation rate tensor. It can be defined by,

$$\varepsilon^{\alpha\beta} = \frac{1}{2} \left(\frac{\partial v^\alpha}{\partial x^\beta} + \frac{\partial v^\beta}{\partial x^\alpha} \right) \quad (6.13)$$

$$\omega^{\alpha\beta} = \frac{1}{2} \left(\frac{\partial v^\alpha}{\partial x^\beta} - \frac{\partial v^\beta}{\partial x^\alpha} \right) \quad (6.14)$$

Using the concept of the SPH approximation the system of partial differential equations (6.1) and (6.2) can be converted into the SPH formulations which will be used to solve the motion of soil particles as follows:

$$\frac{D\rho_i}{Dt} = \sum_{j=1}^N m_j (v_i^\alpha - v_j^\alpha) \frac{\partial W_{ij}}{\partial x_i^\alpha} \quad (6.15)$$

$$\frac{Dv_i^\alpha}{Dt} = \sum_{j=1}^N m_j \left(\frac{\sigma_i^{\alpha\beta}}{\rho_i^2} + \frac{\sigma_j^{\alpha\beta}}{\rho_j^2} \right) \frac{\partial W_{ij}}{\partial x_i^\beta} + f^\alpha \quad (6.16)$$

Similarly, the SPH approximation of the strain rate tensor and the rotation rate tensor for particle i can be expressed as following:

$$\varepsilon_i^{\alpha\beta} = \frac{1}{2} \sum_{j=1}^N \left(\frac{m_j}{\rho_j} (v_i^\alpha - v_j^\alpha) \frac{\partial W_{ij}}{\partial x_i^\beta} + \frac{m_j}{\rho_j} (v_i^\beta - v_j^\beta) \frac{\partial W_{ij}}{\partial x_i^\alpha} \right) \quad (6.17)$$

$$\omega_i^{\alpha\beta} = \frac{1}{2} \sum_{j=1}^N \left(\frac{m_j}{\rho_j} (v_i^\alpha - v_j^\alpha) \frac{\partial W_{ij}}{\partial x_i^\beta} - \frac{m_j}{\rho_j} (v_i^\beta - v_j^\beta) \frac{\partial W_{ij}}{\partial x_i^\alpha} \right) \quad (6.18)$$

By combining Equations (6.11), (6.16) and (6.17), the deviatoric shear stress components can be calculated. Then, they are compared with the maximum shear stress ($S_f = c + P \tan\phi$) in the plastic flow regime of the soil, which determined by the Mohr–Coulomb failure criterion. Here c is soil cohesion and ϕ is the angle of internal friction of the soil.

6.4. SOIL–WATER INTERACTION MODELING

Modeling of soil and water in the framework of the smoothed particle hydrodynamics method has been presented in the previous sections, however, these models only allow to simulate one-phase flow. In order to simulate the soil– water interaction, which consists of two-phase flows, it is necessary to derive an equation to describe the interaction between soil and water phases, as follows.

When groundwater is seeping through the pores of a soil, viscous friction will produce drag on soil particles in the direction of water flow, so-called seepage force. This seepage force acts on the soil particles in addition to the gravitational force, and will be introduced into the momentum equations for soil and water as an external force according to the following model equation based on the Darcy's law:

$$f_{seepage} = \gamma_w n \frac{(v_{water} - v_{soil})}{k} \quad (6.19)$$

where γ_w is the unit weight of water; n is the porosity; and k is the soil permeability.

As saturated soil consists of soil and water mixed together while standard SPH models only handle one phase problem, it is necessary to develop a saturated soil model using in SPH simulation. This saturated soil model will be described as follows:

We assumed that the saturated soil domain in SPH can be divided into two separate phases, which are water phase and soil phase. The motion of SPH particles on each phase is solved separately using its own SPH governing equations, which are SPH for soil and SPH for water. These two-phases are then superimposed and the interaction between two-phases will be taken into account through the seepage force, which is introduced into the momentum equation as mentioned before. In addition, the water pressure is also allowed to contribute to the soil pressure during the overlapping procedure. This allows us to simulate the pore water pressure, which always exists in natural saturated soil. Accordingly, the momentum equations for saturated soil can be summarized as follows,

Momentum equation for soil phase

$$\begin{aligned} \frac{Dv_i^\alpha}{Dt} = & \sum_{j=1}^N m_j \left(\frac{s_i^{\alpha\beta}}{\rho_i^2} + \frac{s_j^{\alpha\beta}}{\rho_j^2} \right) \frac{\partial W_{ij}}{\partial x_i^\alpha} - \sum_{j=1}^N m_j \left(\frac{P_i}{\rho_i^2} + \frac{P_j}{\rho_j^2} \right) \frac{\partial W_{ij}}{\partial x_i^\alpha} + f_i^\alpha - \sum_{a=1}^N m_a \frac{P_a}{\rho_i \rho_a} \frac{\partial W_{ia}}{\partial x_i^\alpha} \\ & + \sum_{a=1}^N m_a \frac{f_{ia}^{seepage}}{\rho_i \rho_a} W_{ia} \end{aligned} \quad (6.20)$$

Momentum equation for Water phase

$$\begin{aligned} \frac{Dv_i^\alpha}{Dt} = & \sum_{b=1}^N m_b \left(\frac{\tau_a^{\alpha\beta}}{\rho_a^2} + \frac{\tau_b^{\alpha\beta}}{\rho_b^2} \right) \frac{\partial W_{ab}}{\partial x_a^\alpha} - \sum_{b=1}^N m_b \left(\frac{P_a}{\rho_a^2} + \frac{P_b}{\rho_b^2} \right) \frac{\partial W_{ab}}{\partial x_a^\alpha} + f_a^\alpha \\ & - \sum_{i=1}^N m_i \frac{f_{ia}^{seepage}}{\rho_i \rho_a} W_{ia} \end{aligned} \quad (6.21)$$

where the subscripts i and j represent for soil particles while a and b are used for water particles. It is clear that these momentum equations of saturated soil are different from that of single phase, equation (6.16). The presence of the seepage force in equations (6.19), (6.20), and the contribution of pressure from water to soil in equation (6.19) make them possible to simulate the effect of seepage force and pore water pressure in the saturated soil model, as a result the interaction between soil and water could be simulated through SPH.

In order to damp out the unphysical stress fluctuation and to prevent shock waves and the penetration of particles through the boundaries, an artificial viscosity has been employed to the pressure term in the momentum equation. The most widely used type is proposed by Monaghan and Lattanzio (1985), and specified as follows

$$\pi_{ij} = \begin{cases} \frac{-\alpha \bar{c}_{ij} \phi_{ij} + \beta \phi_{ij}^2}{\bar{\rho}_{ij}} & v_{ij} \cdot x_{ij} < 0 \\ 0 & v_{ij} \cdot x_{ij} \geq 0 \end{cases} \quad (6.22)$$

in which α and β are constants and are taken 0.01, 1.0 respectively, and c represent the speed of sound. As well as having beneficial effects, artificial viscosity can also introduce unwanted numerical defects in some cases, among which the excess dissipation and false shearing torque in rotating flows (Dalrymple, and Knio, 2001).

The momentum equations for saturated soil after introducing the artificial viscosity to the pressure term are:

Momentum equation for soil phase:

$$\begin{aligned} \frac{Dv_i^\alpha}{Dt} = & \sum_{j=1}^N m_j \left(\frac{s_i^{\alpha\beta}}{\rho_i^2} + \frac{s_j^{\alpha\beta}}{\rho_j^2} \right) \frac{\partial W_{ij}}{\partial x_i^\alpha} - \sum_{j=1}^N m_j \left(\frac{P_i}{\rho_i^2} + \frac{P_j}{\rho_j^2} + \pi_{ij} \right) \frac{\partial W_{ij}}{\partial x_i^\alpha} + f_i^\alpha \\ & - \sum_{a=1}^N m_a \frac{P_a}{\rho_i \rho_a} \frac{\partial W_{ia}}{\partial x_i^\alpha} + \sum_{a=1}^N m_a \frac{f_{ia}^{seepage}}{\rho_i \rho_a} W_{ia} \end{aligned} \quad (6.23)$$

Momentum equation for Water phase:

$$\begin{aligned} \frac{Dv_i^\alpha}{Dt} = & \sum_{b=1}^N m_b \left(\frac{\tau_a^{\alpha\beta}}{\rho_a^2} + \frac{\tau_b^{\alpha\beta}}{\rho_b^2} \right) \frac{\partial W_{ab}}{\partial x_a^\alpha} - \sum_{b=1}^N m_b \left(\frac{P_a}{\rho_a^2} + \frac{P_b}{\rho_b^2} + \pi_{ij} \right) \frac{\partial W_{ab}}{\partial x_a^\alpha} + f_a^\alpha \\ & - \sum_{i=1}^N m_i \frac{f_{ia}^{seepage}}{\rho_i \rho_a} W_{ia} \end{aligned} \quad (6.24)$$

6.5. LOUVAIN EROSIONAL DAM BREAK (TEST CASE)

To validate the proposed SPH model for soil–water interaction, in this section it is applied to the benchmark test of the Louvain erosional dam break experiment presented by Fraccarollo and Capart (2002). The collapse of the water column induces a surge leading to erosions of the soil.

Fig.6.1 presents the schematic diagram for the Louvain erosional 3D-dam break, which presented by Fraccarollo and Capart (2002). A water column with a width $L_w = 1$ m, and height $H_w = 0.1$ m is situated over the soil bed with width $L_s = 2$ m, and height $H_s = 0.6$ m. The density ratio between soil density ρ_s , and water density ρ_w is taken as $\rho_s/\rho_w = 1.54$.

The dry soil is modeled by one type of particles with uniform material properties. These particles have the following properties: Young's modulus $E = 150$ MPa and Poisson's ratio $\nu = 0.3$. The water particles have density of $\rho = 1.0$ g/cm³ and viscosity $\mu = 10^{-3}$ Ns/m². There are a total of 4173 and 2420 particles representing the soil and water particles, respectively. A particle spacing equal 0.005 m is used for both the water and the soil materials.

To validate the model, the computed free surfaces and bed evolution profiles by the SPH model are compared with the experimental data (Fraccarollo and Capart 2002) in **Fig. 6.2** at four different time instants after the dam break, i.e. $t = 0.25$ s, 0.5 s, 0.75 s, and 1.0 s; respectively.

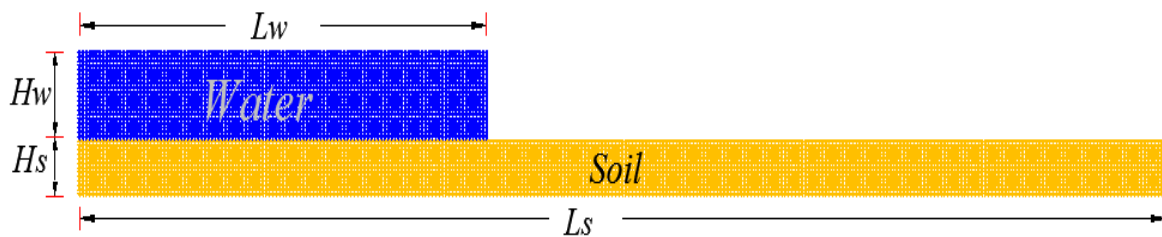


Fig 6.1 Sketch of the Louvain dambreak experiment's initial set-up

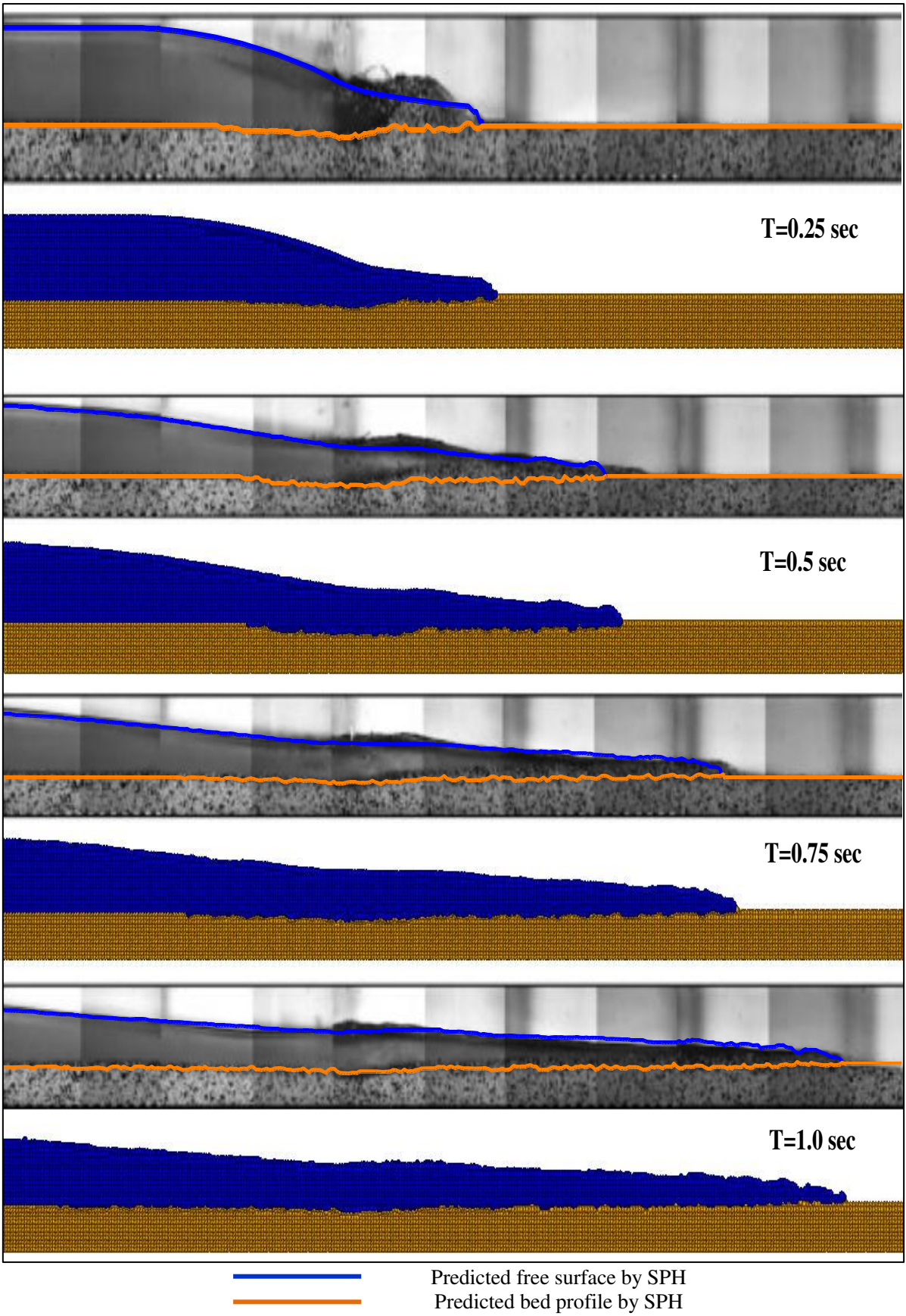


Fig 6.2 Snapshots of the Louvain experiments ($t=0.25, 0.5, 0.75, 1.0$ Sec) compared with SPH simulations

The comparisons in **Fig. 6.2** indicated that the SPH computed free surface profiles match the measured interface-contours quite well. Deviations, both in the interfaces and the surge front, are seen in the earlier time instant $t = 0.25$ s. They are attributed to the effects being related to experimental details – such as the opening of a gate – that are not captured by the simulation. The overall agreement is nonetheless satisfactory, especially for $t \geq 0.5$ s.

As for the sediment bed profiles, the SPH model well predicted the maximum sediment layer height, but there exist some discrepancies in the bed evolution profile and the SPH seemed to under-predict the sediment bed movement.

6.6. RESULTS AND DISCUSSIONS

In this section, SPH will be applied to soil scour and erosion behind the seawall had occurred during the overflow (return flow), and it may become one of the main reasons for the collapse of seawall. Yamamoto et.al, (2011), conducts a laboratory experiment to investigate this phenomenon.

6.6.1. Scour prediction in front of seawall caused by the return flow

6.6.1.1. Model description

Fig. 6.3 shows a schematic sketch illustrating the dimensions of the experiment of the hydraulic experiment done by Yamamoto. This experiment is a return flow scouring experiment and its scale is shown below

Here, gradient of sandy beach and slope is one-fifteenth, and there is a seawall at the front of sandy beach. There is a velocity meter away from the seawall by 6cm.

6.6.1.2. Numerical simulations

As for soil parameters, the density ratio between soil density ρ_s and water density ρ_w is taken as $\rho_s / \rho_w = 1.6$, Young's modulus $E = 150$ Mpa, passion ratio $\nu = 0.3$. The internal angle and cohesion are taken as $\varphi = 30^\circ$ and $c = 30$ kPa.

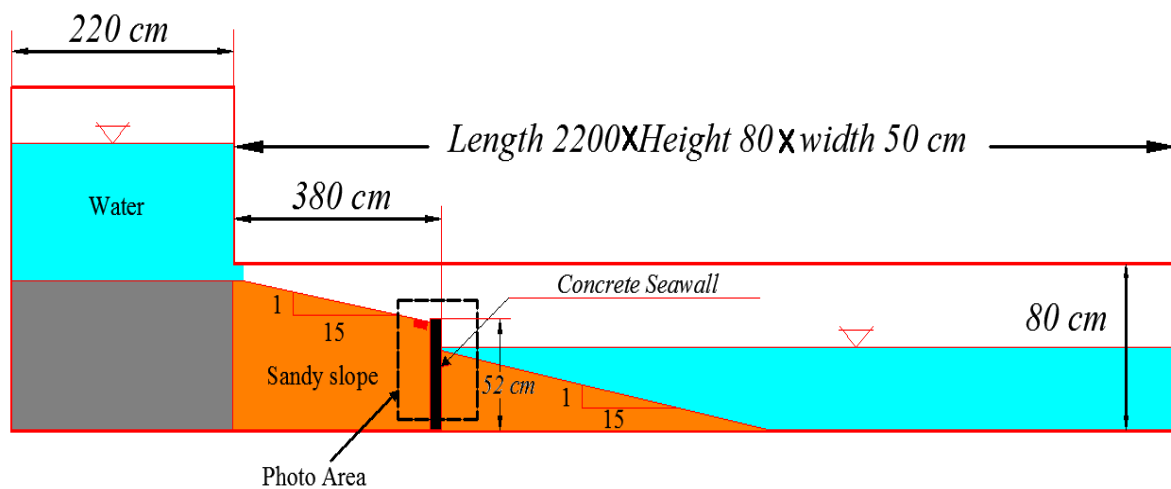


Fig 6.3 Schematic diagram for hydraulic experiment

6.6.1.3. Results and analysis

Fig. 6.4 shows a comparison between the experimental snapshot and numerical results in the term of the particles distribution and the scouring shape before and after formatting the scouring hole. From these comparisons, we can see that the predicted express soil erosion and scouring behaviors show a good agreement with the hydraulic experiment test. However, the shape of soil erosion is slightly different. As for the reason, various factors are taken into account. One of them is not considered permeability of soil.

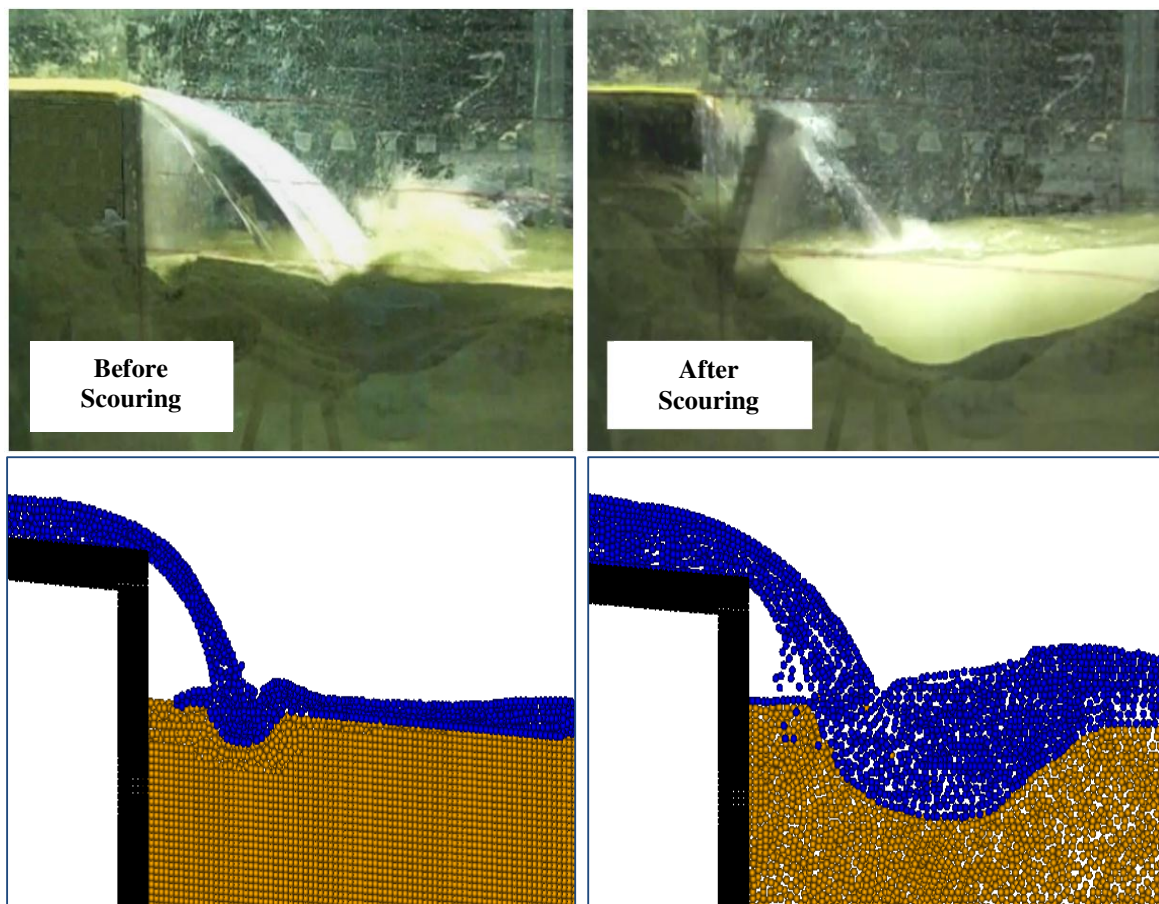


Fig 6.4 Comparison between experiment and analysis result

6.7. SUMMARY

The development of an improved smoothed particle hydrodynamics to simulate the behavior of soil–water interaction has been described through this chapter. Water was modeled as a viscous fluid with week compressibility while the soil was modeled as an elastic–perfectly plastic material. Interaction between soil and water was modeled by means of pore water pressure and seepage force. Simulation tests of the Louvain erosional dam-break experiment presented has been presented. The results have shown that the extremely large deformation and failure of soil can be handled in SPH without any difficulties.

The model used to simulate the experiment performed by Yamamoto (2011), to evaluate the scour in the front of a coastal seawall by the backflow of the tsunami. It was confirmed that the SPH method can express soil erosion and scouring. However, its analysis result is good

from a qualitative perspective, but not so good from quantitative one. Advantages of the method are its robustness, conceptual simplicity, relative ease of incorporating new physics, and especially its potential to handle large deformation and failure.

Chapter 7

Conclusions and future work

7.1. CONCLUSIONS

The thesis reports on the development and application of a Smoothed-Particle-Hydrodynamics method to simulate various phenomena in the science of computational fluid dynamic focusing on geo-disasters problems in order to establish effective prediction methods for such events could be used to design real protection structures.

Concerning the physical modeling, both, the water and soil phase are treated by a weakly compressible SPH model using Tait's equation for pressure evaluations. Water is modeled as a Newtonian fluid with a constant molecular viscosity. The soil is modeled as an elastic–perfectly plastic material. The Mohr–Coulomb failure criterion is applied to describe the stress states of soil in the plastic flow regime.

We developed a Two-dimensional SPH model to simulate free surface flow problems, and we used it to simulate three benchmark tests, (collapse of a water column with a rigid obstacle, and dam break on a wet bed). The simulation results were compared with experimental data and the solutions of Moving Particles Semi-implicate method. The comparison shows a good agreement and states that our SPH code could capture the water free surface shape precisely. The model is then extended to be Three- dimensional and used to solve the same two benchmark tests. We get good results in terms of particles spreading and the shape of free surface.

A novel non-Newtonian three-dimensional SPH model was developed to simulate real snow avalanches mechanisms. The snow was considered as a Bingham fluid and the snow viscosity was calculated based on the Bingham constitutive model, on the basis of Coulomb's failure criterion. An equivalent Newtonian viscosity is calculated to express the Bingham viscosity into Navier-Stokes equations. Model validation was performed by simulating the movement of an unsteady mudflow released from a reservoir of a finite size onto a steep channel. The results show a good agreement between our models and the experimental results, indicating that this numerical method can be used for practical simulation of non- Newtonian fluid. A small scale snow avalanche experiment with different types of obstacles was simulated using the present refined SPH code. Numerical results showed that, in the most cases, good agreements were found by the means of leading-edge position and the travel length.

Furthermore, successfully, the elastic–perfectly plastic model has been implemented in the SPH to develop three-dimensional SPH code to simulate the gravity granular flow past different types of obstacles. The model was validated by the experiment on the collapse of 3D axisymmetric column of sand and a good agreement was observed. The numerical results for the granular flows past a group of stake rows with different spacing in terms of the final granular deposition shapes, spreading of the particles and the position of the leading edge is found to be in good agreements with the experimental results. Although the efficiency factor from the experimental results in all cases is slightly greater than the calculated from the SPH results, the error is less than 1 %. Simulations of granular free-surface flows around a circular cylinder, and tetrahedral obstacle show that the present SPH model can capture and describe the formation of the bow shock, normal shock, and oblique shock around the obstacle. It also succeeded in describing the protected area as observed from the comparison.

Finally, soil–water interaction is presented in order to simulate the soil scour and erosion behind the seawall had occurred during the overflow (return flow). The interaction between soil and water was done by adding the seepage force and pore water pressure terms to the momentum equation. It was confirmed that the SPH method can express soil erosion and scouring. However, its analysis result is good from a qualitative perspective, but not so good from quantitative one.

The thesis demonstrates that SPH provides strong advantages over alternative mesh based methods related to large relative motions, multiple phases and continua, free surface flows and rapid granular flow. Such phenomena are not only relevant to the primarily addressed field of establishment structures for protection against geo-disasters, but occur in very similar characteristics in many other hydraulic engineering disciplines. The present procedure therefore provides the potential of being extensively used and to play an important role in a wide range of applications.

7.2. FUTURE WORK

Although we succeeded to simulate many phenomena with different cases using our developed model, this model has the following limitation. In all the simulated cases, the flow (Fluid or Soil) starts from stationary conditions and moves under the gravity force. This model cannot deal with problems, which need inflow/outflow boundary conditions, such as, open channel flow, and flood inundation owing to rapidly varying flow, such as tsunamis. These are some suggestions for the future work:

Firstly, Adding the closed boundary conditions to the current model by applying the modified virtual boundary (MVB) method to maintain the zeroth moment of the kernel function as closely as possible to unity, (a property referred to as zero-consistency), for particles close to solid boundaries. (Vacondio et. al., (2011a) *International Journal for Numerical Methods in Fluids*). The main advantage of the MVB is that complex domains and arbitrary bathymetries or boundaries with angles can be easily reproduced.

Secondly, Incorporation of open boundary conditions to the current model will be by combining the ghost particle technique which was introduced for solid wall boundary conditions with the mirror particle technique (Morris et al., 1997, *J. Comput. Phys*; Libersky, et. al., 1993, *J. Comput. Phys*) to produce open boundary conditions. This feature will allow us to transmit incident waves across the boundary without any reflection. Furthermore, different combinations of velocity and pressure boundary conditions will be possible. Moreover coupling the conventional Euler 2D model and the improvement SPH model to develop a novel Hybrid SPH model in order to, get a precise prediction of tsunami hazard maps for a wide area as well as detailed information around tsunami hot spots.

APPENDIX A- PUBLICATION LISTS

Peer-Reviewed Papers

1. Abdelrazek A.M., Kimura I., and Shimizu Y.: Comparison between SPH and MPS Methods for Numerical Simulations of Free Surface Flow Problems, Journal of Japan Society of Civil Engineers, Ser. B1 (Hydraulic Engineering), Vol.70 No. (4), pp. I_67-I_72 (2014). **DOI: 10.2208/jscejhe.70.I_67**
2. Abdelrazek A.M., Kimura I., and Shimizu Y. : Numerical Simulation of Snow Avalanches as a Bingham Fluid Flow Using SPH method, River Flow 2014, pp. 1581-1587, (2014). **DOI: 10.1201/b17133-210**
3. Abdelrazek A.M., Kimura I., and Shimizu Y. : Numerical simulation of a small-scale snow avalanche tests using non-Newtonian SPH model, Journal of Japan Society of Civil Engineers, Ser. A2 (Applied Mechanics (AM)) Vol. 70, No.2, pp. I_681-I_690, (2014). **DOI: 10.2208/jscejam.70.I_681**
4. Abdelrazek A.M., Kimura I., and Shimizu Y. : Numerical Simulation of Granular Flow Past Simple Obstacles using the SPH Method, Journal of Japan Society of Civil Engineers, Ser. B1 (Hydraulic Engineering), Vol.71, No.4, pp. I_199-I_204, (2015). **<http://ci.nii.ac.jp/naid/40020432389>**
5. Abdelrazek A.M., Kimura I., and Shimizu Y.: Numerical Simulation of Granular Flow Past Different types Obstacles using the SPH Method, Journal of Glaciology, (2015). **(Revised and resubmitted).**
6. Abdelrazek A.M., Kimura I., and Shimizu Y. : Numerical Investigation of the Propagation of Shock Waves and Dead Zones in Rapid Flows of Granular Materials using SPH Method, Journal of Japan Society of Civil Engineers, Ser. A2 (Applied Mechanics (AM)), (2015). **(Submitted).**

Presentations on Conferences (as participant)

7. Abdelrazek A.M., Kimura I., and Shimizu Y., Comparison between SPH and MPS Methods for Numerical Simulations of Free Surface Flow Problems. The 58th Conference on Hydraulic Engineering, March 4-6, 2014, Kobe University, Kobe, Japan.
8. Abdelrazek A.M., Kimura I., and Shimizu Y. 2014. : Numerical simulation of a small-scale snow avalanche tests using non-Newtonian SPH model. The 17th Applied Mechanics Symposium, May 10-11, 2014, University of the Ryukyus, Okinawa, Japan.
9. Abdelrazek A.M., Kimura I., and Shimizu Y. 2014. : Numerical Simulation of Snow Avalanches as a Bingham Fluid Flow Using SPH method. The 7th River Flow 2014, September 3-5, 2014, Lausanne, Switzerland.
10. Abdelrazek A.M., Kimura I., and Shimizu Y. 2015. : Numerical Simulation of Granular Flow Past Simple Obstacles using the SPH Method. The 59th Conference on Hydraulic Engineering, March 10-12, 2015, Waseda University, Tokyo, Japan.
11. Abdelrazek A.M., Kimura I., and Shimizu Y. 2015. : Numerical Investigation of the Propagation of Shock Waves and Dead Zones in Rapid Flows of Granular Materials using SPH Method. The 18th Applied Mechanics Symposium, May 10-11, 2015, Kanazawa University, Ishikawa, Japan.
12. Abdelrazek A.M., Kimura I., and Shimizu Y. 2015. : Simulation of rapid free-surface granular flows around a circular cylinder using the SPH method. The 9th Symposium on River, Coastal and Estuarine Morphodynamics, RCEM 2015, August 30 to September 3, Iquitos City, Peru **(Accepted).**

13. Abdelrazek A.M., Kimura I., and Shimizu Y.: Two-phase numerical simulation of scour due to free fall of water jet using WCSPH method, The 11th International Symposium on Ecohydraulics, ISE2016, February7-12, Melbourne, Australia (**Accepted**).

REFERENCES

- 1) Abdelrazek, A.M., Kimura, I., and Shimizu, Y.: Numerical Simulation of Snow Avalanches as a Bingham Fluid Flow Using SPH method, *River Flow 2014*, 1581-1587, 2014.
- 2) Abdelrazek, A.M., Kimura, I., and Shimizu, Y.: Comparison between SPH and MPS Methods for Numerical Simulations of Free Surface Flow Problems, *Journal of Japan Society of Civil Engineers, Ser. B1 (Hydraulic Engineering)*, 70 (4), I_67-I_72, 2014.
- 3) Abdelrazek, A.M., Kimura, I., and Shimizu, Y. : Numerical simulation of a small-scale snow avalanche tests using non-Newtonian SPH model, *Journal of Japan Society of Civil Engineers, Ser. A2 (Applied Mechanics (AM))*, 70 (2), I_681-I_690, 2014.
- 4) Abdelrazek, A.M., Kimura, I., and Shimizu, Y. : Numerical Simulation of Granular Flow Past Simple Obstacles using the SPH Method, *Journal of Japan Society of Civil Engineers, Ser. B1 (Hydraulic Engineering)*, 70 (4), I_199-I_204, 2015.
- 5) Abdelrazek, A.M., Kimura, I., and Shimizu, Y.: Numerical Simulation of Granular Flow Past Different types Obstacles using the SPH Method, *Journal of Glaciology*, 2015. **(Revised and resubmitted)**.
- 6) Abdelrazek, A.M., Kimura, I., and Shimizu, Y. : Numerical Investigation of the Propagation of Shock Waves and Dead Zones in Rapid Flows of Granular Materials using SPH Method, *Journal of Japan Society of Civil Engineers, Ser. A2 (Applied Mechanics (AM))*, 2015. **(Submitted)**.
- 7) Amicarelli, A., Marongiu, J-C., Leboeuf, F., Leduc, J., Neuhauser, M., Fang, L., and Caro, J.: SPH truncation error in estimating a 3D derivative. *Int. J. Numer. Meth. Engng.*, 87: 677–700, 2011.
- 8) Armstrong, B.R., Williams, K. and Armstrong, R.L.: The avalanche book. *Fulcrum Publishing*, 1992.
- 9) Benson, D. J.: Computational methods in Lagrangian and Eulerian hydrocodes, *Computer Methods in Applied Mechanics and Engineering*, 99,235-394, 1992.
- 10) Benz, W.: Smoothed particle hydrodynamics: a review, In *Numerical Modeling of Non-linear Stellar Pulsation: Problems and Prospects*, Kluwer Academic, Boston, 1990.
- 11) Biot, M.A.: Theory of propagation of elastic waves in a fluid saturated porous solid. I. low frequency range. *J Acoust Soc Am*, 28,168–78, 1956.
- 12) Bui, H. H., Sako, K., and Fukagawa, R.: Numerical simulation of soil–water interaction using smoothed particle hydrodynamics (SPH) method. *Journal of Terramechanics*, 44, 339–346, 2007.
- 13) Bui, H. H., Fukagawa, R., Sako, K. and Ohno, S.: Lagrangian meshfree particles method (SPH) for large deformation and failure flows of geomaterial using elastic–plastic soil constitutive model. *Int. J. Numer. Anal. Meth. Geomech.*, 32 (12), 1537–1570, 2008.
- 14) Bui, H. H., Fukagawa, R., Sako, K., and Wells, J. C.: Slope stability analysis and discontinuous slope failure simulation by elasto-plastic smoothed particle hydrodynamics (SPH). *Géotechnique*, 61 (7), 565 –574, 2010.
- 15) Chen, J. K., Beraun, J. E., and Carney, T. C.: A corrective smoothed particle method for boundary value problems in heat conduction, *Computer Methods in Applied Mechanics and Engineering*, 46:231-252, 1999.
- 16) Chen, W., and Qiu, T.: Numerical Simulations for Large Deformation of Granular Materials Using Smoothed Particle Hydrodynamics Method. *Int. J. Geomech.*, 12(2), 127–135, 2012.
- 17) Cui, X., Gray, J. M. N. T., and Johannesson, T.: Deflecting dams and the formation of oblique shocks in snow avalanches at Flateyri, Iceland. *Journal of Geophysical Research-earth Surface*, 112, F04012, 2007.
- 18) Cui, X., and Gray, J. M. N. T.: Gravity-driven granular free-surface flow around a circular

- cylinder. *Journal of Fluid Mechanics*, 720, 314-337, 2013.
- 19) Cummins, S. J., and Rudman, M.: A SPH projection method, *J.Comput.Phys.*, Vol.152, pp.584–607, 1999.
 - 20) Dalrymple, R.A., and Knio, O.: SPH modelling of water waves, *Proc. Coastal Dynamics*, 779-787, Sweden, 2001.
 - 21) Faug, T., Beguin, R., and Benoit, C.: Mean Steady Granular Force on a Wall Over-flowed by Free-surface Gravity-driven Dense Flows. *Physical Review E* 80, 021305, 2009.
 - 22) Flebbe, O., Muenzel, S., Herold, H., Riffert, H., and Ruder, H.: Smoothed Particle Hydrodynamics: Physical Viscosity and the Simulation of Accretion Disks, *The Astrophysical Journal*, 431, 2, pp. 754-760, 1994.
 - 23) Fraccarollo, L., and Capart, H.: Riemann wave description of erosional dam-break flows. *J. Fluid Mech.* 461, 183–228, 2002.
 - 24) Fries, T.P., and Matthies, H.G.: A Stabilized and Coupled Meshfree/Meshbased Method for the Incompressible Navier-Stokes Equations - Parts I and II: Stabilization and Coupling, *Informatikbericht-Nr.* 2005.
 - 25) Gingold, R.A., and Monaghan, J. J.: Smoothed particle hydrodynamics: theory and application to nonspherical stars, *Mon. Not. Roy. Astron. Soc.*, 181, 375–389, 1977.
 - 26) Gotoh, H., and Shao: Turbulence particle models for tracking free surfaces. *Journal of Hydraulic Research*, 43 (3): 276-289, 2005.
 - 27) Gotoh, H., Sakai, T.: Key Issues in the Particle Method for Computation of Wave Breaking, *Coastal Eng.*, 53 (2-3), 171-179, 2006.
 - 28) Gotoh, H., Okayasu, A., Watanabe Y.: Computational Wave Dynamics, *Advanced Series on Ocean Engineering*, 37, 2013.
 - 29) Gray, J. M. N. T., Wieland, M., and Hutter, K.: Gravity-driven free surface flow of cohesionless granular avalanches over complex basal topography. *Proc. R. Soc, A* 455, 1841–1874, 1999.
 - 30) Gray, J. M. N. T., Tai, Y. C., and Noelle, S.: Shock waves, dead zones and particle-free regions in rapid granular free-surface flows. *Journal of Fluid Mechanics*, 491, 161-181, 2003.
 - 31) Gray, J. M. N. T., and Cui, X.: Weak, strong and detached oblique shocks in gravity-driven granular free-surface flows. *Journal of Fluid Mechanics*, 579, 113-136, 2007.
 - 32) Grigourian, S. S., Eglit, M. E., and Iakimov, I. L.: New statement and solution of the problem of the motion of snow avalanche. *Snow, Avalanches & Glaciers. Tr. Vysokogornogo Geofizich. Inst.* 12, 104–113, 1967.
 - 33) Hakonardottir, K. M., and Hogg, A.: Oblique shocks in rapid granular flows. *J Physics of Fluids*, 17 (7), 077101, 2005.
 - 34) Hanifa, T., Agra, B., and Christian, F.: Three-Dimensional Smoothed Particle Hydrodynamics Simulation for Liquid Droplet with Surface Tension. *ISCS Selected Papers*, 2013.
 - 35) Huang Y., Dai Z., Zhang W., *Geo-disaster Modeling and Analysis: An SPH-based Approach*, Springer, 2014.
 - 36) Hans, U. Mair: Review: hydrocodes for structure response to underwater explosions, *Shock and Vibration*, 6 (2): 81-96, 1999.
 - 37) Hauksson, S., Pagliardi, M., Barbolini, M., and Jóhannesson, T.: Laboratory measurements of impact forces of supercritical granular flow against mast-like obstacles. *Cold Reg. Sci. Technol.* 49, 54–63, 2007.
 - 38) Harlow, F. H., and Welch, E.: Numerical calculation of time-dependent viscous incompressible flow of fluids with free surface, *Phys. Fluids*, 8, 2182, 1965.

- 39) Hibi, S., Yabushita, K.: A Study on Reduction of Unusual Pressure Fluctuation of MPS Method, *Journal of the Kansai Society of Naval Architects.*, Japan (241), 125-131, 03-25 (in Japanese), 2004.
- 40) Hirt, C. W., Amsden, A. A., and Cook, J. L.: An arbitrary Lagrangian-Eulerian computing method for all flow speeds, *Journal of Computational Physics*, 14:227-253, 1974.
- 41) Hirt, W., and Nichols, B. D.: Volume of fluid (VOF) method for the dynamics of free boundaries. *Journal of Computational Physics*, 39 (1): 201-225, 1981.
- 42) Hopkins, P. F.: GIZMO: A New Class of Accurate, Mesh-Free Hydrodynamic Simulation Methods. *ArXiv e-prints*, 1409.7395, 2014.
- 43) Hutter, K., Koch, T., Pluss, C., Savage S. B.: Dynamics of avalanches of granular materials from initiation to run out. Part II: Experiment. *Acta Mech*, 109, 127-165, 1995.
- 44) Ikari, H., Gotoh, H., Sakai, T., Tanioka, H.: Analysis of impact wave pressure by particle method for compressible fluid, *Annual Journal of Coastal Engineering JSCE* 52 (1), 731–735, Written in Japanese, 2005.
- 45) Iverson, R. M.: The physics of debris-flows. *Rev. Geophys*, 35, 245–296, 1997.
- 46) Janosi, I. M., Jan, D., Szabo, K. G., and Tel, T.: Turbulent drag reduction in dam-break flows, *Exp. Fluids*, 37(2), 219–229, 2004.
- 47) James, C. Lombardi, Alison Sills, Frederic A. Rasio, and Stuart L. Shapiro.: Tests of Spurious Transport in Smoothed Particle Hydrodynamics, *J. Comput. Phys.*, 152, 687–735, 1999.
- 48) Jiang, G., and Tadmor, E.: Non-oscillatory central schemes for multidimensional hyperbolic conservation laws. *SIAM J. Sci. Comput.* 19, 1892–1917, 1997.
- 49) Johnson, G. R. and Beissel, S. R.: Normalized smoothing functions for SPH impact computations. *Int. J. Numer. Methods Eng.* 39, 2725-2741, 1996.
- 50) Johnson, C. G. and Gray, J. M. N. T.: Granular jets and hydraulic jumps on an inclined plane. *Journal of Fluid Mechanics*, 675, 87-116, 2001.
- 51) Jóhannesson, T., Gauer, P., Issler, D., and Lied, K.: The design of avalanche protection dams: Recent practical and theoretical developments. *EU Report*, 2009.
- 52) Kabir, M. A., Lovell, M. R., and Higgs, III. C. F.: Utilizing the Explicit Finite Element Method for Studying Granular Flows. *Tribol Lett*, 29 (2), 85–94, 2008.
- 53) Kato, H., Otsuki, M., Saito, N., Shimizu, Y., Kimura, I.: Refinement of MPS Method for Practical Application on Large Scale Snow Avalanches. *Journal of Japan Society of Civil Engineers, Ser. B1 (Hydraulic Engineering)*, 67 (4), I_1231-I_1236, Written in Japanese, 2012.
- 54) Khayyer, A., Gotoh, H.: Modified Moving Particle Semi-implicit methods for the prediction of 2D wave impact pressure, *Coastal Eng.*, 56 (4), 419-440, 2009.
- 55) Khayyer, A., and Gotoh, H.: Enhancement of stability and accuracy of the moving particle semi-implicit method, *J. Comput. Phys.*, 230, 8, 3093-3118, 2011.
- 56) Koch, T., Greve, R., and Hutter, K.: Unconfined Flow of Granular Avalanches along a Partly Curved Surface. II. Experiments and Numerical Computations. *Proceedings: Mathematical and Physical Sciences*, 445 (1924), 415-435, 1994.
- 57) Koshizuka, S., and Oka, Y.: Moving-particle semi-implicit method for fragmentation of incompressible fluids, *Nucl. Sci. Eng.*, 123, 421–434, 1996.
- 58) Komatina, D., and Jovanovic, M.: Experimental study of steady and unsteady free surface flows with water-clay mixtures, *J. Hydraulic Research*, 35, 579-590, 1997.
- 59) Koshizuka, S., and Oka, Y.: Moving particle semi-implicit method: Fully lagrangian analysis of incompressible flows. *In European Congress on Computational Methods in Applied Sciences and Engineering. ECCOMAS*, 2000.
- 60) Koshizuka, S., Tamko, H., and Oka, Y.: A particle method for incompressible viscous flow with fluid fragmentation, *Comp. FluidDyn. J.*, 4 (1), 29–46, 1995.

- 61) Li, S., and Liu, W. K.: Meshfree and particle methods and their applications, *Applied Mechanics Review*, 55 (1): 1-34, 2002.
- 62) Libersky, L. D., and Petscheck, A. G.: Smoothed particle hydrodynamics with strength of materials, in H. Trease, J. Fritts and W. Crowley (ed.): *Proceedings of The Next Free Lagrange Conference*, Springer-Verlag, NY, 395:248-257, 1991.
- 63) Liu, G.R. and Liu, M.B.: Smoothed particle hydrodynamics: a meshfree particle method. *World Scientific*, 2003.
- 64) Liu, M.B., and Liu, G.R.: Smoothed Particle Hydrodynamics (SPH): an Overview and Recent Developments, *Arch Comput Methods Eng.*, 17, 25–76, 2010.
- 65) Lucy L.: A numerical approach to testing the fission hypothesis, *Astronomical J.*, 82, 1013–1024, 1977.
- 66) Lube, G., Huppert, H. E., Sparks, R. S. J. and Hallworth, M. A.: Axisymmetric collapses of granular columns. *J. Fluid Mech.*, 508, 175–199, 2004.
- 67) Mangeney-C, Astelnaud A., Vilotte, J. P., Bristeau, M O., Perthame, B., Bouchut, F., Simeoni, C., and Yerneni, S.: Numerical modeling of avalanches based on Saint-Venant equations using a kinetic scheme. *J. Geophys. Res.*, 108, 2527, 2003.
- 68) Matsuzawa, W., Yasuhiko, K., and Yasuhiko, I.: Study on safety factor of slope snow cover evaluation of earthquake. *Snow and Ice in Hokkaido*, 26, 96-98, Written in Japanese, 2007.
- 69) Martin, J. C., and Moyce, W. J.: An experimental study of the collapse of liquid columns on a rigid horizontal plane. *Philos. Trans. Soc. London*, A244:312–324, 1952.
- 70) McDougall, S., and Hungr, O.: A model for the analysis of rapid landslide motion across three-dimensional terrain. *Canadian Geotechnical Journal*, 41 (6), 1084-1097, 2004.
- 71) Monaghan, J. J. and Gingold, R. A.: Shock simulation by the particle method SPH, *Journal of Computational Physics*, 52:374-389, 1983.
- 72) Monaghan, J. J., Lattanzio J. C.: A refined particle method for astrophysical problems, *Astron Astrophys.*, 149:135, 1985.
- 73) Monaghan, J. J.: On the problem of penetration in particle methods, *Journal of Computational physics*, 82:1-15, 1989.
- 74) Monaghan, J. J.: Smoothed particle hydrodynamics, *Annual Review of Astronomical and Astrophysics*, 30:543-574, 1992.
- 75) Monaghan, J.J.: Simulating free surface flows with SPH, *J. Comput. Phys.*, 110, 399–406, 1994.
- 76) Monaghan, J.J., Kocharyan, A.: SPH simulation of multiphase flow, *comput. phys. commun.*, 87, 225-235, 1995.
- 77) Monaghan, J.J., Cas, R.A.F., Kos, A. and Hallworth, M.: gravity currents descending a ramp in a stratified tank. *Journal of Fluid Mechanics*, 379, 39-69, 1999.
- 78) Monaghan, J.J.: SPH compressible turbulence, *Mon.Not. Roy. Astron.Soc.*, 335 (3), 843-852, 2002.
- 79) Morris, J. P., and Monaghan, J. J.: A switch to reduce SPH viscosity, *Journal of Computational Physics*, 136:41-50, 1977.
- 80) Otsuka, T., Shimizu, Y., Kimura, I., Otsuki, M., Saito, Y.: Fundamental studies on applications of MPS method for computing snow avalanches, *International Snow Science Workshop, Davos, Proceedings*, 418-422, 2009.
- 81) Papamastasiou, T. C.: Flows of materials with yield, *J. Rheol*, Vol.31, pp. 385-404, 1986.
- 82) Premoze, S., Tasdizen, T., Bigler, j., Iefohn, A., and Whitaker, R.: Particle-based simulation of fluids. *Computer Graphics Forum* 22, 3, 401–410, 2003.
- 83) Saito, Y., Kato, Hirotaka, Otsuki, M., Kimura, I., Shimizu, Y., Isenko, E.: Refinement of MPS method for practical application to snow avalanches. *Annals of Glaciology*, 53 (61), 13-22(10), 2012.

- 84) Savage, S. B., and Hutter, K.: The motion of a finite mass of granular material down a rough incline. *J. Fluid Mech*, 199, 177–215, 1989.
- 85) Shakibaeinia, A., Jin, Y.C.: A weakly compressible MPS method for modeling of open-boundary free-surface flow, *International J. Numer. Methods Fluids.*, 63(10), 1208-1232, 2009.
- 86) Shao, and Edmond, Y.M. Lo.: Incompressible SPH method for simulating Newtonian and non-Newtonian flows with a free surface. *Advances in Water Resources*, 26 (7): 787-800, 2003.
- 87) Sigurdsson, F., Tomasson, G. G., and Sandersen, F.: Avalanche defenses for Flateyri, Iceland. From hazard evaluation to construction of defences. *Tech. Rep.* 203. Norw. Geotech. Inst., Oslo, 1998.
- 88) Silbert, L. E., Erta, S. D., Grest, G. S., Halsey, T. C., Levine, D., and Plimpton, S.: Granular Flow Down an Inclined Plane: Bagnold Scaling and Rheology. *Physical Review E* 64, 051302, 2001.
- 89) Sovilla, B., Schaer, M., Kern, M. and Bartelt, p.: Impact pressures and flow regimes in dense snow avalanches observed at the Vall' ee de la Sionne test site. *J. Geophys. Res.*, 113, F01010, 2008.
- 90) Stuart, B. Savage.: Gravity flow of cohesionless granular materials in chutes and channels. *J. Fluid Mech.* 92, 53-96, 1979.
- 91) Swegle, J.W., Hicks, D.L. and Attaway, S.W.: Smoothed particle hydrodynamics stability analysis. *Journal of Computational Physics*, 116, 123-134, 1995.
- 92) Tai, Y. C., Wang, Y. Q., Gray, J. M. N. T., and Hutter, K.: Methods of similitude in granular avalanche flows. In *Advances In Cold-Region Thermal Engineering And Sciences: Technological, Environmental and Climatological Impact, Lecture Notes in Physics*, 533, 415–428. Springer, 1999.
- 93) Tai, Y. C., Gray, J. M. N. T., Hutter, K., and Noelle, S: Flow of dense avalanches past obstructions. *Annals of Glaciology*, 32 (1), 281-284, 2001.
- 94) Vreman, A. W., Al-Tarazi, M., Kuipers, J. A. M., Van Sint Annaland, and Bokhove, O.: Supercritical shallow granular flow through a contraction: experiment, theory and simulation. *Journal of Fluid Mechanics*, 578, 233-269, 2007.
- 95) Yabe, T., Xiao, F., and Utsumi, T.: The constrained interpolation profile method for multiphase analysis. *Journal of Computational Physics*, 169 (2): 556-593, 2001.
- 96) Yaidel, R. L., Dirk, R. and Carlos, R. M.: Dynamic particle refinement in SPH: application to free surface flow and non-cohesive soil simulations. *Computational Mechanics*, 51,731–741, 2012.
- 97) Yamamoto, Y., Nunthawath, C., and Kenji, N.: Proposal of rational evaluation methods of structure damage by tsunami, *Journal of Japan Society of Civil Engineers, Ser. B2 (Coastal Engineering)*, 67(1), 72-91, 2011.
- 98) Yellin, K., Saito, Y., Kimura, I., Otsuki, M., and Shimizu Y.: Refinement of Simulation Model for Practical Design of Energy Dissipater for Snow Avalanche. *JSSI & JSSE Joint Conference on Snow and Ice Research*, 2013.
- 99) Yih-Chin, T., Wang, Y., Gray, J., and Kolumban H.: Methods of similitude in granular avalanche flows. *Advances in Cold-Region Thermal Engineering and Sciences-Lecture Notes in Physics*, 533, 415-428, 1999.
- 100) Yih-Chin, T.: Dynamics of Granular Avalanches and Their Simulations with Shock-Capturing and Front-Tracking Numerical Schemes. *PhD Dissertation, Darmstadt University of Technology, Darmstadt, Germany*, 2000.

- 101) Yoon, H.Y., Koshizuka, S., and Oka, Y.: A particle-gridless hybrid method for incompressible flows, *Int. J. Numer. Meth. Fluid*, 30, 407–424, 1999.